Molecules assembling and reacting under the constraint of weak and strong surface interactions

Inauguraldissertation

Zur

Erlangung der Würde eines Doktors der Philosophie

vorgelegt der

Philosophisch-Naturwissenschaftlichen Fakultät

der Universität Basel

von

Seyedeh Fateme Mousavi

aus dem Iran (Tehran)

Basel, 2019

Genehmigt von der Philosophisch-Naturwissenschaftlichen Fakultät auf Antrag von:

Prof. Dr. Thomas Jung
Prof. Dr. Ernst Meyer

Basel, 16.10.2018

Prof. Dr. Martin Spiess
Dekan

This thesis is dedicated to the people that I love. To the memory of my beloved mother who could not see this thesis completed, to my father, brother and sister for their ongoing love and to my beloved husband for his unlimited love and support.

Abstract

On surface chemistry and physics of nanoscale molecular self-assemblies manufactured in a "bottom-up" approach is the base on which this thesis is established. The formation of the mentioned self-assemblies is dependent on the interactions between their organic molecular building blocks and building blocks-substrate interaction. These organic molecules are synthesized for specific purposes by modifying molecular topology, structure and functional groups. The substrates employed are predominantly single crystals composed of coinage metals or single crystals with deposited adlayers. Chemical modification of these compounds via different bonding motifs (i.e. Hydrogen bonding, coordination, Van der Waals interaction, etc) in their self-assemblies is studied after their in-situ deposition using Scanning Tunneling Microscopy (STM), X-ray photoelectron spectroscopy (XPS) and Density Functional Theory (DFT).

In chapter [[1]] direct comparison between in-solution and on-surface behavior of the same compounds is presented. Synthesis and surface assembly of the higher pyrazinacenes and their oxidized analogues using PbO_2 in solution and annealing on Cu(111) substrate is studied. Upon thermal deposition of these compounds on single Cu(111) crystal, the molecules arrange in a chiral conformation. Subsequent annealing at 150 °C causes the dehydrogenation of the molecules and consequently the formation of linear arrays. Further annealing to 300 °C breaks the linear chains and the molecules appear to adopt a "double-lobe" or "two dark satellite" morphology which we attribute to further oxidation (cyclodehydrogenation).

In chapter [[2]] the unprecedented 'out-of-plane' oriented, hydrogen-bonded assemblies of a planar module, the perylene derivative DPDI on a specifically-chosen weakly interacting substrate is studied. A single atomic layer of semi-metallic Bi in p(10x10) phase is selected as the substrate as it is known to be electronically decoupled from the underlying metallic Cu(100) single crystal thus can be used to study mainly intermolecular interactions. Extended, hexagonal networks containing "windmill-shaped" nodes with unique bi-chirality features, together with a compact assembly of zigzag structures are the two spontaneously formed supramolecular structures which are of great chemical importance since direct deposition of DPDI on Cu(100) does not lead to any sort of assembly.

In chapter [[3]] the self-assembly of functionalized tetraphenylporphyrins in different architectures is presented. Trifluoromethyl and methoxy- functionalized tetraphenylporphyrins were synthesized and used to reveal polymorphism, driven by F…F interactions and C-F…H-C hydrogen bonds. The on-surface behavior of the symmetric and asymmetric functionalized

Abstract

compounds (trans and mono, respectively) is compared with tetrakis(3,4,5-trimethoxyphenyl)- and tetrakis(3,5-trifluoromethylphenyl)-porphyrins.

List of publications / manuscripts

This thesis is based on three first-author manuscripts and is provided in the 'cumulative' format. The manuscripts are listed below and are referred in the text by the double square brackets.

[[1]] - Oxidation-induced assembly and disassembly of a reduced decaazapentacene

S. Fatemeh Mousavi and David Miklík, Zuzana Hloušková, Anna Middleton, Yoshitaka Matsushita, Jan Labuta, Aisha Ahsan, Luiza Buimaga-Iarinca, Paul A. Karr, Pavel Švec, Filip Bureš, Gary J. Richards,Toshiyuki Mori, Katsuhiko Ariga, Yutaka Wakayama, Cristian Morari, Francis D'Souza, Thomas A. Jung and Jonathan P. Hill

Manuscript to be submitted.

[[2]] - Frustrated H-bonding of planar molecules on a weakly interacting semi-metallic Bi surface

S. Fatemeh Mousavi, Aisha Ahsan, Thomas Nijs, Milos Baljozovic, Aneliia Wäckerlin, Olha Popova, Sylwia Nowakowska, Christian Wäckerlin, Jonas Björk, Lutz Gade and Thomas A. Jung

Manuscript to be submitted to Chemical Communications.

[[3]] - Substitution of Mutually Interacting Substituents for Monolayer Engineering of Tetraphenylporphyrin Surface Self-assembled Structures

S. Fatemeh Mousavi, Aisha Ahsan, Luiza Buimaga-Iarinca, Cristian Morari, Mehdi Heydari, Ondrej Sedlacek, Waka Nakanishi, Yutaka Wakayama, Katsuhiko Ariga, Jonathan P. Hill and Thomas A. Jung.

Manuscript in preparation.

In addition, during my PhD studies I contributed to the following publications and manuscripts:

[1] - Phase transitions in confinements: Controlling solid to Fluid transitions of xenon atoms in an on-surface network

Aisha Ahsan, S. Fatemeh Mousavi, Thomas Nijs, Sylwia Nowakowska, Olha Popova, Aneliia Wäckerlin, Jonas Björk, Lutz H. Gade, Thomas A. Jung Small (2018)

[DOI: 10.1002/smll.201803169]

[2] - Watching nanostructure growth: kinetically controlled diffusion and condensation of Xe in a surface metal organic network

List of publications / manuscripts

Aisha Ahsan, S. Fatemeh Mousavi, Thomas Nijs, Sylwia Nowakowska, Olha Popova, Aneliia Wäckerlin, Jonas Björk, Lutz H. Gade and Thomas A. Jung
Nanoscale (2019).
[DOI: 10.1039/c8nr09163c]

[3] - The different faces of 4'-pyrimidinyl functionalized 4,2':6',4''-terpyridines: environmental effects in solution and on Au(111) and Cu(111) surface platforms

Thomas Nijs, Y. Maximilian Klein, S. Fatemeh Mousavi, Aisha Ahsan, Sylwia Nowakowska, Edwin C. Constable, Catherine E. Housecroftb and Thomas Jung.
Journal of the American Chemical Society (2018)
[DOI: 10.1021/jacs.7b12624]

[4] - Molecular chessboard assemblies sorted by site-specific interactions of out-of plane d-orbital with a semimetal template

Aneliia Wäckerlin, Shadi Fatayer, Thomas Nijs, Sylwia Nowakowska, S. Fatemeh Mousavi, Olha Popova, Aisha Ahsan, Thomas A. Jung, and ChristianWäckerlin.
Nano letters, 17, 1956-1962 (2017)
[DOI: 10.1021/acs.nanolett.6b05344]

[5] - Adsorbate-induced modification of the confining barriers in a quantum array

Sylwia Nowakowska, Federico Mazzola, Mariza N. Alberti, Fei Song, Tobias Voigt, Jan Nowakowski, Aneliia Wäckerlin, Christian Wäckerlin, Jérôme Wiss, W. Bernd Schweizer, Max Broszio, Craig Polley, Mats Leandersson, Shadi Fatayer, Toni Ivas, Milos Baljozovic, S. Fatameh Mousavi, Aisha Ahsan, Thomas Nijs, Olha Popova, Jun Zhang, Matthias Muntwiler, Carlo Thilgen, Meike Stöhr, Igor A. Pašti, Natalia V. Skorodumova, François Diederic, Justin Wells, Thomas A. Jung.
ACS Nano, 12, 768-778 (2017) [DOI: 10.1021/acsnano.7b07989]

[6] - Configuring Electronic States in an Atomically Precise Array of Quantum Boxes

Sylwia Nowakowska, Aneliia Wäckerlin, Ignacio Piquero-Zulaica, Jan Nowakowski, Shigeki Kawai, Christian Wäckerlin, Manfred Matena, Thomas Nijs, Shadi Fatayer, Olha Popova, Aisha Ahsan, S. Fatemeh Mousavi, Toni Ivas, Ernst Meyer, Meike Stöhr, J. Enrique Ortega, Jonas Björk, Lutz H. Gade, Jorge Lobo-Checa and Thomas A. Jung.
Small, 12, 3757–3763 (2016). [DOI: 10.1002/smll.201600915]

[7] - Kinetically controlled activation of diffusion pathways of Xe condensates in a surface metal organic network

Aisha Ahsan, S. Fatemeh Mousavi, Thomas Nijs, Sylwia Nowakowska, Olha Popova, Aneliia Wäckerlin, Jonas Björk, Lutz H. Gade, Thomas A. Jung

Manuscript to be submitted

[8] - Sub-PC adsorbed on Ag(111)

Luiza Buimaga-Iarinca, S. Fatemeh Mousavi, Simon Berner, Micheal de Wild, R. Bertschinger, A. Baratoff , Thomas A. Jung, and Cristian Morari

Manuscript to be submitted

Contents

List of Abbreviations

General acronyms

2D	Two Dimensional
3D	Three Dimensional
BE	Binding Energy
DOS	Density Of States
LDOS	Local Density Of States
MON	Metal Organic Network
UHV	Ultra High Vacuum
VdW	Van der Waals
HOMO	Highest Occupied Molecular Orbitals
LUMO	Lowest Unoccupied Molecular Orbitals
RT	Room Temperature
HOPG	Highly Oriented Pyrolytic Graphite
ML	Mono Layer

Methods

STM	Scanning Tunneling Microscopy
XPS	X-ray Photoelectron Spectroscopy
DFT	Density Functional Theory

Molecules / Chemical compounds

- **N8 :** 5,12-dihydro-2,3,8,9-tetraphenyl-1,4,5,6,7,10,11,12-octaazatetracene

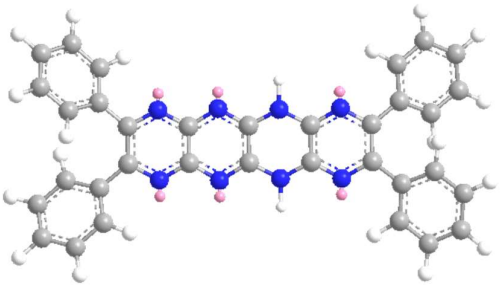

- **N10:** 6,13-dihydro-2,3,9,10-tetraphenyl-1,4,5,6,7,8,11,12, 13,14-decaazapentacene

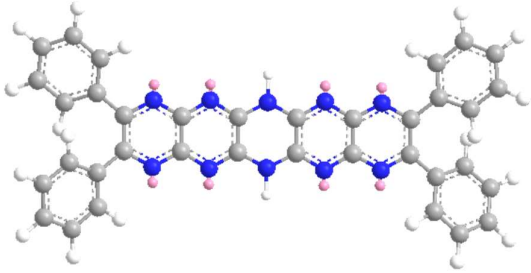

- **DPDI:** 4,9-diaminoperylene-quinone-3,10-diimine

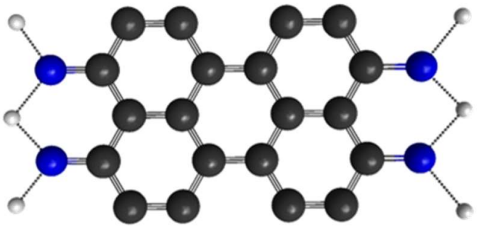

- **TRANS** 5,15-Bis(3,5-trifluoromethylphenyl)-10,20-bis(3,4,5-trimethoxyphenyl)porphyrin

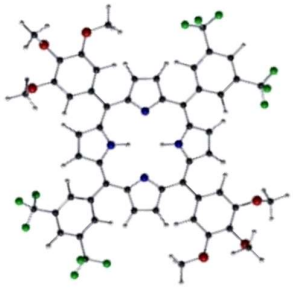

Molecules / Chemical compounds

- **MONO** 5-(3,4,5-trimethoxyphenyl)-10,15,20-tris(3,5-trifluoromethylphenyl)porphyrin

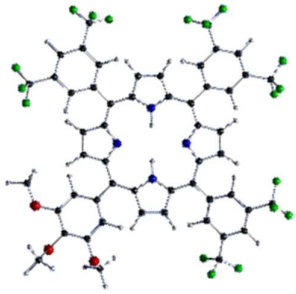

- **MeOTPP** tetrakis(3,4,5-trimethoxyphenyl)porphyrin

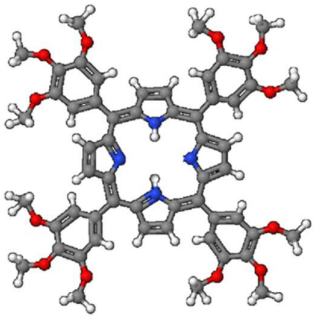

-

- **CF3TPP** tetrakis(3,5-trifluoromethylphenyl)porphyrin

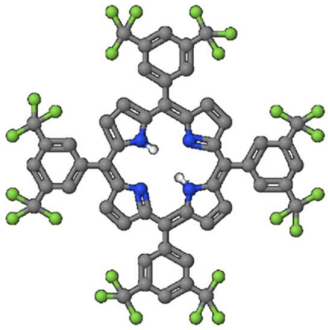

-

-

Introduction

A core topic of Nanoscience is provided by the often complex, site specific and often new behavior of molecules interacting with each other and with interfaces[1–4]. Here, the behavior of molecules is clearly different from the – physical – adsorption process and also from the – chemical – reaction within a fluid matrix. Even in molecular life science, a long established field, we become increasingly aware that the function of a biomolecular machine is site specific and depends the specific molecular architecture, not only on the presence of one or the other molecule in a fluid to be functional[5]. So it is not only the structure, but also the structure of the environment that determines the function of a biomolecule[6].

Far beyond the analysis of functional bio molecular entities scientists desire to design and create new functional molecular structures which is the topic of self-assembly and supramolecular chemistry[7–10]. Also here the first in-fluid achievements lead to more recent implementations of site specific architectures i.e. molecular motors and ultimately to a 2nd Nobel price.

The focus of this thesis is provided by on-surface supramolecular chemistry. I have studied the supramolecular chemistry and the function (here reactivity) of molecules which are bound to the surfaces (i.e. in 'flatland') in vacuum and in absence of solution.

Biomolecular structure, e.g. protein folding is determined by conformational adaptation and a balance of weak and strong interactions[11,12]. Mostly non-covalent i.e. physical (VdW, H-bond and polar) forces are involved in biomolecular folding while also covalent bonds are formed at decisive locations to secure the shape of life's molecular architectures[13,14].

At solid surfaces molecules experience already very strong forces by the surface potential and the chemical and physical interaction with the surface atoms. This implies that any shape directing interaction has to be of at least comparable strength. Also the thermal stability of bio-molecules is generally too low for any practical chemical or physical application.

This leaves us – who are working with on-surface supramolecular chemistry – with the challenges (1) to predictably create strongly bound functional structures while still using stronger bonds from the same set of interaction forces; and (2) to investigate their physical properties and chemical function or reactivity as it often derives from the same molecule in fluid.

The big advantage of this approach is that 'molecular self-assembly' allows for the spontaneous, creation of identical nanostructures if the proper molecular building blocks and the right process conditions are used. At the down-side it has to be mentioned that it is an enormously difficult task to understand self-assembly at the limit of even small molecules with 100 some atoms – way smaller than biomolecules – and create functional entities. Nature in the action of biochemical

evolution has been able to sample a parameter space which is not going to be covered by a few scientists in a few years of their action who are operating with different target properties and aiming at different i.e. non-biological functions.

In my work I have investigated the already very complex behavior of small molecules in different surface environments. Interestingly, their reactivity is sometimes comparable to what is known from the bulk and sometimes not; their assembly in supramolecular architectures on substrate surfaces is controlled by the complex interplay of interactions at the solvent free molecule/surface interface and between ad-molecules. The formation of on-surface supramolecular structures and their modification with progressing reactions has been investigated by Low Temperature Scanning Tunneling Microscopy (LT-STM), X-ray photoelectron spectroscopy (XPS) and Density Functional Theory (DFT).

In chapter [[1]] of this thesis I present the direct comparison of two molecules from the same family of compounds at the solid-vacuum interface and in-solution. Specifically I have worked with N8 and N10 from the pyrazinaacenes, a N bearing modification of the important organic semiconductor pentacene[15,16] .In close collaboration with the synthetic chemistry group we have investigated the step by step oxidation of the compounds on surfaces and the consecutive modification of the self-assembly. Our exhaustive experimental results provide evidence for a novel photo-redox activity of this organic semiconductor. [17] Since STM gives us a direct real-space access to the resulted 2D self-assemblies[18], it simplifies understanding the chemical and physical phenomena upon formation of the nano-structures and helps us to learn much more about the compounds, also in comparison to solution studies.

The interaction of the organic molecules with the underlying substrates plays a crucial role in molecular self-assembly as well as for the chemical and electronic properties of the resulting interfaces[19]. Studies in on-surface chemistry and supramolecular chemistry have been mostly performed on coinage metal substrates. More recently alternative substrates like graphene[20,21], boron-nitride layers[22,23], alkali-halide layers[24] and Sn Alloys[25] have been chosen. In chapter [[2]] of this thesis a novel substrate (Bi/Cu(100))[26] has been used to study the formation of interesting non-planar H-bonded assemblies of DPDI, an amino-functionalized perylene derivative. This particular molecule has been intensively investigated by earlier members of my hosting group[19,27] and has not been observed to form supramolecular assembled structures in its native, non-dehydrogenated form. In my work on the Bi/Cu(100) substrate I have observed H-bonding which is only enabled by re-orientation (tilting) of the planar adsorbate molecules

Chemical functionalization, e.g. with directional or non-directional bonding groups, is another method which is widely used to control the arrangement of molecules in self-assembled structures.

Chemical functionalization is of crucial importance in nanoscience and technology because it enables scientists to control the self-assembly processes and to manufacture molecular arrays with well defined, in some cases pre-defined nanostructures[28–30]. In addition, the clever choice of the functionalization by chemists helps to achieve highly ordered supramolecular structures with considerable control level[31]. Chapter [[3]] of this thesis is dedicated to self-assemblies of newly synthesized porphyrins functionalized with methoxy and trifluoromethyl groups. In my studies on different substrates I found a complex polymorphism driven Fluorine H-bonding. The choice of the Porphyrin building block has been motivated by the large body of knowledge about their functionalization and synthesis and also for the importance of these compounds for application like photodynamic therapy[32], toxicology[33], molecular electronics, semiconductor/sensor technology[34] and finally supramolecular chemistry[35–38].

Methods

This section gives a short description of the main methods used to study on surface self-assemblies and nanostructures in this thesis. To characterize the resulted nanoscale structures a combination of different methods were used. Scanning tunneling microscopy was used to perform real-space structural characterization and X-ray photoelectron spectroscopy (XPS) was used for quantitative and qualitative element specific analysis.

Scanning tunneling microscopy (STM)

STM is an electron microscope with atomic level resolution. It is based on a quantum mechanical effect called 'tunneling' which occurs once a bias voltage is applied between the tip and the sample and the distance between the tip and sample is only few angstroms. Upon tunneling, the electrons have a non-zero probability to pass through the tiny vacuum gap between tip and sample. The resulted current depends on the distance between tip and sample and the local density of states (LDOS). The tip is attached to a piezoelectric scanner whose in-plane movements helps imaging the sample with sub-angstrom precision. Scanning can be performed in two modes: the constant current or the constant height mode. In the constant current mode, a feedback loop is used to adjust the tip vertically in such a way that the current stays constant and the height is recorded. In constant height mode, the vertical position of the tip is not changed, using a slow or disabled feedback. The current as a function of lateral position represents the surface image. Occupied and unoccupied states of the sample can be measured by applying negative and positive sample voltages respectively.

X-Ray Photoelectron Spectroscopy (XPS)

X-ray Photoelectron Spectroscopy (XPS), also known as Electron Spectroscopy for Chemical Analysis (ESCA) is a widely used technique to investigate the chemical composition of surfaces. It is based on the photoelectric effect for the discovery of which Einstein won the Noble prize in 1921 and was developed in the mid-1960 by Kai Siegbahn and his research group at the University of Uppsala and ended to their Nobel prize in 1981. It is an element-specific and surface sensitive technique. Using XPS, the binding energies (BE) of the electronic core-levels of the atoms are probed by analyzing their kinetic energy after excitation with monochromatic X-ray light. The following equation is used to measure the electron binding energy of each of the emitted electrons:

$$E_{binding}=E_{photon}-(E_{kinetic}+\phi)$$

In the above equation, the energy of the X-ray with particular wavelength is known (MgKα photon with an energy of 1253.6 eV or AlKα photon with an energy of 1486.6eV), the kinetic

energies of the emitted electrons are measured and ϕ is the work function which depends on the spectrometer and the material. Changes in the local environment of the electrons causes small changes in the obtained binding energy, called chemical shift considering which both elements and states identification is possible. Stoichiometry analysis is also possible considering the number of the events of specific energy recorded by the XPS detector.

Chapter [[1]] and Supplementary Information

[[1]] - Oxidation-induced assembly and disassembly of a reduced decaazapentacene

S. Fatemeh Mousavi and David Miklík, Zuzana Hloušková, Anna Middleton, Yoshitaka Matsushita, Jan Labuta, Aisha Ahsan, Luiza Buimaga-Iarinca, Paul A. Karr, Pavel Švec, Filip Bureš, Gary J. Richards,Toshiyuki Mori, Katsuhiko Ariga, Yutaka Wakayama, Cristian Morari, Francis D'Souza, Thomas A. Jung and Jonathan P. Hill

Contribution of S. F. Mousavi: carried out experimental investigations (STM & XPS), analyzed and interpreted the data, wrote the manuscript together with chemistry collaborators. Shared first authorship with the synthesis chemist.

Oxidation-induced assembly and disassembly of a reduced decaazapentacene

David Miklík[†],[a],[b] S. Fatemeh Mousavi[†],[c] Zuzana Hloušková,[b] Anna Middleton,[d] Yoshitaka Matsushita,[e] Jan Labuta,[a] Aisha Ahsan,[c] Luiza Buimaga-Iarinca,[f] Paul A. Karr,[g] Pavel Švec,[a] Filip Bureš,[b] Gary J. Richards,[a],[h] Toshiyuki Mori,[i] Katsuhiko Ariga,[a],[j] Yutaka Wakayama,[a] Cristian Morari,[f] Francis D'Souza,*,[d] Thomas A. Jung*,[k] and Jonathan P. Hill*,[a]

Abstract: We report the synthesis and surface assembly of higher pyrazinacenes which are structurally related to the key organic semiconductor compound pentacene, *i.e.* 6,13-dihydro-2,3,9,10-tetraphenyl-1,4,5,6,7,8,11,12,13,14-decaazapentacene (**1**) and 5,12-dihydro-2,3,8,9-tetraphenyl-1,4,5,6,7,10,11,12-octaazatetracene (**2**) and their oxidations to the corresponding decaazapentacene (**1**-ox) and octaazatetracene (**2**-ox) chromophores. Our physico-chemical investigation, in particular of the behaviour in solution and at interfaces revealed different oxidation states of the compounds available in those media and lead to the finding that **1** and **2** are also efficient photoredox catalysts for C-C bond forming reactions. **1** and **2** form well-defined structures on a solid Cu(111) substrate: they adopt chiral conformations in their native state and form self-assembled linear arrays of molecules at ambient temperature or by annealing at 150 °C due to dehydrogenation of the dihydroacene cores to the corresponding decaazapentacene (**1**-ox) and octaazatetracene (**2**-ox). Further annealing of the ad-surface structures at high temperature (300 °C) leads to cyclo-dehydrogenation of the reduced oligoazaacene cores as confirmed by scanning tunneling microscopy data, density functional theory modelling and X-ray photoelectron spectroscopy.

[a] Dr. D. Miklík, Dr. J. Labuta, Dr. P. Švec, Dr. G. J. Richards, Prof. Dr. K. Ariga, Dr. Y. Wakayama, Dr. J. P. Hill
International Center for Materials Nanoarchitectonics
National Institute for Materials Science
Namiki 1-1, Tsukuba, Ibaraki 305-0044, Japan
E-mail: Jonathan.Hill@nims.go.jp
[b] Dr. D. Miklík, Dr. Zuzana Hloušková, Prof. Dr. F. Bureš
Institute of Organic Chemistry and Technology
Faculty of Chemical Technology
University of Pardubice
Studentská 573, Pardubice 53210, Czech Republic
[c] S. F. Mousavi, Dr. A. Ahsan,
Department of Physics
University of Basel
Klingelbergstrasse 82, 4056 Basel, Switzerland
[d] A. Middleton, Prof. Dr. F. D'Souza
Department of Chemistry
University of North Texas
1155 Union Circle, 305070 Denton, Texas 76203, USA
E-mail: francis.dsouza@unt.edu
[e] Dr. Y. Matsushita
Research Network and Facility Services Division
National Institute for Materials Science
1-2-1 Sengen, Tsukuba, Ibaraki 305-0047, Japan
[f] Dr. L. Buimaga-Iarinca, Dr. Cristian Morari
National Institute for Research and Development of Isotopic and Molecular Technologies (NIRDIMT)
65-103 Donath, Ro-400293, Cluj-Napoca, Romania
[g] Prof. Dr. P. A. Karr,
Department of Physical Sciences and Mathematics
Wayne State College
111 Main Street, Wayne, Nebraska, 68787, USA
[h] Dr. G. J. Richards
Department of Chemistry
Ochanomizu University
Otsuka 2-1-1, Bunkyo-ku, Tokyo 112-8610, Japan
[i] Dr. T. Mori
Center for Green Research on Energy and Environmental Materials
National Institute for Materials Science
Namiki 1-1, Tsukuba, Ibaraki 305-0044, Japan
[j] Prof. Dr. K. Ariga
Graduate School of Frontier Sciences
The University of Tokyo
Kashiwa 277-0827, Japan
[k] Prof. Dr. T. A. Jung
Laboratory for Micro- and Nanotechnology
Paul Scherrer Institute
5232 Villigen PSI, Switzerland
E-mail: thomas.jung@psi.ch
†**These authors contributed equally to this work.**
Supporting information for this article is given via a link at the end of the document.

Acenes,[1–4] in particular pentacene,[5,6] are a class of compounds that have become increasingly important for a variety of applications as synthetic methods for their preparation have advanced.[7,8] Pentacene (Scheme 1) itself is the archetypal p-type organic semiconductor[9] and it has been extensively studied from this viewpoint despite an inconvenient susceptibility to be oxidized to its pentacene-6,13-quinone form,[10,11] an unfortunate consequence of its electron richness.

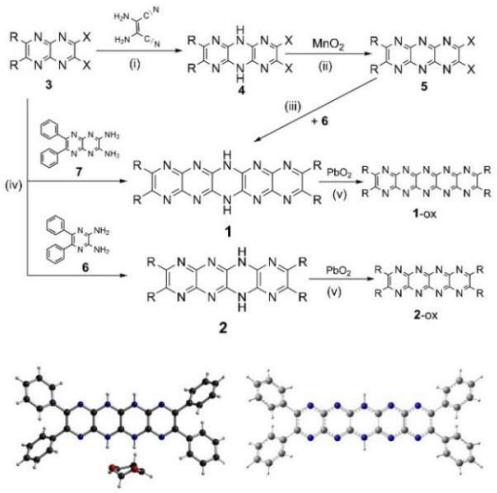

Scheme 1. Top: synthesis of target compounds **1** and **2** and their oxidized derivatives. R = C_6H_5 (**1**, **2**), $tBuC_6H_4$ (**1**-tBu); X = nitrile or chloride. Reaction conditions: (i) DMSO, Na_2CO_3, 90 °C, 4 h, 47% (ii) CCl_4:MeCN:H_2O (2:2:1), RuO_2, $NaIO_4$, r.t., 1 h, 50-60%. (iii) DMSO, Na_2CO_3, 120 °C, 4 h, 10 %. (iv) DMSO, K_2CO_3, 120 °C, 4 h, 35 %. (v) PbO_2, CH_2Cl_2, >95 %. Bottom left: X-ray crystal structure of **2**. Bottom right: DFT calculated structure of **1**.

This disadvantage can be ameliorated for by several means: introduction of pentacene 6,13-substituents is one method used to preclude oxidation.[12] Alternatively, heteroatoms may be

introduced so that the acene is either stabilized electronically or oxidation is blocked by the presence of heteroatoms at affected sites.[13] Both these methods can have other beneficial effects such as increased solubility of the compounds or promotion of other properties such as sensing behaviour[14] and tautomerism.[15] Addition of heteroatoms to the acene core can also be used to facilitate the synthesis of higher acenes[16–18] (e.g. nonacene[19]) as can the appending of multiple substituents where stability is conferred by steric rather than electronic factors.[20] Higher acenes are important because of the possible existence of 'exotic' electronic states such as stable open shell biradicals[21] and other radicaloids.[22,23]

In this work we prepare acenes composed exclusively of fused 1,4-pyrazine units leading to compounds we term 'pyrazinacenes' (Scheme 1). A significant aim of this work has been to obtain unknown analogues of acenes with N atoms replacing bridgehead-CH groups. We[24] and others[25–33] have had some success preparing these materials (including those with non-identical heteroatoms[34,35]). We have now synthesized the octaazatetracene and decaazapentacene cores (see Section 2.0, Supporting Information). The crystal structure of **2** is shown in Scheme 1 (bottom left). The molecular form of **2** in the crystal is remarkably similar to its structure obtained by DFT calculation including the conformation of the phenyl substituents. Crystals of **1** were not suitable for single crystal X-ray analysis. However, given the good agreement between crystal and DFT structures for **2**, we suggest that the calculated structure (Scheme 1, bottom right) should be closely similar to the actual structure including the form of the phenyl groups.

1 and **2** are susceptible to oxidation to the nitrogenous analogues **1**-ox and **2**-ox of pentacene and tetracene (i.e. decaazapentacene and octaazatetracene), respectively, where all the apical CH groups are replaced by pyridine-type N atoms. Electronic absorption and fluorescence spectra of **1**, **2** are shown in Figure 1a,b spectrum except that the band at 450 nm (the 2nd acene band) is the absorption maximum; a feature we attribute to tautomerization in this molecule and which has been observed for fluoflavine (dihydro-2,3,8,9-tetraazatetracene).[36] **1**-ox and **2**-ox were obtained by treating solutions of **1** or **2** with PbO_2[37,38] both undergoing a shift in absorption maximum to longer wavelength (590 nm for **1**-ox and 540 nm for **2**-ox; see Figure S3). Oxidation can also be achieved electrochemically (see Figure 1b(i,ii)) with **2** being more easy to oxidize than **1** by around 300 mV. This can be attributed to the greater electron deficiency of **1** over **2**. **2**-ox was found to have a low reduction potential of -0.293 mV (see Figure S4) DFT was used to calculate structures of the highest occupied molecular orbitals (HOMO) and lowest unoccupied molecular orbitals (LUMO) of the compounds (Figures S5-S8). HOMO and LUMO structures of **1** and **2** are shown in Figure 1c. The HOMO structures of **1** and **2** are similar to those found for other pyrazinacenes[24,39] and to reduced N-heteroacenes such as fluorubine[40] and dihydrodiazapentacene.[41] Oxidation differentiates the compounds: while **2**-ox attains an acene-like form for its molecular orbitals, **1**-ox gains a delocalized state due to the presence of nitrogen lone pairs on adjacent pyrazine units (see Figure S8). Based on this and previous work (also based on DFT calculations), structures containing five fused pyrazine rings and above appear to prefer delocalization of the pyrazine nitrogen atom lone pairs. This was first observed by Winkler and Houk[42] in their calculations of the electronic structure of decaazapentacene. In the case of **1**-ox, this feature seems to reduce the amount of electron density found on the phenyl substituents. Having established that **1** and **2** can exist in different states of oxidation in solution, we were stimulated to observe how this property might affect their assembly and reactivity in contact with metal surfaces.

1 and **2**, due to their very similar structures, appear also similar when studied by scanning tunneling microscopy on a Cu(111) surface, which we have used as a model substrate to investigate the supramolecular self-assembly and reactivity at the interface. Details

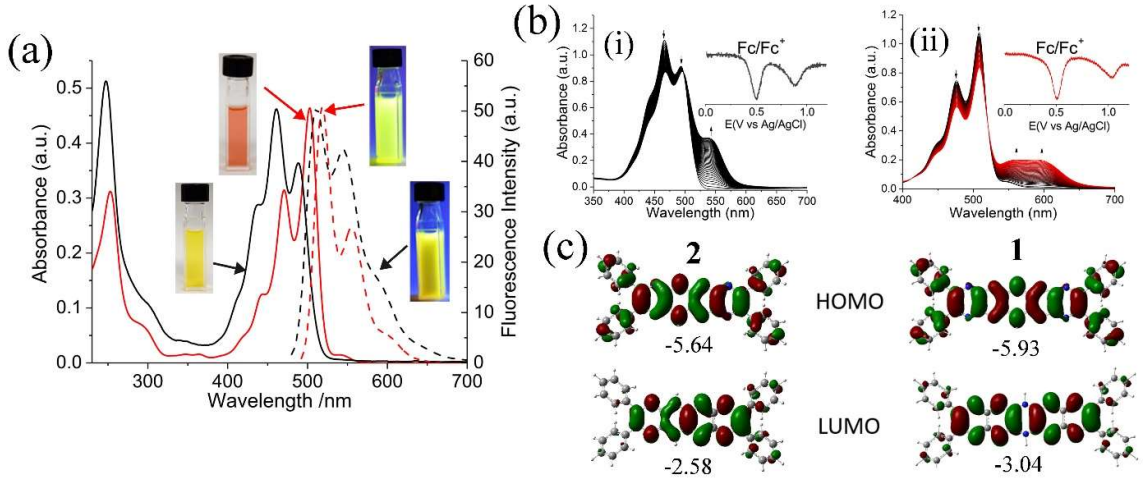

Figure 1. (a) Electronic absorption (UV/Vis) and fluorescence spectra of **1** (red) and **2** (black) in dry CH_2Cl_2. Insets show the appearance of solutions under room light or 365 nm ultraviolet light. For more information see Supporting Information. (b) Spectroelectrochemistry during oxidation of (i) **2** and (ii) **1** both in benzonitrile. Insets show the differential pulsed voltammograms for these processes. (c) Structures of HOMOs and LUMOs of (from left) **2**, and **1**. Energies are in eV.

together with images of their solutions in dichloromethane (see also Figure S1,S2). **1** shows an acene-type 4-banded spectrum with an absorption maximum at 500 nm and shorter wavelength peaks gradually diminishing in intensity. **2** has a similar several banded

of **2** are shown (see Figure S11 for details of **1**). For compound **2** (Figure 2), molecules exhibit a double-lobed morphology (Figure 2a,d). The almost exclusive presence of individual adsorbates indicates repulsive electrostatic interactions occurring after

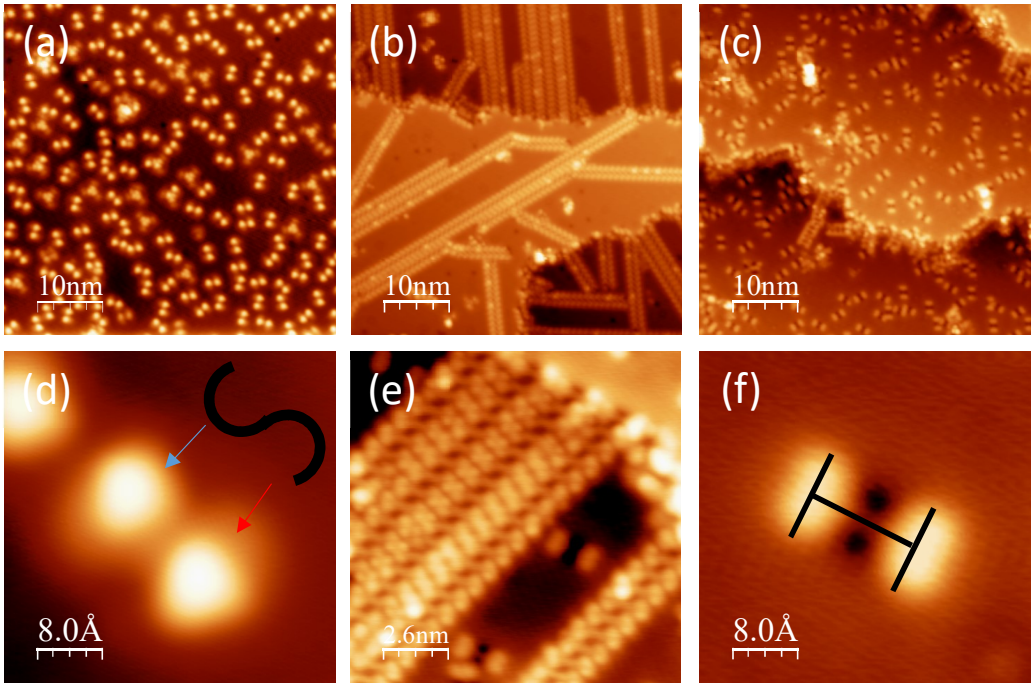

Figure 2. Scanning tunneling micrographs of **2** on Cu(111) substrate. (a) Double-lobed shaped individual adsorbates of **2** distributed randomly after deposition onto substrate maintained at room temperature. (b) Linear arrays form slowly under ambient temperature (more rapidly at 150°C) on Cu(111). (c) Individual adsorbates formed upon annealing at temperatures up to 300°C. The dark zone at the position of the molecular backbone and the reduced apparent height of the molecules (See Figures S17, S18) indicate their strengthened interaction with the substrate after annealing. (d-f) Magnified images of species contained in (a-c), respectively. (d) Double-lobe shaped monomers are chiral. Note the asymmetry of each lobe forming the double-lobed structure, marked by red and blue arrows, which appears in 'S' and mirror 'S' shape for the two chiral conformers. (e) Line structures showing packing structures of the lines (spots are phenyl rings, lines are the acene backbone). (f) Profile modification of individual molecules upon annealing at higher temperature is consistent with dehydrogenation/cyclodehydrogenation (see main text). STM data information: (a) 50nm x 50nm, 10pA, 1V. (b) 50nm x 50nm, 30pA, 500mV. (c) 50nm x 50nm, 10pA, 1V. (d) 4nm x 4nm, 50pA, 1V. (e) 13nm x 13nm, 30pA, 500mV. (f) 4nm x 4nm, 30pA, 500mV.

polarization/charge transfer between the adsorbate and the substrate. The molecules are adsorbed in registry with the substrate with 6 different orientations (see Figure S12(a)), which makes sense for a chiral conformer (× 2) on a threefold (× 3) symmetric substrate surface. Note that the chiral conformers occur from the relative twisting of phenyl groups of the molecule with each denoted as 'S' and its reflection in Figure S12(b). Surprisingly, **1** or **2** gradually assemble on the substrate (under ambient temperature, see Figure S13, or at 150 °C) into linear arrays (Figure 2b,e), which are formed by molecules arranged with their long axes aligned parallel with an offset. These linear arrays are stabilized by C-H…N hydrogen bonds involving phenyl rings and terminal pyrazine rings as depicted in Figure S14 (such interactions are known from crystal structures of similar molecules[24] – see also Figure S15). Molecular long axes are canted at an angle of 75° to the long axis of the line structures. XPS data (Figure S16) reveal that a single type of pyridine-type N atom (N1s 398.3 eV[43]) is present in molecules contained in the line structure indicating that dehydrogenation of the pyrazinacene core of **2** has occurred yielding **2**-ox, which is also available by chemical oxidation. Annealing at 150°C appears to increase somewhat the rate of line formation but also leads to the appearance of unusual double-lobed structure different from the starting morphology. To investigate this we annealed at higher temperature (300 °C, see Figure 2c), which lead to the disappearance of the line structures and molecules appeared to have exclusively the new double-lobed profile. We assign the double-lobe/two dark satellites transition to molecules that have been further oxidized (cyclodehydrogenated) with concurrent release of hydrogen into the vacuum. Cu(111) is known to be capable of acting as an oxidizing agent and **2** can be easily oxidized to **2**-ox even by mild oxidizing agents (*vide infra*). Cu(111) is also known to act as a cyclodehydrogenating agent at elevated temperatures.[44] The considerably flattened STM profiles of **1** and **2** (Figures S17,S18) obtained after annealing at higher temperatures contrasts strongly with that of the as-deposited molecules. During this annealing-induced conformational transition, the phenyl substituents take a symmetric, planar position and, correspondingly, the conformational enantiomers are no longer visible (Figures S17,S18). Therefore, cyclodehydrogenation of the peripheral 1,2-diphenylbenzene units of **2** must have occurred on the Cu(111) surface at 300 °C yielding the tetrabenzo[*a,c,n,p*]-5,7,9,11,18,20,22,24-octaazahexacene derivative whose dimensions and profile fit well with those observed. Molecules of **2**, therefore, undergo two oxidative transformations on Cu(111) first leading to **2**-ox (whose non-coplanar phenyl substituents remain visible), which assembles to the line structure, followed by cyclodehydrogenation to highly planar heteroacene species, which do not assemble, resulting in disassembly of the **2**-ox line structure.

1 (see Figure S11) behaves similarly to **2,** in that linear arrays are formed either by annealing under ambient conditions or at slightly elevated temperatures. Differences in STM contrast between **1** and **2** line structures can be attributed to their different backbone length and to the different conformers each of them can form. The conformers i) differ within the same chain and also ii) contribute to the different alignment of the molecules within the chains of **1** and **2**. Details are shown in Figure 3 and Figure S19). This confirms that phenyl rings can rotate in the molecules in response to the line structure. The STM images (for **2**) were simulated using DFT methods (see Figures S20-S25) revealing excellent agreement

between the calculated structures and those observed experimentally. In particular, we found no evidence (from STM or DFT simulated structures) for the presence of Cu adatoms being coordinated within the line structures with the most important intermolecular interactions apparently being C-H…N hydrogen bonds. The calculated structures also indicate that there exist some interaction between pyrazinacene N-atoms and the copper surface atoms in the oxidized forms of **1** and **2** which form the line structures (see Figures S20(b) and S21).

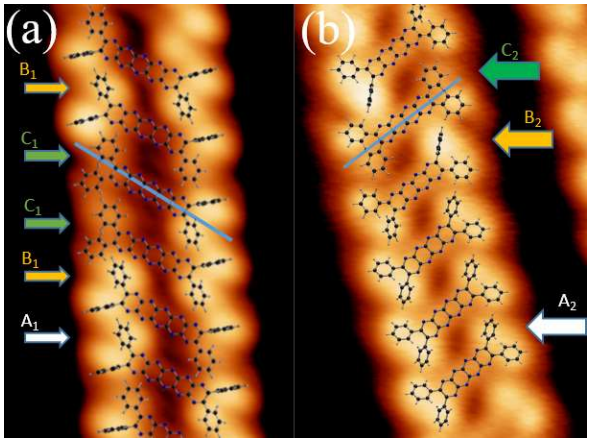

Figure 3. Line structures obtained after on-surface oxidation of (a) **1** and (b) **2** formed by the linear packing of specific conformers. A_1, B_1 and C_1 denote three different conformations of **1** arranged within a linear array. **2** similarly shows 3 conformations A_2, B_2 and C_2 with the corresponding height profile analysis shown in Supporting Information (Figure S9). The respective packing models for **1** and **2** have been overlaid onto the micrographs. Notably the different lengths of the molecular axis of **1** and **2** cause different conformers and different angles of the molecular axis (blue lines) with the axis of the chain. STM data information: a) 300mV, 50pA, 4nm x 6nm. b) 500mV, 40pA, 4nm x 6nm.

Both the on-surface reactivity observed in our STM study and the reactivity in solution (i.e. via the step-wise dehydrogenation of the pyrazinacene core on the surface and electrochemically) for **1** and **2** suggest a complex redox activity pattern, while their optical and redox properties in solution also resemble those recently reported for a push-pull dicyanopyrazine.[45-50] For these reasons, we have made a preliminary examination of their photoredox catalytic activities in the benchmark cross-dehydrogenative coupling (CDC) reaction[49] between *N*-phenyltetrahydroisoquinoline (THIQ) and nitromethane as shown in Scheme S1. The reactions were run for 24 hours with 1 mol% of the catalyst by irradiating the reaction mixture with Royal Blue LED under air at 25 °C. Both pyrazinacenes were capable of causing C-C bond formation between THIQ and nitromethane. However, the catalytic performances of **1** and **2** differ slightly (see Table S1). According to the observed conversions and isolated yields, decaazapentacene **1** proved to be a less efficient catalyst than octaazatetracene **2**. This is likely due to the greater compatibility of the absorption maximum of **2** (~ 450 nm) with the high energy emission band of the Royal Blue LED (~ 450 nm) (**1** possesses the absorption maxima red-shifted by about 50 nm). Hence, **2** afforded better conversion (72 %) and isolated yield (70 %) of the CDC product than **1** (67 and 63 %).

We have reported the first synthesis of the pyrazinacenes, dihydrooctaazatetracene (**2**) and dihydrodecaazapentacene (**1**) core chromophore structures lacking N-substituents. These compounds may be oxidized respectively to octaazatetracene (**2**-ox) and decaazapentacene (**1**-ox) most notably observed *in situ* in a scanning tunneling microscope where the oxidation states of the molecules affect their surface behaviours. **1**-ox and **2**-ox can then be further oxidized by cyclodehydrogenation of their phenyl substituents to their planar analogues, tetrabenzo- octaazahexacene and tetrabenzodecaazaheptacene, respectively. The solution state electrochemical properties, comprise relatively low first oxidation potentials and a low reduction potential (as observed for **2**). For the also easy dehydrogenation of **1** and **2** respectively to **1**-ox and **2**-ox at interfaces, we considered that the compounds could be useful as electron/proton transfer conduits for catalysis. These chromophore properties of **1** and **2** can be photochemically exploited in the form of photo-stimulated redox activities catalytically forming C-C bonds. Although the detailed mechanism of this photocatalysis is under investigation, it is notable that **1** and **2** are both sufficiently stable to be used under (irradiative) reaction conditions where similar acene compounds would not. Tetracene or pentacene may be considered most important for their semiconductor behaviour or use *e.g.* in organic light-emitting diodes. Decaazapentacene in its various states of oxidation and/or protonation, on the other hand, appears to be interesting because of its photochemical behaviour as a proton-coupled chromophore that can be oxidized, deprotonated and protonated as reported here. This is in addition to the possibility of it having complementary semiconductor properties to pentacene. These and other aspects make the pyrazinacenes a significant member of the acene family of materials.

Experimental Section

For synthesis and other experimental details see Supporting Information.

Acknowledgements

Prof. Masakazu Aono, MANA directorate, and MANA visiting scientists program are acknowledged for their decisive role in triggering this collaboration. R. Schelldorfer and M. Martina are acknowledged for their technical support; T. Nijs for helpful discussions. This study was supported by JSPS KAKENHI Grant Numbers JP15K13684 (Linear acene proton conductors for molecular electronics), JP16H06518 (Coordination asymmetry), and CREST, Japan (Grant # JPMJCR1665). The authors are also grateful to the Paul Scherrer Institute, the Physics Department of the University of Basel and the Swiss Nanoscience Institute, the Swiss National Science Foundation (Grant # 200020_162512, 206021_144991, 206021_121461), the Swiss Commission for Technology and Innovation (CTI, 16465.1 PFNM-NM) and the Swiss Government Excellence Scholarship Program for Foreign Scholars. XPS measurements were performed at the Laboratory for Micro- and Nanotechnology at the Paul Scherrer Institute (PSI). STM data were processed using the WSXM software.[51] L. B.-I. and C. M. acknowledge financial support from MCI Romania, CORE program, project PN 18 03 02 01.

Keywords: acene • N-heteroacene • pyrazinacene • scanning tunnelling microscopy • photocatalysis

[1] J. E. Anthony, *Chem. Rev.* **2006**, *106*, 5028 – 5048.
[2] Q. Ye, C. Chi, *Chem. Mater.* **2014**, *26*, 4046 – 4056.
[3] M. Bendikov, F. Wudl, D. F. Perepichka, *Chem. Rev.* **2004**, *104*, 4891 – 4945.

[4] Z. Sun, J.-S. Wu, *Aust. J. Chem.* **2011**, *64*, 519 – 528.
[5] E. Clar, Fr. John, *Ber. Dtsch. Chem. Ges. B* **1930**, *63B*, 2967 – 2977.
[6] C. F. H. Allen, J. W. Gates, *J. Am. Chem. Soc.* **1943**, *65*, 1502 – 1503.
[7] H. Qu, C. Chi, *Curr. Org. Chem.* **2010**, *14*, 2070 – 2108.
[8] M. Watanabe, K.-Y. Chen, Y. J. Chang, T. J. Chow, *Acc. Chem. Res.* **2013**, *46*, 1606 – 1615.
[9] T. Yasuda, T. Goto, K. Fujita, T. Tsutsui, *Appl. Phys. Lett.* **2004**, *85*, 2098 – 2100.
[10] A. Etienne, C. Beauvois, *Compt. Rend.* **1954**, *239*, 64 – 66.
[11] I. Kaur, W. Jia, R. P. Kopreski, S. Selvarash, M. R. Dokmeci, C. Pramanik, N. E. McGruer, G. P. Miller, *J. Am. Chem. Soc.* **2008**, *130*, 16274 – 16286.
[12] J. E. Anthony, J. S. Brooks, D. L. Eaton, S. R. Parkin, *J. Am. Chem. Soc.* **2001**, *123*, 9482 – 9483.
[13] For example: G. Li, K. Zheng, C. Wang, K. S. Leck, F. Hu, X. W. Sun, Q. Zhang, ACS *Appl. Mater. Interfaces* **2013**, *5*, 6458 – 6462.
[14] P.-Y.Gu, Z. Wang, Q. Zhang, *J. Mater. Chem. B* **2016**, *4*, 7060 – 7074.
[15] R. Scipioni, J. P.Hill, G. J. Richards, M. Boero, T. Mori, K. Ariga, T. Ohno, *Phys. Chem. Chem. Phys.* **2011**, *13*, 2145 – 2150.
[16] J. E. Anthony, *Angew. Chem. Int. Ed.* **2008**, *47*, 452 – 483.
[17] H. F. Bettinger, C. Toenschoff, *Chem. Rec.* **2015**, *15*, 364 – 369.
[18] R. Dorel, A. M. Echavarren, *Eur. J. Org. Chem.* **2017**, *2017*, 14 – 24.
[19] I. Kaur, M. Jazdzyk, N. N. Stein, P. Prusevich, G. P. Miller, *J. Am. Chem. Soc.* **2010**, *132*, 1261 – 1263.
[20] J. Xiao, H. M. Duong, Y. Liu, W. Shi, L. Ji, G. Li, S. Li, X.-W. Liu, J. Ma, F. Wudl, Q.Zhang, *Angew. Chem., Int. Ed.* **2012**, *51*, 6094 – 6098.
[21] M. Bendikov, K. N. Houk, H. M. Duong, K. Starkey, E. A. Carter, F. Wudl, *J. Am. Chem. Soc.* **2004**, *126*, 7416 – 7417.
[22] S. Dong, T. S. Herng, T. Y. Gopalakrishna, H. Phan, Z. L. Lim, P. Hu, R. D. Webster, J. Ding, C. Chi, *Angew. Chem. Int. Ed.* **2016**, *55*, 9316 – 9320.
[23] Z. Sun, Z. Zeng, J. Wu, *Acc. Chem. Res.* **2014**, *47*, 2582 – 2591.
[24] G. J. Richards, J. P. Hill, N. K. Subbaiyan, F. D'Souza, M. R. J. Elsegood, S. J. Teat, T. Mori, K. Ariga, *J. Org. Chem.*, **2009**, *74*, 8914 – 8923.
[25] U. H. F. Bunz, *Acc. Chem. Res*. **2015**, *48*, 1676 – 1686.
[26] U. H. F. Bunz, J. U. Engelhart, B. D. Lindner, M. Schaffroth, *Angew. Chem. Int. Ed.* **2013**, *52*, 3810 – 3821.
[27] D. M. Gampe, S. Schramm, S. Ziemann, M. Westerhausen, H. Görls, P. Naumov, R. Beckert, *J. Org. Chem*. **2017**, *82*, 6153 – 6162.
[28] F. Stöckner, R. Beckert, D. Gleich, E. Birckner, W. Günther, H. Görls, G. Vaughan, *Eur. J. Org. Chem.* **2007**, *2007*, 1237 – 1243.
[29] P.-Y. Gu, Z. Wang, G. Liu, H. Yao, Z. Wang, Y. Li, J. Zhu, S. Li, Q. Zhang, *Chem. Mater*. **2017**, *29*, 4172 – 4175.
[30] J. Li, S. Chen, Z. Wang, Q. Zhang, *Chem. Rec.* **2016**, *16*, 1518 – 1530.
[31] Z. Liang, Q. Tang, J. Xu, Q. Miao, *Adv. Mater*. **2011**, *23*, 1535 – 1539.
[32] L. V. Brownell, K. Jang, K. A. Robins, I. C. Tran, C. Heske, D.-C. Lee, *Phys. Chem. Chem. Phys*. **2013**, *15*, 5967 – 5974.
[33] D. Cortizo-Lacalle, C. Gozalvez, M. Olano, X. Sun, M. Melle-Franco, L. E. Hueso, A. Mateo-Alonso, *Org. Lett*. **2015**, *17*, 5902 – 5905.
[34] P. Y. Gu, F. Zhou, J. Gao, G. Li, C. Wang, Q.-F. Xu, Q. Zhang, J.-M. Lu, *J. Am. Chem. Soc*. **2013**, *135*, 14086 – 14089.
[35] T. Qi, W. Qiu, Y. Liu, H. Zhang, X. Gao, Y. Liu, K. Lu, C. Du, G. Yu, D. Zhu, *J. Org. Chem.* **2008**, *73*, 4638 – 4643.
[36] Y. Akimoto, *Bull. Chem. Soc. Jpn.* **1956**, *29*, 460 – 464.
[37] U. H. F. Bunz, *Chem. Eur. J.* **2009**, *15*, 6780 – 6789.
[38] The changes in structure of the electronic absorption spectra upon PbO_2 oxidation of **1** and **2** are similar to those observed for substituted fluorubine derivatives described in Z. He, R. Mao, D. Liu, Q. Miao, *Org. Lett*. **2012**, *14*, 4190 – 4193.
[39] R. Rakhi, C. H. Suresh, *Phys. Chem. Chem. Phys*. **2016**, *18*, 24631 – 24641.
[40] D. M. Gambe, S. Schramm, M. Kaufmann, H. Görls, R. Beckert, *New J. Chem*. **2016**, *40*, 10100 – 10107.
[41] Q. Tang, D. Zhang, S. Wang, N. Ke, J. Xu, J. C. Yu, Q. Miao, *Chem. Mater.* **2009**, *21*, 1400 – 1405.
[42] M. Winkler, K. N. Houk, *J. Am. Chem. Soc.* **2007**, *129*, 1805 – 1815.
[43] A. Shchyrba, C. Wäckerlin, J. Nowakowski, S. Nowakowska, J. Björk, S. Fatayer, J. Girovsky, T. Nijs, S. C. Martens, A. Kleibert, M. Stöhr, N. Ballav, T. A. Jung, L. H. Gade, *J. Am. Chem. Soc*. 2014, 136, 9355 – 9363.
[44] M. Treier, C. A. Pignedoli, T. Laino, R. Rieger, K. Muellen, D. Passerone, R. Fasel. *Nature Chem*. **2011**, *3*, 61 – 67.
[45] Y. Zhao, C. Zhang, K. F. Chin, O. Pytela, G. Wei, H. Liu, F. Bureš, Z. Jiang, *RSC Adv.* **2014**, *4*, 30062 – 30067.
[46] X. Liu, X. Ye, F. Bureš, H. Liu, Z. Jiang, *Angew. Chem. Int. Ed.* **2015**, *54*, 11443 – 11447.
[47] C. Zhang, S. Li, F. Bureš, R. Lee, X. Ye, Z. Jiang, *ACS Catal.* **2016**, *6*, 6853 – 6860.
[48] G. Wei, C. Zhang, F. Bureš, X. Ye, C.-H. Tan, Z. Jiang, *ACS Catal.* **2016**, *6*, 3708 – 3712.
[49] Z. Hloušková, J. Tydlitát, M. Kong, O. Pytela, T. Mikysek, M. Klikar, N. Almonasy, M. Dvořák, Z. Jiang, A. Růžička, F. Bureš, *ChemistrySelect* **2018**, *3*, 4262 – 4270.
[50] A. G. Condie, J. C. Gonzáles-Gómez and C. R. J. Stephenson *J. Am. Chem. Soc.*, 2010, 132, 1464
[51] I. Horcas, R. Fernández, J. M. Gómez-Rodríguez, J. Colchero, J. Gomez-Herrero, A. M. Baro, *Rev. Sci. Instrum.* **2007**, *78*, 013705.

Entry for the Table of Contents (Please choose one layout)

Layout 1:

COMMUNICATION

Putting more 'N's in pentacene. Octaazatetracene and decaazapentacene chromophores have been successfully synthesized and their self-assembly and other properties studied. By scanning tunnelling microscopy, self-assembly and disassembly of molecular nanowire structures is coupled with the oxidation state of the oligoazaacene molecules.

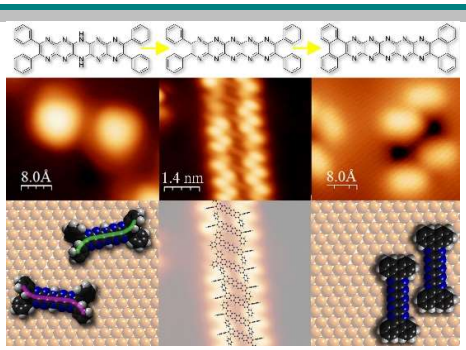

David Miklík, S. Fatemeh Mousavi, Zuzana Hloušková, Anna Middleton, Yoshitaka Matsushita, Jan Labuta, Aisha Ahsan, Luiza Buimaga-Iarinca, Paul A. Karr, Pavel Švec, Filip Bureš, Gary J. Richards, Toshiyuki Mori, Katsuhiko Ariga, Yutaka Wakayama, Cristian Morari, Francis D'Souza, Thomas A. Jung* and Jonathan P. Hill**

Page No. – Page No.

Oxidation-induced Self-assembly and Disassembly of a Reduced Decaazapentacene

Supporting Information

Oxidation-induced assembly and disassembly of a reduced decaazapentacene

David Miklík,[a],[b] S. Fatemeh Mousavi,[c] Zuzana Hloušková,[b] Anna Middleton,[d] Yoshitaka Matsushita,[e] Jan Labuta,[a] Aisha Ahsan,[c] Luiza Buimaga-Iarinca,[f] Paul A. Karr,[g] Pavel Švec,[a] Filip Bureš,[b] Gary J. Richards,[a],[h] Toshiyuki Mori,[i] Katsuhiko Ariga,[a],[j] Yutaka Wakayama,[a] Cristian Morari,[f] Francis D'Souza,*,[d] Thomas A. Jung*,[k] and Jonathan P. Hill*,[a]

[a] WPI Center for Materials Nanoarchitectonics and ⊥Fuel Cell Materials Group, National Institute for Materials Science, Namiki 1-1, Tsukuba, Ibaraki 305-0044, Japan.

[b] Institute of Organic Chemistry and Technology, Faculty of Chemical Technology, University of Pardubice, Studentská 573, Pardubice 53210, Czech Republic.

[c] Department of Physics, University of Basel, Klingelbergstrasse 82, 4056 Basel, Switzerland.

[d] Department of Chemistry, University of North Texas, 1155 Union Circle, 305070 Denton, Texas 76203, USA.

[e] Research Network and Facility Services Division, National Institute for Materials Science (NIMS), 1-2-1 Sengen, Tsukuba, Ibaraki 305-0047, Japan.

[f] National Institute for Research and Development of Isotopic and Molecular Technologies (NIRDIMT) 65-103 Donath, Ro-400293, Cluj-Napoca, Romania.

[g] Department of Physical Sciences and Mathematics, Wayne State College, 111 Main Street, Wayne, Nebraska, 68787, USA.

[h] Department of Chemistry, Ochanomizu University, Otsuka 2-1-1, Bunkyo-ku, Tokyo 112-8610, Japan.

[i] Center for Green Research on Energy and Environmental Materials, National Institute for Materials Science, Namiki 1-1, Tsukuba, Ibaraki 305-0044, Japan

[j] Graduate School of Frontier Sciences, The University of Tokyo, Kashiwa 277-0827, Japan.

[k] Laboratory for Micro- and Nanotechnology, Paul Scherrer Institute, 5232 Villigen PSI, Switzerland.

E_mail: francis.dsouza@unt.edu; thomas.jung@psi.ch; jonathan.hill@nims.go.jp

Contents

1.0 Experimental

General. Reagents and dehydrated solvents (in septum-sealed bottles) used for syntheses and spectroscopic measurements were obtained from Tokyo Kasei Chemical Co., Wako Chemical Co. or Aldrich Chemical Co. and were used without further purification. Electronic absorption spectra were measured using JASCO V-570 UV/Vis/NIR spectrophotometer, Princeton Applied Research (PAR) diode array rapid scanning spectrometer or a Shimadzu UV/Visible spectrophotometer. Fluorescence spectra were measured using a JASCO FP-670 spectrofluorimeter. FTIR spectra were obtained from samples deposited on a barium fluoride disc using a Thermo-Nicolet 760X FTIR spectrophotometer. ^{1}H and ^{13}C NMR spectra were obtained using JEOL AL300BX (^{1}H: 300 MHz; ^{13}C: 75 MHz) or Bruker Avance 600 MHz (^{1}H: 600 MHz; ^{13}C: 150 MHz) spectrometers using tetramethylsilane as an internal standard. MALDI-TOF mass spectra were measured using a Shimadzu Axima AFR+ mass spectrometer with dithranol as matrix. High resolution MALDI-TOF mass spectra were measured using an LTQ Orbitrap XL system using 2,5-dihydroxybenzoic acid as matrix. Computational geometry optimizations were performed at the B3LYP/6-311+G(d,p) level using NWChem.[S1] GaussView program of GAUSSIAN[S2] was used to generate frontier HOMO and LUMO orbitals. 5,6-Diphenyl-2,3-diaminopyrazine (**6**) was prepared according to a reported procedure.[S3]

Electrochemistry. Cyclic voltammograms were recorded on an EG&G Model 263A potentiostat using a three electrode system. A platinum button electrode was used as the working electrode. A platinum wire served as the counter electrode and an Ag/AgCl electrode was used as the reference. Ferrocene/ferrocenium redox couple was used as an internal standard. All the solutions were purged prior to electrochemical and spectral measurements using argon gas. Spectroelectrochemical study was performed by using a cell assembly (SEC-C) supplied by ALS Co., Ltd. (Tokyo, Japan). This assembly comprised of a Pt counter electrode, a 6 mm Pt Gauze working electrode, and an Ag/AgCl reference electrode in a 1.0 mm path length quartz cell. The optical transmission was limited to 6 mm covering the Pt gauze working electrode.

X-ray Crystallography. Crystals of **2** were grown by diffusion of hexane into a solution of **2** in tetrahydrofuran. Data collections were performed using MoK_{α} radiation (λ = 0.71073 Å) on a RIGAKU VariMax Saturn diffractometer equipped with a CCD detector. Prior to the diffraction experiment the crystals were flash-cooled to 213 K in a stream of cold N_2 gas. Cell refinements and data reductions were carried out by using the d*trek program package in the CrystalClear software suite.[S4] The structures were solved using a dual-space algorithm

method (SHELXT)[S5] and refined by full-matrix least squares on F2 using SHELXL-2014[S6] in the WinGX program package.[S7] Non-hydrogen atoms were anisotropically refined and hydrogen atoms were placed on calculated positions with temperature factors fixed at 1.2 times U_{eq} of the parent atoms and 1.5 times U_{eq} for methyl groups. Crystal data for **2**: orange bar, $C_{42}H_{34}N_8O_2$, M_r = 682.77, monoclinic P21/n, a = 15.6972(4) Å, b = 5.71170(10) Å, c = 19.7826(6) Å, β = 106.4810(10)°, V = 1700.79(7) Å^3, T = 213 K, Z = 2, R_{int} = 0.0428, GoF = 1.063, R_1 = 0.0793, wR(all data) = 0.2500. Crystallographic data (excluding structure factors) have been deposited with the Cambridge Crystallographic Data Centre with CCDC reference number 1576267 (**2**). Copies of the data can be obtained, free of charge, on application to CCDC, 12 Union Road, Cambridge CB2 1EZ, UK http://www.ccdc.cam.ac.uk/perl/catreq/catreq.cgi, e-mail: data_request@ ccdc.cam.ac.uk, or fax: +44 1223 336033.

Scanning Tunneling Microscopy. All sample preparations were performed under ultrahigh vacuum (UHV) conditions with a base pressure of ~10^{-10} mbar. The crystals were cleaned using cycles of sputtering with Ar+ ions with subsequent annealing at 450 °C. Thermal evaporation at 300 °C was used to deposit the molecules on the substrate using a commercial evaporator (Kentax GmbH, Germany). The sublimed amounts of the compounds were controlled by using a quartz crystal microbalance. STM imaging was performed in constant current mode (typical tunneling current 10 – 50 pA) with the selected sample bias in the range of 300 mV to 1 V at 5K. Pt-Ir wires (90 % Pt, 10 % Ir) were used to make scanning probe tips and these were cleaned by sputtering with Ar+ ions prior to use.

In Situ X-ray Photoelectron Spectroscopy. XPS was used at room temperature to track the N1s chemical environment changes of the compounds before and after annealing steps. The spectra were recorded in normal emission with an instrumental setup that gives a full width at half-maximum (FWHM) of 1.0 eV using a monochromatized Al Kα X-ray source.

DFT Simulation of on-surface structures for compound 2. Simulations were performed using the Siesta code.[S89-S10] This uses norm-conserving pseudopotentials[S11] and expands the wave functions of valence electrons in LCAO form. The relaxation procedure involves the Conjugated Gradient method. As exchange-correlation functional, we have used the van der Waals functional as implemented by Berland and Hyldgaard (BH).[S12] The systems were constructed based on the experimental bulk parameter for copper (i.e. 3.62; we have tested the bulk parameter in the BH functional framework. The computed value was 3.64, indicating an error below 0.6%. This

allows us to construct models based on the experimental value). The systems were confined to unit cells that allow the study of periodically repeating Cu(111) surface features, and included 3 atomic layers. The super-cell sizes vary from 7 x 10 Cu atoms for monomers to 12 x 12 Cu atoms for dimers. The length of the cells along the OZ axis was 30 Å for all systems, thus allowing a vacuum level of 20 Å, which we consider large enough to avoid the artificial influence of the electric charge from one cell to another. The Monkhorst-Pack grid for the integrals in the Brillouin zone was 2 x 2 x 1. We used double-zeta polarized (DZP) basis sets with an energy shift of 100 meV for all atoms. This setup allows production of orbitals with larger cutoff-radii for accurate simulation of long-range interactions. Since the difference between the calculated bulk parameter and the experimental value is reasonably small, the systems were relaxed by keeping the deeper layer of the copper substrate pinned at their starting positions, with only the upper layer and the molecule being permitted to relax. In Model 2-dimer, we also allowed the relaxation of the Cu ad-atom. The systems were allowed to reach the local minima until the maximum gradient in the relaxed structure was below 0.1 eV/A for monomers and below 0.2 eV/A for dimers. Simulations of the STM images were perfomred by using the Tersoff-Hamman approximation. This method considers that an STM image is determined by the local density of states (LDOS).[S13] We computed LDOS in the energy window spanning from the Fermi level of the system up to 1 eV below the Fermi level, corresponding to an external bias of 1V. Next, we scanned the surface by searching for a given constant value of the LDOS (i.e. a "constant current" STM experiment). The values used in calculations are given in Figure 3 of reference [S13].

2.0 Synthesis

2,3-Dichloro-6,7-diphenyl-1,4,5,8-tetraazanaphthalene (X = Cl, **3**). Benzil (210 mg, 1 mmol) and 2,3-diamino-5,6-dichloropyrazine (190 mg, 1.05 mmol) were dissolved in a mixture of dry 1,4-dioxane (10 mL) and glacial acetic acid (2 mL). The solution was heated under reflux for 12 h. The reaction mixture was allowed to cool then poured into 150 mL of water followed by partitioning of the resulting mixture with DCM (2 × 40 mL). The combined extracts were washed with 30 mL of brine, dried over anhydrous Na_2SO_4 then the solvents were evaporated under reduced pressure. The residue was purified by column chromatography (silica, DCM) to give the product as a yellow crystalline solid. Yield: 307 mg (87 %). ^{1}H NMR (300 MHz, $CDCl_3$, 25 °C) □ = 7.34 – 7.4 (m, 4 H, Ar*H*), 7.43 – 7.48 (m, 2H, Ar*H*), 7.63 – 7.67 (m, 4 H, Ar*H*) ppm. ^{13}C NMR (75 MHz, $CDCl_3$, 25 °C) □ = 128.5, 130.2, 130.4, 137.0, 142.2, 149.2, 158.2 ppm. FTIR (ATR) $\tilde{\nu}$= 3109, 3075, 2918, 2849, 2558, 1557, 1451, 1401, 1338, 1244, 1234, 1163, 1082, 1068, 1007, 968 cm^{-1}. HR-MALDI-MS (DHB): m/z calc. for $C_{18}H_{10}Cl_2N_4$ $[M]^+$: 352.0283; found 352.0283.

2,3-Diamino-6,7-diphenyl-1,4,5,8-tetraazanaphthalene, **7**. Dry ammonia gas was bubbled through a solution of 2,3-dichloro-6,7-diphenyl-1,4,5,8-tetraazanaphthalene (200 mg, 0.57 mmol) in DMF (7 mL) for 15 min at RT. The reaction mixture was then heated at 90°C in a sealed tube for 12 h. Solvents and excess ammonia were then removed under reduced pressure. The solid residue was ultrasonicated with water (20 mL), the solid was filtered, washed with ethyl-acetate (20 mL) then hexane (20 mL) giving the product as a yellow crystalline solid. Yield: 100 mg (56 %). ^{1}H NMR (300 MHz, DMSO-d_6, 25 °C) □ = 7.29 – 7.31 (m, 6H, Ar*H*), 7.35 – 7.39 (m, 4H, Ar*H*), 7.45 (br s, 4H, NH_2) ppm. ^{13}C NMR (75 MHz, DMSO-d_6, 25 °C) □ = 127.7, 127.8, 129.6, 139.5, 141.5, 146.8, 148.3 ppm. FTIR (ATR) $\tilde{\nu}$□= 3452, 3314, 3222, 3138, 2028, 1628, 1470, 1381, 1212, 1070, 1025 cm^{-1}. HR-MALDI-MS (DHB): m/z $[M + 2H]^+$ calcd for $C_{18}H_{14}N_6$: 316.1431; found 316.1429.

2,3-Dichloro-6,7-di(4-tert-butylphenyl)-1,4,5,8-tetraazanaphthalene. 4,4′-Di-tert-butylbenzil (323 mg, 1 mmol) and 2,3-diamino-5,6-dichloropyrazine (190 mg, 1.05 mmol) were dissolved in a mixture of dry 1,4-dioxane (10 mL) and glacial acetic acid (2 mL). The solution was heated under reflux for 12 h. The reaction mixture was then allowed to cool, poured into water (150 mL) and extracted with DCM (40 mL). The extract solution was washed with of brine (30 mL), dried over ahydrous Na_2SO_4, then solvents were evaporated under reduced pressure and the residue was purified by column chromatography (silica; DCM, hexane 5/1) to give the product as a yellow crystalline solid. Yield: 255 mg (55 %). ^{1}H NMR (300 MHz, $CDCl_3$, 25 °C) □ = 1.31 (s, 18H, C*H*$_3$), 7.38 (d, ^3J = 8.4 Hz, 4H, Ar*H*), 7.63 (d, ^3J = 8.4 Hz, 4H, Ar*H*) ppm. ^{13}C NMR (75 MHz, $CDCl_3$, 25 °C) □ = 31.2, 34.9, 125.4, 130.0, 134.3, 142.1, 148.7, 154.1, 158.1 ppm. FTIR (ATR) $\tilde{\nu}$□= 2962, 2926, 2868, 1729, 1604, 1461, 1333, 1235, 1166, 1112, 1008 cm^{-1}. HR-MALDI-MS (DHB): m/z $[M]^+$ calcd for $C_{26}H_{26}Cl_2N_4$: 466.1691; found 466.1692.

2,3-Diamino-6,7-di(4-tert-butylphenyl)-1,4,5,8-tetraazanaphthalene. Dry ammonia gas was bubbled through a solution of 2,3-dichloro-6,7-di(4-tert-butylphenyl)-1,4,5,8-tetraazanaphthalene (300 mg, 0.65 mmol) in DMF (10 mL) for 15 min at RT. The reaction mixture was heated at 90°C in a sealed tube for 12 h. Solvents and excess ammonia solution was removed using reduced pressure. The product was isolated using column chromatography (silica; $CHCl_3$, 8% MeOH) to give product like a yellow crystalline solid. Yield: 125 mg (45 %). ^{1}H NMR (300 MHz, DMSO-*d*$_6$, 25 °C) □ = 1.33 (s, 18H, C*H*$_3$), 7.34 – 7.43 (m, 12H, Ar*H* + N*H*$_2$) ppm. ^{13}C NMR (75 MHz, $CDCl_3$, 25 °C) □ = 31.0, 34.1, 124.42, 129.1, 136.7, 141.2, 146.6, 148.1, 150.1 ppm. FTIR (ATR) $\tilde{\nu}$□= 3435, 3316, 3235, 2959, 2864, 1700, 1520, 1435, 1365, 1333, 1268, 1207, 1117, 1016 cm^{-1}. HR-MALDI-MS (DHB): m/z $[M + 2H]^+$ calcd for $C_{26}H_{30}N_6$: 428.2688; found 428.2677.

5,12-Dihydro-2,3,8,9-tetraphenyl-1,4,5,6,7,10,11,12-octaazatetracene, **2**. A mixture of 2,3-dichloro-6,7-diphenyl-1,4,5,8-tetraazanaphthalene (106 mg, 0.3 mmol), 2,3-diamino-5,6-diphenylpyrazine (95 mg, 0.36 mmol) and K_2CO_3 (138 mg, 1 mmol) in DMSO (5 mL) was heated for 3 h at 110 °C. The reaction mixture was allowed to cool to room temperature then poured into saturated aqueous ammonium chloride solution (30 mL) and extracted with chloroform (3 × 50 mL). The combined extracts were washed with brine (100 mL), dried over anhydrous Na_2SO_4 then solvents evaporated under reduced pressure. The product was isolated using column chromatography (SiO_2; $CHCl_3$, 8 % THF) to give the product as an orange crystalline

solid. Yield: 70 mg (43 %). UV-Vis (CH_2Cl_2): λ_{max} (ε) = 249 (77000), 441 (39500), 461 (67000), 489 (46000) nm. ^{1}H NMR (300 MHz, THF-*d8*, 25 °C) δ = 7.14 – 7.22 (m, 12H, ArH), 7.33 – 7.36 (m, 8H, ArH), 10.94 (br. s, 2H, NH) ppm. ^{13}C NMR (75 MHz, CF_3COOD, 25 °C) δ = 131.3, 131.5, 133.2, 134.1, 142.3, 149.3, 152.0 ppm. FT-IR (BaF_2) $\tilde{\nu}$ = 3639, 2956, 2924, 2854, 1522, 1445, 1429, 1406, 1368, 1185, 1088, 1026, 984, 762, 695 cm^{-1}. HR-MALDI-MS (DHB): m/z $[M + 2H]^+$ calcd for $C_{34}H_{24}N_8$: 544.2118; found 544.2140.

6,13-Dihydro-2,3,9,10-tetraphenyl-1,4,5,6,7,8,11,12,13,14-decaazapentacene, **1**. A mixture of 2,3-dichloro-6,7-diphenyl-1,4,5,8-tetraazanaphthalene (106 mg, 0.3 mmol), 2,3-diamino-6,7-diphenyl-1,4,5,8-tetraazanaphthalene (104 mg, 0.33 mmol) and K_2CO_3 (138 mg, 1 mmol) in DMSO (5 mL) was heated for 4 h at 120 °C. The reaction mixture was allowed to cool to room temperature then poured into aqueous saturated ammonium chloride solution (30 mL) and filtered. The filtrate was dissolved in THF, the resulting solution passed through a short plug of silica then the solvents were evaporated under reduced pressure. Ethyl acetate (20 mL) was added to the resulting solid followed by ultrasonication of the suspension for 10 min. The suspension was filtered, rinsed with water (50 mL), hot ethyl-acetate (10 mL), dichloromethane (10 mL) and dried under reduced pressure to give the product as a red crystalline solid. Yield: 63 mg (35 %). UV-Vis (CH_2Cl_2): λ_{max} (ε) = 252 (75100), 470 (73500), 502 (108000) nm. ^{1}H NMR (300 MHz, CF_3COOD, 25 °C) δ = 7.05 – 7.08 (m, 8H, ArH), 7.15 – 7.17 (m, 8H, ArH) ppm. ^{13}C NMR (75 MHz, CF_3COOD, 25 °C) δ = 131.6, 132.2, 133.5, 135.4, 143.0, 147.9, 155.6 ppm. FT-IR (BaF_2): $\tilde{\nu}$ = 3631, 3384, 3085, 2948, 1580, 1507, 1445, 1192, 1089, 1026, 696 cm^{-1}. HR-MALDI-MS (DHB): m/z $[M + H]^+$ calcd for $C_{34}H_{23}N_{10}$: 595.2107; found: 595.2101.

6,13-Dihydro-2,3,9,10-tetrakis(4-t-butylphenyl)-1,4,5,6,7,8,11,12,13,14-decaazapentacene, **1**-tBu. A mixture of 2,3-Dichloro-6,7-bis(4-tert-butylphenyl)-1,4,5,8-tetraazanaphthalene (140 mg, 0.3 mmol), 2,3-Diamino-6,7-bis(4-tert-butylphenyl)-1,4,5,8-tetraazanaphthalene (141 mg, 0.33 mmol) and K_2CO_3 (138 mg, 1 mmol) in DMSO (5 mL) was heated for 4 h at 120 °C. The reaction mixture was allowed to cool to room temperature, poured into aqueous saturated ammonium chloride solution (30 mL) then the mixture extracted with $CHCl_3$ (3 × 50 mL). The combined extracts were washed with brine (50 mL), dried over anhydrous Na_2SO_4 then solvents were evaporated under reduced pressure. The solid residue was purified using column chromatography (SiO_2; $CHCl_3$, 8 % THF) to give the product as a dark purple crystalline solid. Yield: 110 mg (45 %). UV-Vis: λ_{max} (ε) = 231 (31400), 268 (22800), 571 (51700), 606 nm (60500). ^{1}H NMR (300 MHz,

THF-d_8, 25 °C): δ = 7.25 – 7.30 (m, 8H, ArH), 7.40 – 7.45 (m, 8H, ArH), 11.61 (br. s, 2H, NH) ppm. ^{13}C NMR (75 MHz, CF_3COOD, 25 °C) δ = 31.7, 36.9, 128.5, 130.2, 131.8, 142.37, 147.3, 155.5, 160.8 ppm. FT-IR (BaF_2) $\tilde{\nu}$ = 3213, 3129, 3051, 2960, 2924, 2855, 1607, 1542, 1442, 1286, 1190, 1116, 1077, 1016 cm^{-1}. HR-MALDI-MS (DHB): m/z $[M + H]^+$ calcd for $C_{52}H_{55}N_{10}$: 819.4611; found: 819.4609.

General procedure for oxidation. Dihydroazaacene derivative (0.001 mmol) was dissolved in dry dichloromethane (3 mL) and lead (IV) oxide (50 wt%) was added. The reaction mixture was stirred for 10 min. then filtered through Celite and solvents evaporated under reduced pressure to give the products as solids in quantitative yields.

2,3,8,9-Tetraphenyl-1,4,5,6,7,10,11,12-octaazatetracene, **2**-ox. Dark purple solid. ^{1}H NMR (300 MHz, CD_2Cl_2, 25 °C): δ = 7.45 – 7.50 (m, 8H, ArH), 7.56 – 7.61 (m, 8H, ArH), 7.82 – 7.86 (m, 8H, ArH) ppm. ^{1}H NMR (600 MHz, $CDCl_3$, 25 °C): δ = 7.47 (m, 8H, ArH), 7.58 (m, 4H, ArH), 7.87 (m, 8H, ArH) ppm. ^{13}C NMR (150 MHz, $CDCl_3$, 25 °C): δ = 128.6, 130.8, 131.8, 137.1, 147.0, 147.8, 162.6 ppm. FT-IR (BaF_2) $\tilde{\nu}$ = 3051, 2916, 2848, 1593, 1540, 1427, 1366, 1130, 768, 698, 693 cm^{-1}. HR-MALDI-MS (DHB): m/z $[M + H]^+$ calcd for $C_{34}H_{21}N_8$: 541.1889; found: 541.1888.

2,3,9,10-Tetraphenyl-1,4,5,6,7,8,11,12,13,14-decaazapentacene, **1**-ox. Dark red solid. FT-IR (BaF_2) $\tilde{\nu}$ = 2947, 2865, 1580, 1539, 1445, 1192, 1089, 1070, 697 cm^{-1}. HR-MALDI-MS (DHB): m/z $[M + H]^-$ calcd for $C_{36}H_{21}N_{10}$: 593.1951; found 593.2013.

2,3,9,10-Tetrakis(4-t-butylphenyl)-1,4,5,6,7,8,11,12,13,14-decaazapentacene, **1**-tBu-ox. Dark purple solid. ^{1}H NMR (300 MHz, CD_2Cl_2, 25 °C): δ = 1.40 (s, 36H, CH_3), 7.52 (d, ^3J = 9 Hz, 8H, ArH), 7.88 (d, ^3J = 9 Hz, 8H, ArH) ppm. ^{13}C NMR (75 MHz, CD_2Cl_2, 25 °C) δ = 30.9, 35.2, 125.8, 130.9, 134.6, 148.6, 148.7, 156.8, 163.8 ppm. FT-IR (BaF_2) ν = 3067, 2962, 2904, 2868, 1603, 1505, 1407, 1340, 1304, 1196, 1097, 1062, 831, 704 cm^{-1}. HR-MALDI-MS (DHB): m/z $[M + H]^-$ calcd for $C_{52}H_{53}N_{10}$: 817.4460; found 817.4432.

3.0 Physical appearances of 1 and 2

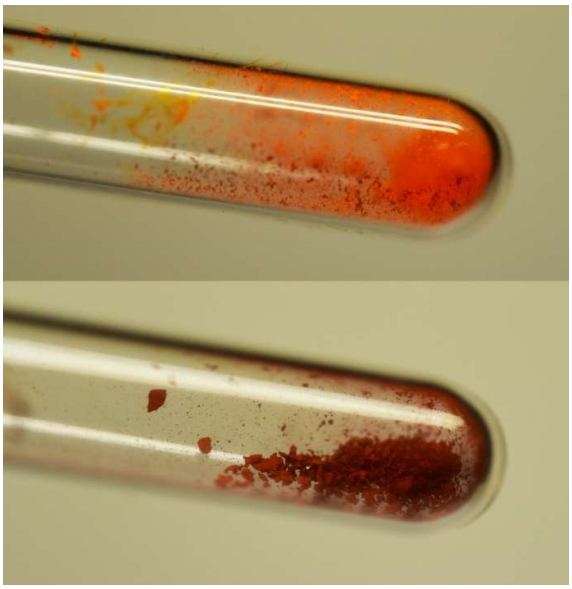

Figure S1. Photographs of samples of **2** (upper) and **1** (lower) illustrating the colours of the compounds.

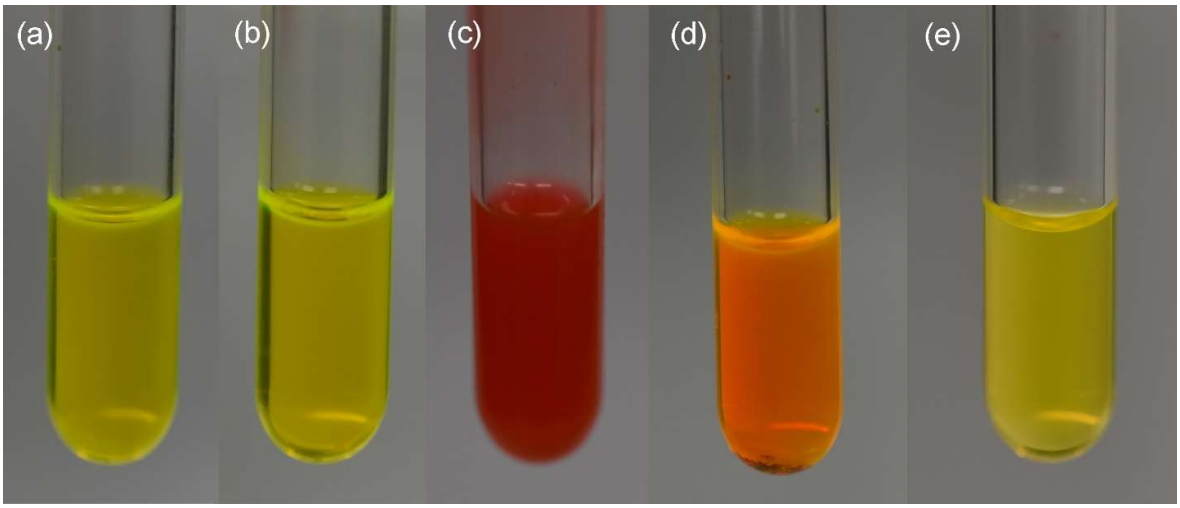

Figure S2. Photographs of solutions of (a) **2** (CH_2Cl_2), (b) **2** (THF), (c) **1** (CH_2Cl_2), (d) **1** (THF), (e) **1** (dilute, CH_2Cl_2). **1** is aggregated in CH_2Cl_2 at high concentration and its fluorescence is quenched. **1** and **2** are solvatochromic dyes. Details will be reported elsewhere.

4.0 Electronic absorption spectra for 1-ox and 2-ox

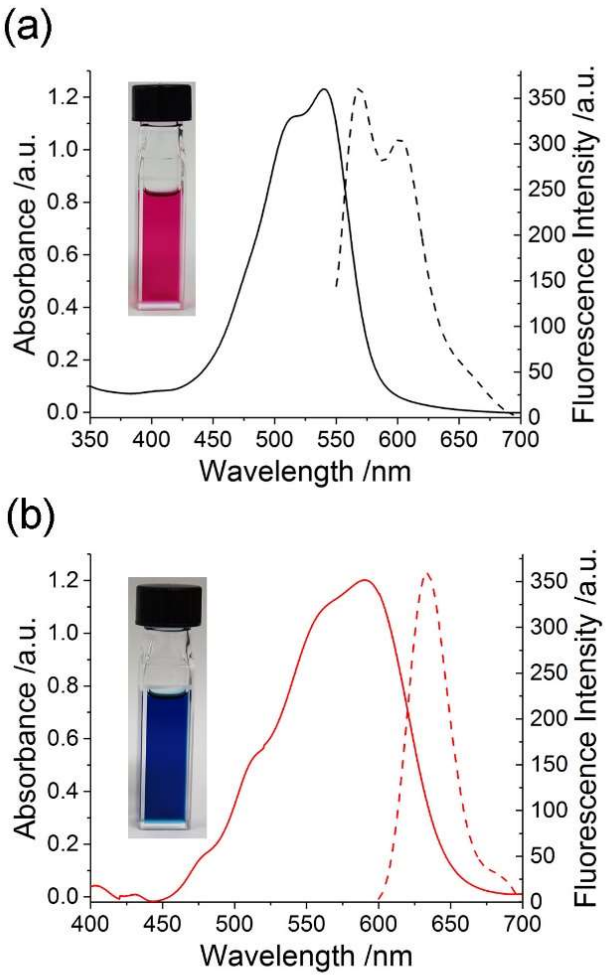

Figure S3. UV/Vis and fluorescence spectra of (a) **2**-ox and (b) **1**-ox.

5.0 Electrochemical Reduction of 2-ox.

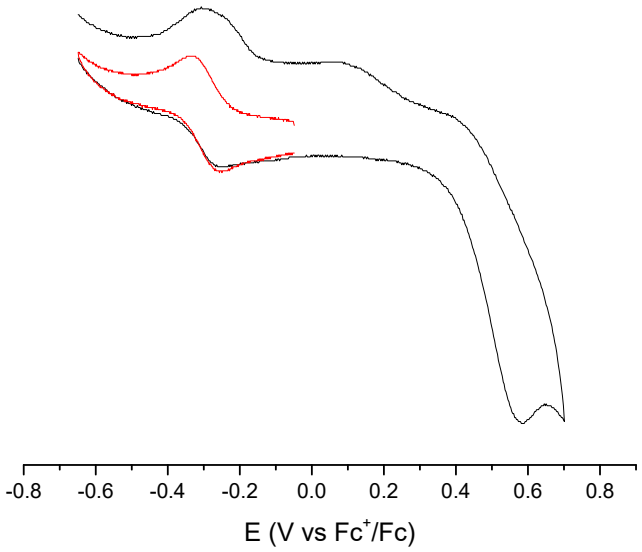

Figure S4. Cyclic voltammetry for **2**-ox revealing a first reduction at -0.293 V. **1**-ox could not be obtained in a form suitable for electrochemical measurements.

6.0 DFT-generated structures

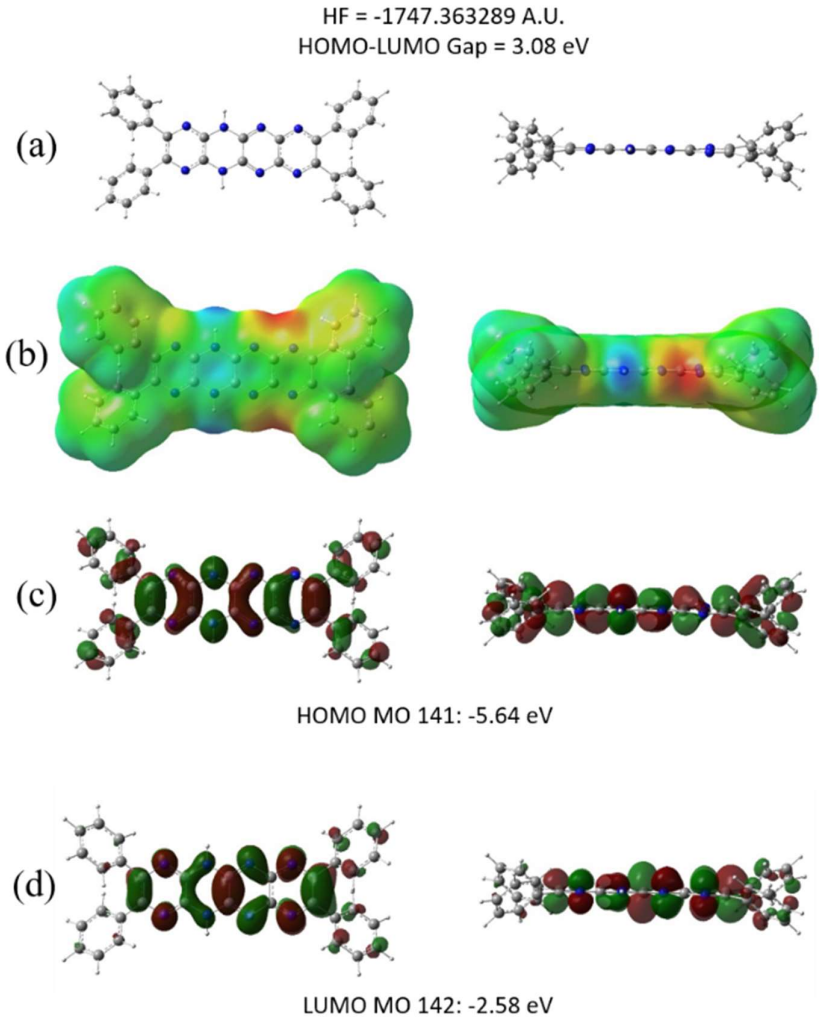

Figure S5. DFT calculations for compound **2**. (a) Molecular structure. (b) Surface charge. (c) Highest occupied molecular orbital (HOMO), and (d) lowest unoccupied molecular orbital (LUMO).

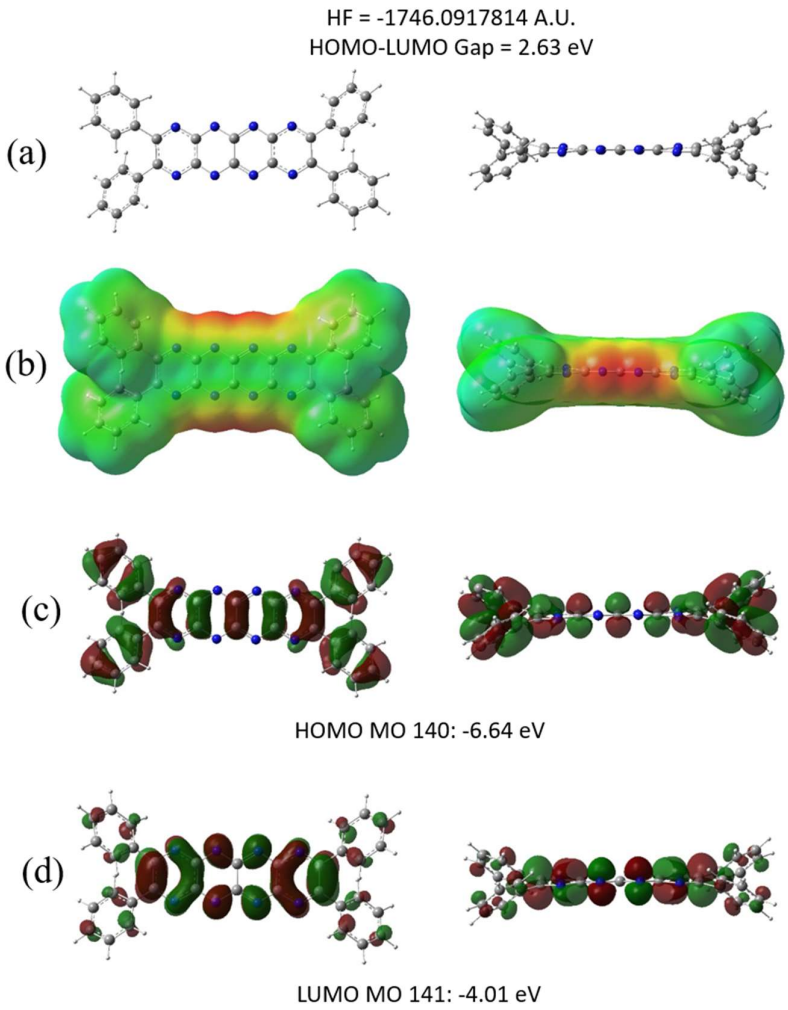

Figure S6. DFT calculations for compound **2**-ox. (a) Molecular structure. (b) Surface charge. (c) Highest occupied molecular orbital (HOMO), and (d) lowest unoccupied molecular orbital (LUMO).

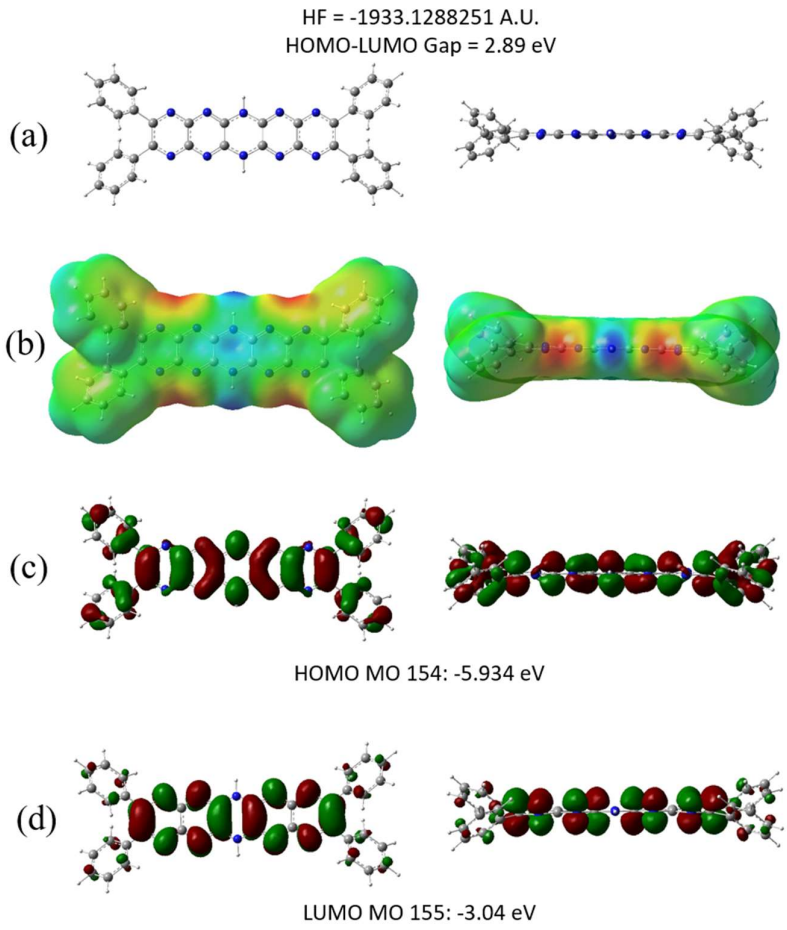

Figure S7. DFT calculations for compound **1**. (a) Molecular structure. (b) Surface charge. (c) Highest occupied molecular orbital (HOMO), and (d) lowest unoccupied molecular orbital (LUMO).

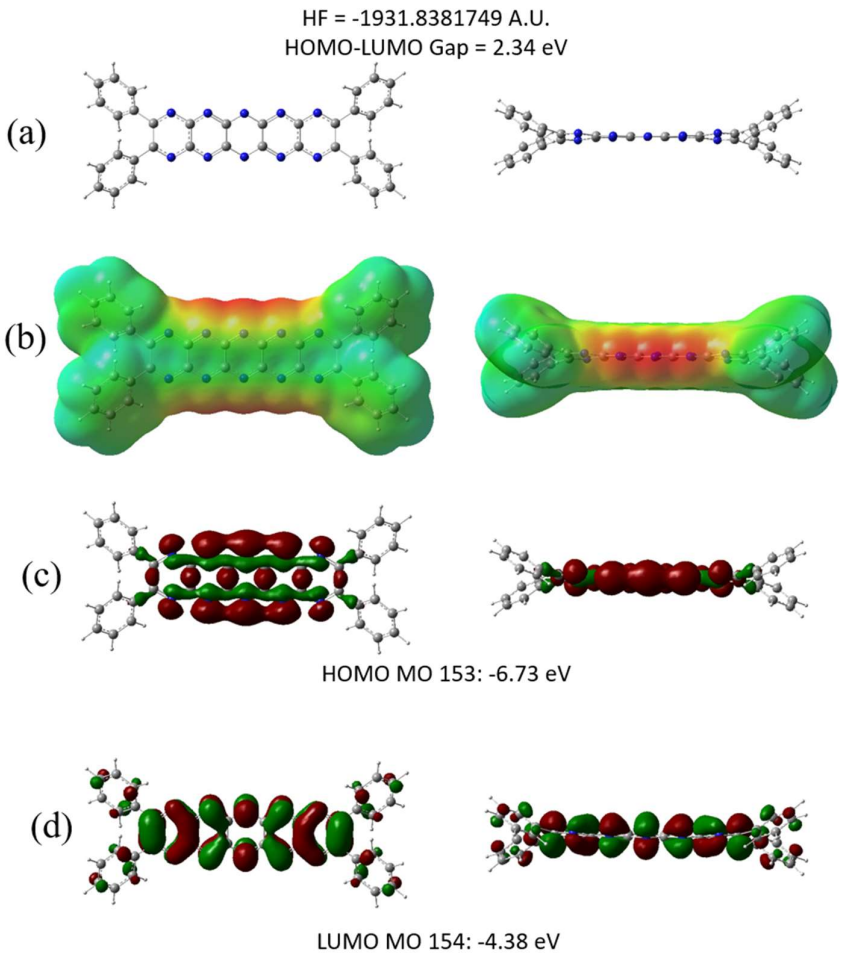

Figure S8. DFT calculations for compound **1**-ox. (a) Molecular structure. (b) Surface charge. (c) Highest occupied molecular orbital (HOMO), and (d) lowest unoccupied molecular orbital (LUMO).

7.0 Titration of 1 with DBU.

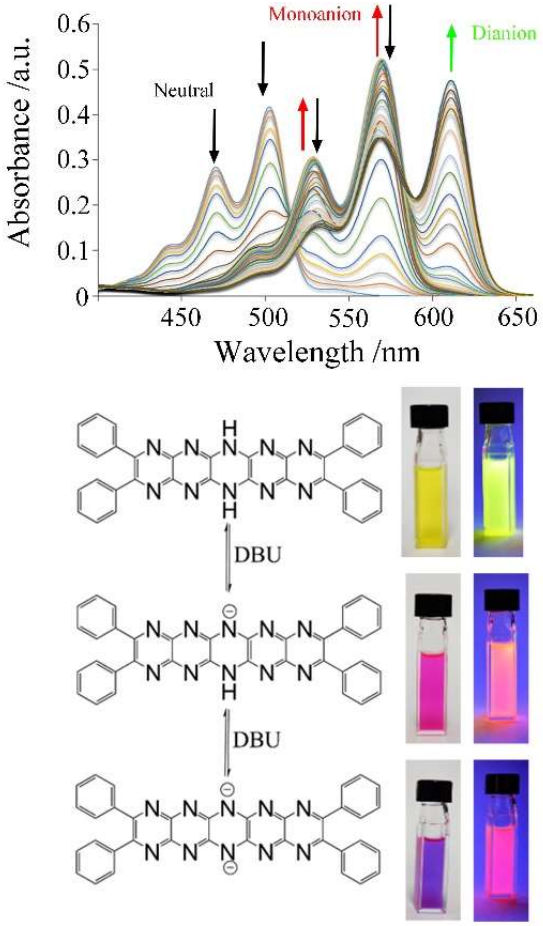

Figure S9. UV/Vis titration of 1 with 1,8-diazabicyclo[5.4.0]undec-7-ene (DBU). Spectral changes can be fit according to a double deprotonation process with easy first deprotonation ($K_1 > 3 \times 10^7$ M^{-1}) and more difficult second process ($K_2 = 1.7 (\pm 0.1) \times 10^6$ M^{-1}). Proposed chemical structures and photographs of the solutions obtained during titration are also given for samples under daylight and under UV light (λ_{ex} = 365 nm).

7.1 Titration of 2 with DBU.

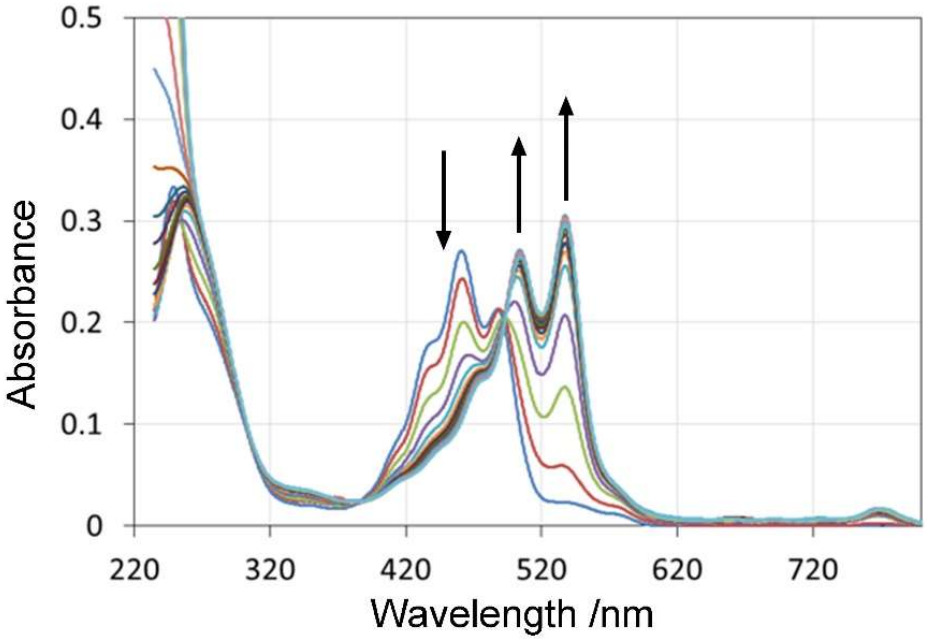

Figure S10. Titration of **2** with DBU. Spectral changes can be fit according to a double deprotonation process with very easy first deprotonation ($K_1 = 1 \times 10^7$ M^{-1}) and more difficult second process ($K_2 = 1.7 (\pm 0.1) \times 10^6$ M^{-1}).

8.0 STM images and in situ XPS data for compound 1

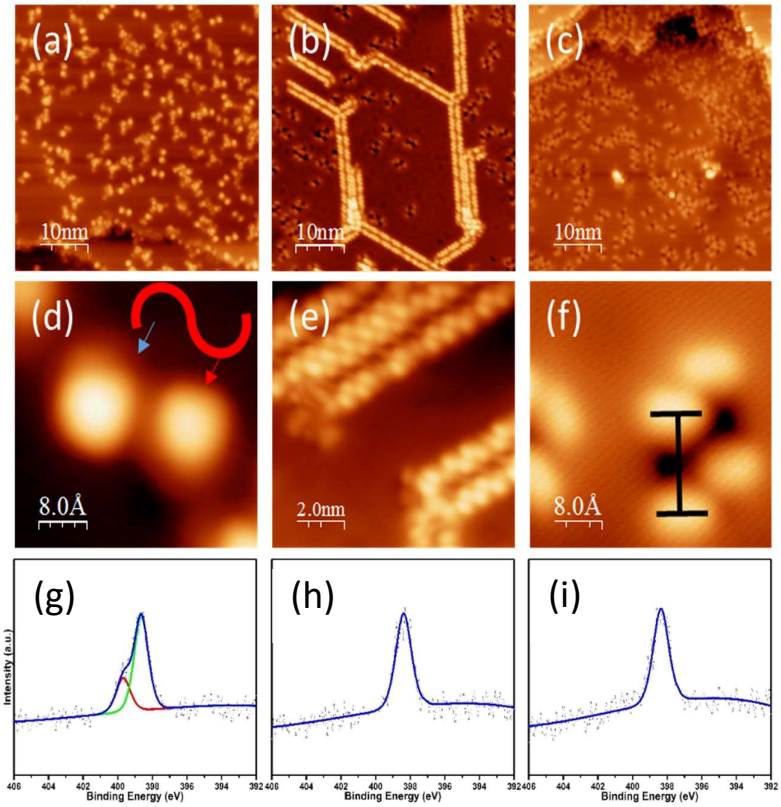

Figure S11. Scanning tunneling micrographs of **1** on Cu(111). (a) **1** distributed as found, predominantly with a double-lobe form. In contrast to **2**, other forms can also be found at low concentration and are largely eliminated following subsequent annealing. (b) Line structures formed upon annealing of **1** at 300°C on Cu(111). (c) Double-lobed two-dark-spot structures dominate after annealing above 300°C. (d-f) Magnified images of (a-c), respectively. Note the narrow line depicting the molecular backbone, e.g. in Fig. 6e. (d) Chiral double-spot profile of **1** similar to that found for **2** (Figure 3(d)). (e) Line structures with phenyls and acene backbones clearly recognizable. (f) Double-lobed/two-dark-spot structure obtained for **1** due to dehydrogenation/cyclodehydrogenation (see main text). (g-i) N1s XP spectra of **1** on Cu(111): (g) as-deposited as in (a),(d); (h) after annealing at 300°C as in (b),(c); (i) after annealing above 300°C as in (c),(f). STM data information: (a) 50nm x 50nm, 10pA, 1V. (b) 50nm x 50nm, 50pA, 300mV. (c) 50nm x 50nm, 10pA, 1V. (d) 4nm x 4nm, 10pA, 1V. (e) 10nm x 10nm, 50pA, 300mV. f) 4nm x 4nm, 50pA, 300mV.

9.0 Analysis of surface chirality for 2

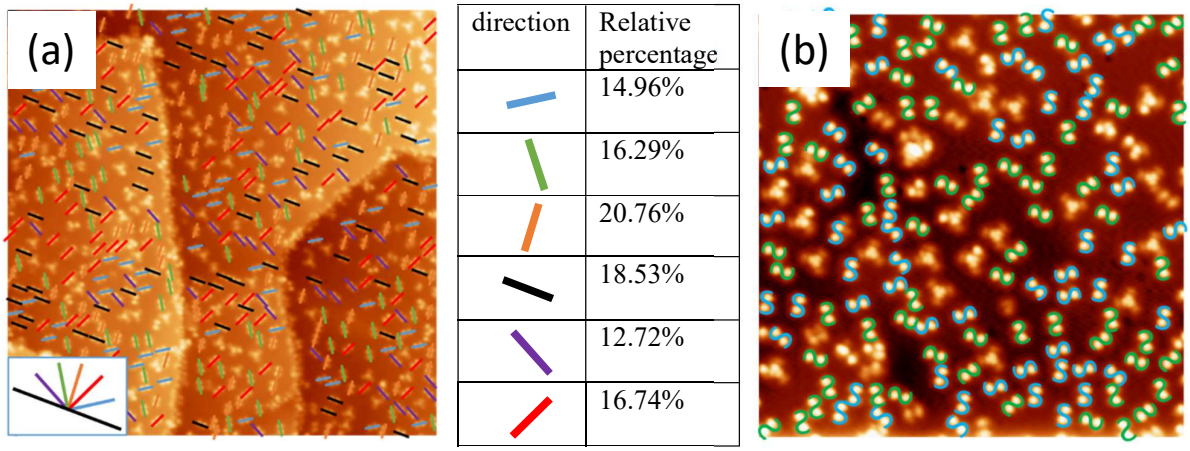

Figure S12. a) Molecules align along six directions on the threefold symmetric Cu(111) substrate. This implies that the 2 chiral conformers take a mirror orientation along the 3 principal directions of the substrate. Note that the determination of the angles is of limited precision. In the table on the right the number of molecules oriented in one or the other direction has been listed. b) Chirality identification. Molecules are adsorbed in two different chiral conformations and have been marked with blue and green 'S' and mirror 'S' features depicting the molecules of opposing chirality. Both enantiomers are present with about equal probability. Figure information: a) 100 nm x 100 nm; 10 pA, 1 V; b) 50 nm x 50 nm; 10 pA, 1 V.

10.0 STM images of 2 after keeping the sample at room temperature for 24 h on Cu(111)

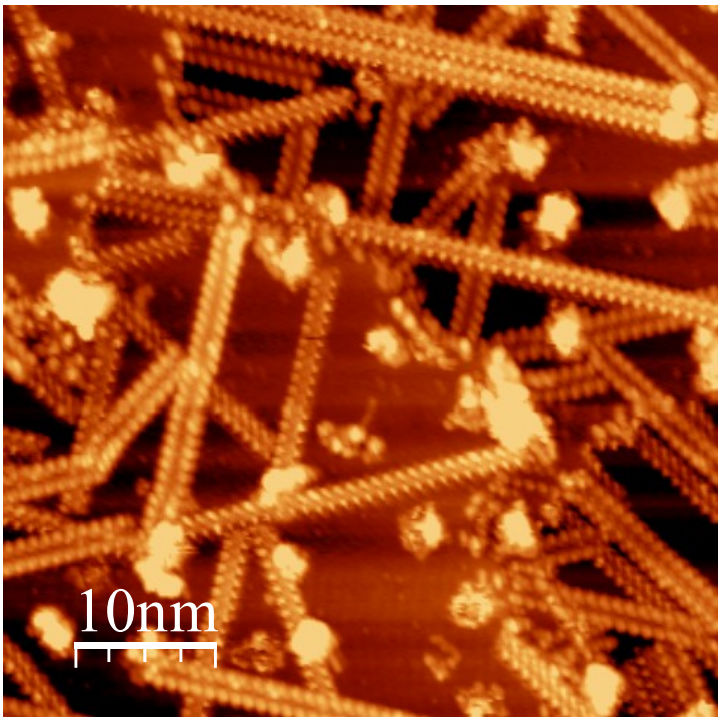

Figure S13. STM images of **2** on Cu(111) after a period of 24 h at ambient temperature revealing that line formation occurs even at low temperatures.

11.0 Packing model for the line structure

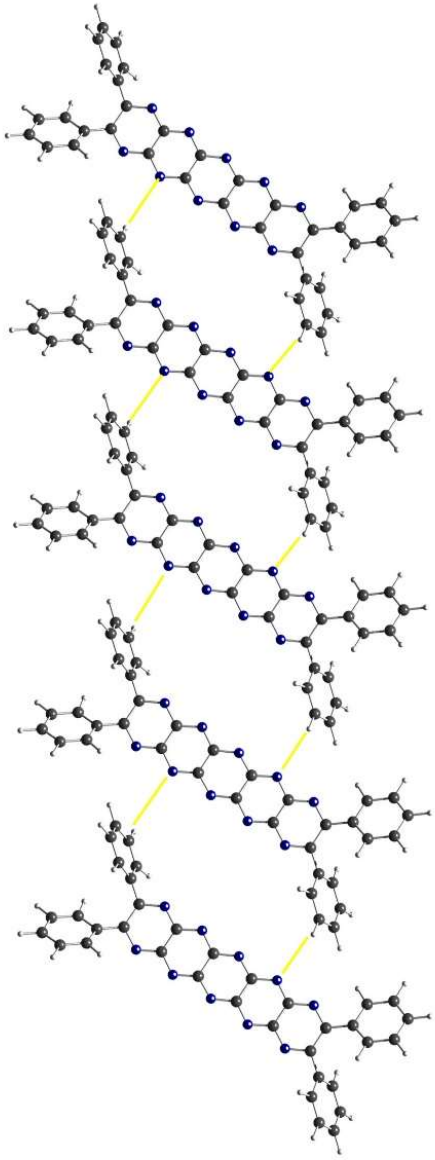

Figure S14. Packing structure within lines of **1** after self-assembly on Cu(111). The major structure directing factor is C-H…N hydrogen bonding, which is a also a major structure-director in crystals of pyrazinacenes (see Figure S11 overleaf).

12.0 C-H…N Hydrogen bonding in other pyrazinacenes

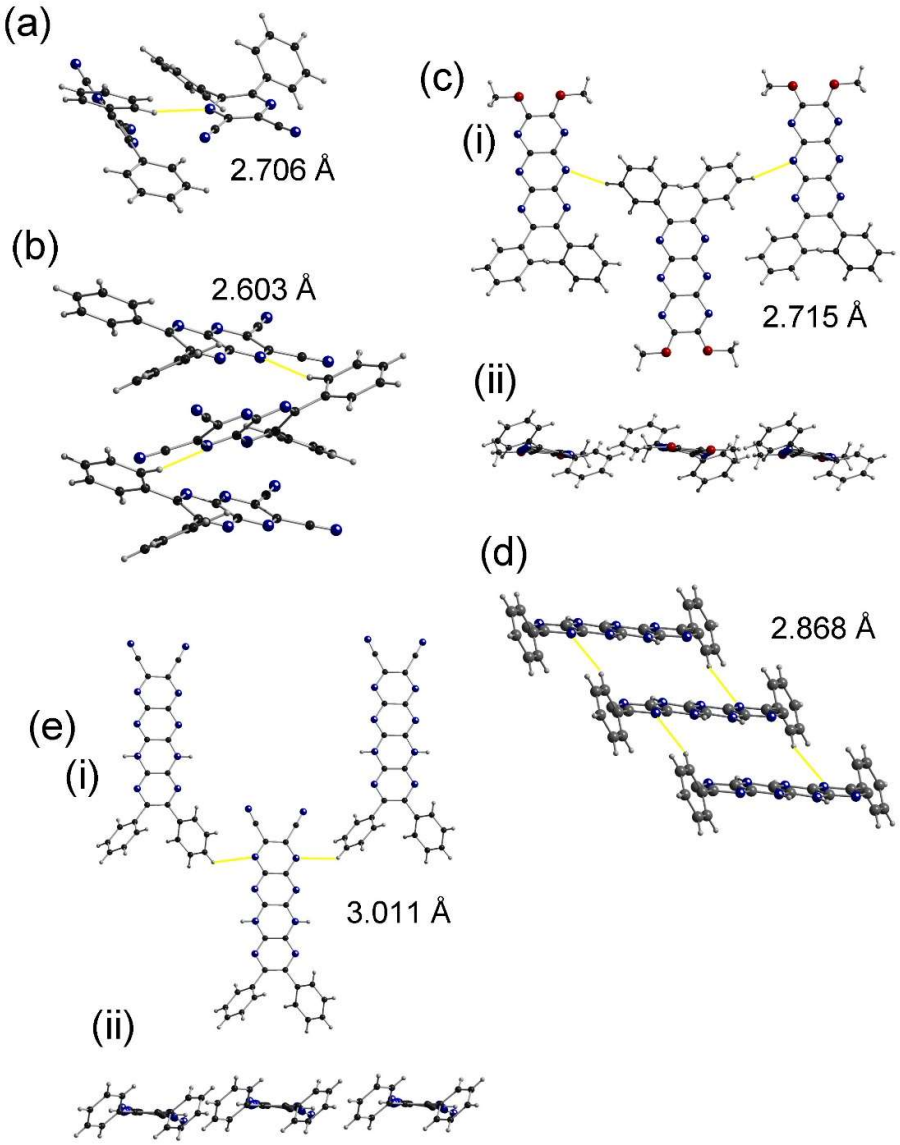

Figure S15. C-H…N H-bonding distances in X-ray crystal structures of other pyrazinacenes. Distances quoted are for close approach of proton to N atoms. (a) 2,3-Diphenylpyrazine-5,6-dicarbonitrile,[S8] (b) 2,3-diphenyl-1,4,5,8-tetraazanaphthalene-6,7-dicarbonitrile,[S8] (c) (i) 2,3-diphenyl-1,4,5,8,9,10-hexaaza anthracene-6,7-dicarbonitrile.[S8] (ii) Side view revealing edge-wise packing. (d) **2** (this work) and (e) (i) 2,3-diphenyl-5,12-dihydro-1,4,5,6,7,10,11,12-octaazatetracene.[S8] (ii) Side view revealing edge-wise packing.

13.0 In situ XPS data for compound 2

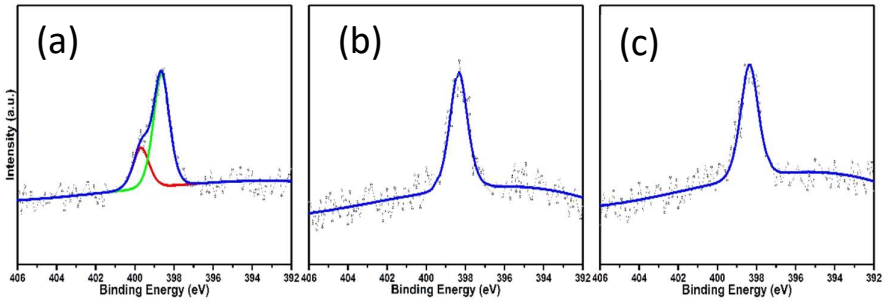

Figure S16. N1s XP spectra of **2** on Cu(111): (a) as-deposited as in Figure 2a,d of the main manuscript. (b) after annealing at 150°C as in Figure 2b,e of the main manuscript; (c) after annealing above 300°C as in Figure 2c,f. Disappearance of the N1s XPS peak at 399.4 eV is consistent with oxidation of the acene backbone.

14.0 Molecule profiles prior to and following annealing (300 °C)

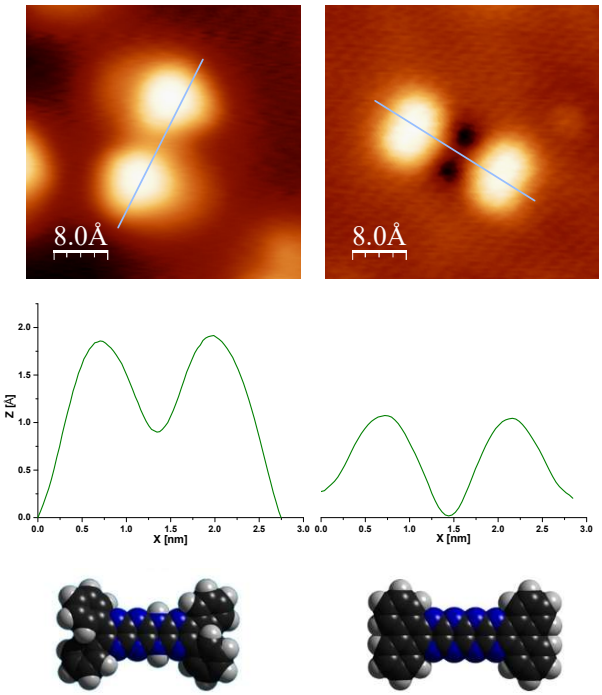

Figure S17. Molecule profile for **2**. (a) As-deposited molecule. (b) after annealing at 300 °C. (c), (d) Corresponding distance profiles for lines given in (a) and (b), respectively. Space-filling models of **2** and the species present after annealing. STM data information: a) 4nm x 4nm, 10pA, 1V. b) 4nm x 4nm, 10pA, 1V.

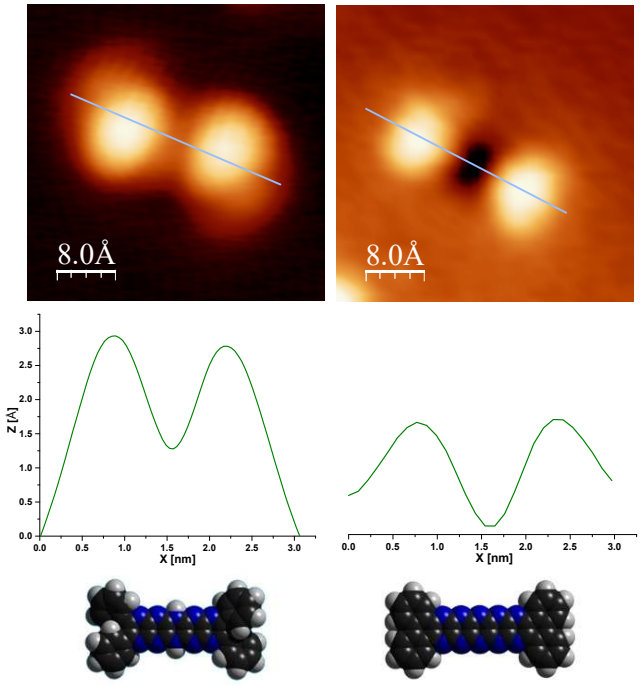

Figure S18. Molecule profile for **1**. (a) As-deposited molecule. (b) after annealing at 300 °C. (c), (d) Corresponding distance profiles for lines given in (a) and (b), respectively. Space-filling models of **1** and the species present after annealing. STM data information: a) 4nm x 4nm, 10pA, 1V. b) 4nm x 4nm, 10pA, 1V.

15.0 STM height profile data – self-assembled lines

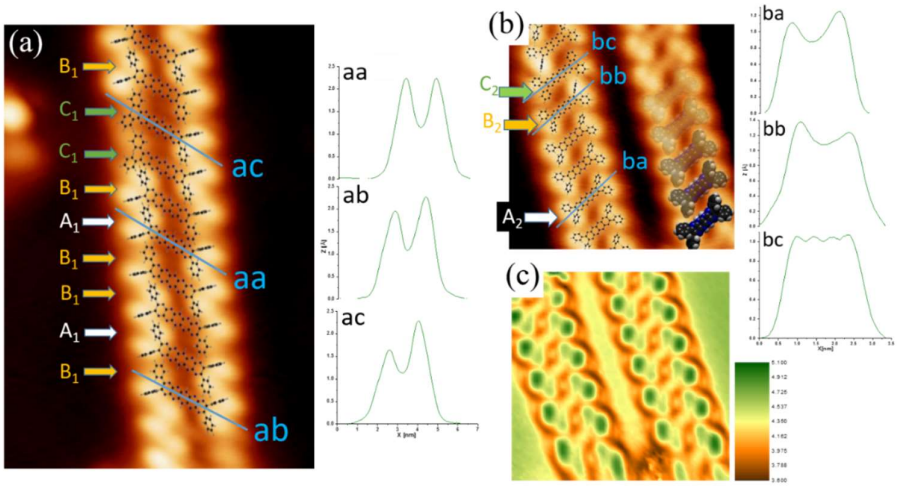

Figure S19. STM profile data for line structures of (a) **1** and (b) **2**. A_1, B_1 and C_1 denote three different conformations of **1** arranged within a linear array; the corresponding height profiles shown at right reveal depressed points due to phenyl group rotation (lower dihedral angles between phenyls and pyrazinacene). **2** similarly shows 3 conformations A_2, B_2 and C_2 with the height profiles also shown at the right of the STM image. STM images contain the respective packing models for **1** and **2**. (c) Work function map of **2**. The work function probes the local charge modification on the molecules by measuring current-distance I(z) plots at every point of the sample. From these it appears that the electronegative phenyls are imaged with higher electronegativity. Also the flexed rotation of the phenyl groups with respect to each other and the substrate is clearly shown. Due to the high electronegativity of the molecules, the surrounding borders of the chains are electron depleted and are identified by their lower electronegativity values.

Description of Figure S19. Variation in the height profiles of molecules contained within the line structures can be assigned to conformational variation of the phenyl substituents of the compounds, i.e. different dihedral angles between the planes of phenyl groups and the plane of the pyrazinacene backbone. For **2**, variation in the phenyl group conformation is relatively rare and appears as 'defects' in the line structures. The observed defects within the arrays correspond to different conformers being included in the arrays; the STM profile height is lower due to rotation of the phenyl groups of one molecule. Possibly in order to reduce stresses within the array, the molecules adjacent to this defect rotate their phenyl groups and are of brighter STM contrast and greater height, as shown in Figure S9b (Conformations B_2 and C_2). Therefore, there exist three different conformations of **2** (indicated in the STM image overlay of Figure S9b) although that closely resembling the crystal structure conformation (Conformation A_2) dominates. In contrast, phenyl group dihedral angle variation in **1** (Figure S9a) is significantly more common although there appears again to be three possible conformations. The contrast of STM images of the line structure of **1** suggests that conformations with larger dihedral angles between phenyl groups and pyrazinacene backbone are preferred. It is difficult to specify these angles but again rotation of the phenyl rings leads to their different heights in STM and allowed us to identify three distinct conformations, A_1 (similar conformation to energy minimized structure), B_1 (with a single phenyl group with a lower dihedral angle with the pyrazinacene) and C_1 (where two phenyl groups at the same end of the molecule have lower dihedral angles). It is likely that this difference in conformational preference between **1** and **2** (i.e., **1** commonly adopts a range of conformations while **2** largely adopts a conformation similar to its crystallographic form plus occasional defects) originates in interactions with the substrate lattice so that **2** is more easily accommodated in its preferred conformation while **1** is required to adapt (through dihedral angle variation) in order to form the line structures. Therefore, the line structures may be the lower energy state favored by both molecules over a dispersed state at the expense of phenyl group dihedral angle variation.

16.0 DFT Structures and Simulation of STM images

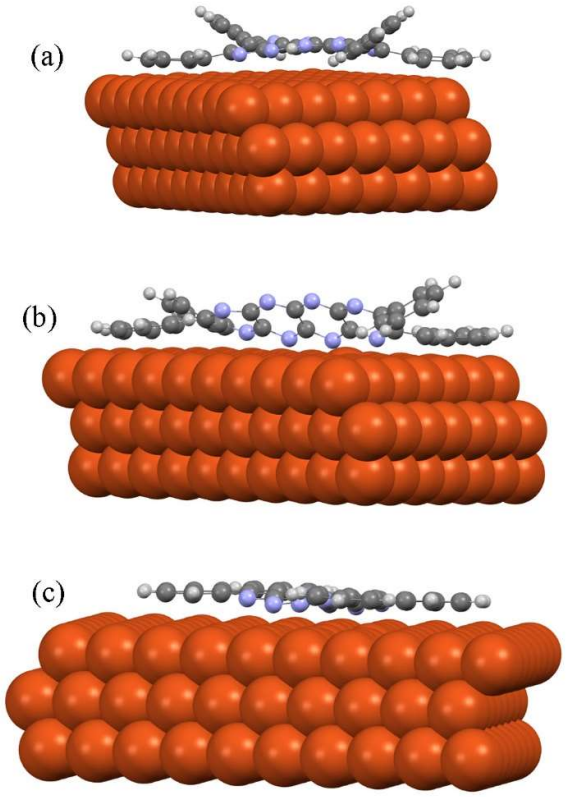

Figures S20. DFT Energy-minimized structures used to simulate STM images of **2** and products of its in situ oxidation on Cu(111). (a) **2**, (b) **2**-ox, and (c) cyclodehydrogenated **2**-ox.

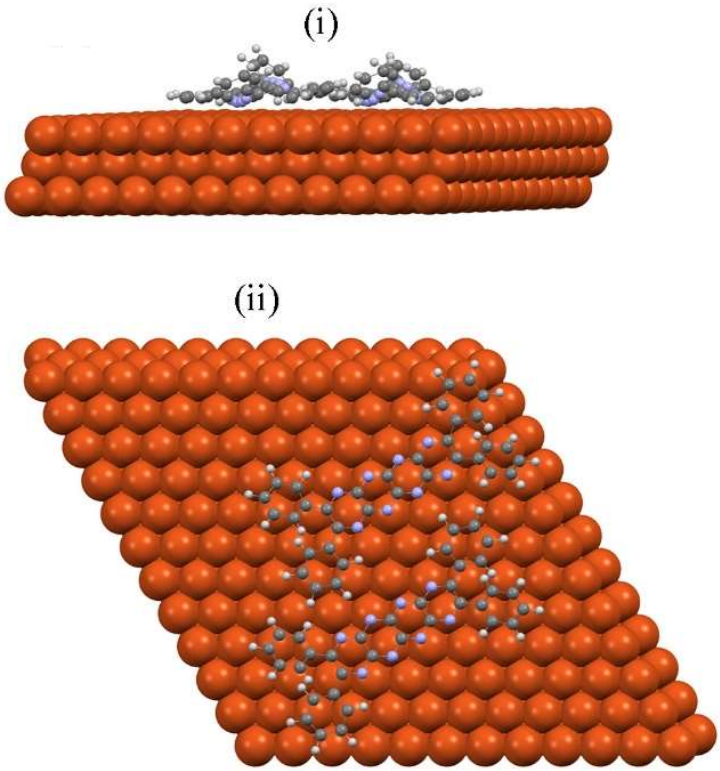

Figure S21. DFT Energy-minimized structures used to simulate STM images of **2** on Cu(111). (i) and (ii) are respectively side and plan elevations.

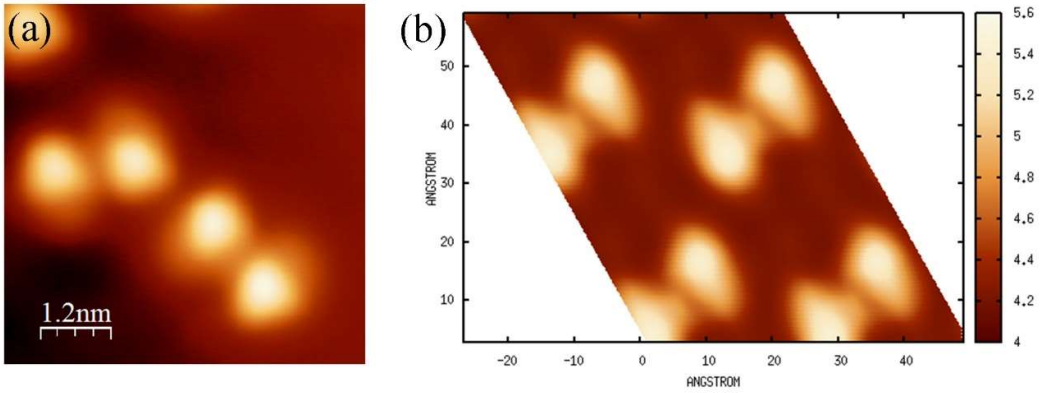

Figure S22. (a) Experimentally observed STM image of as-deposited **2** and (b) simulated STM image of **2** on Cu(111).

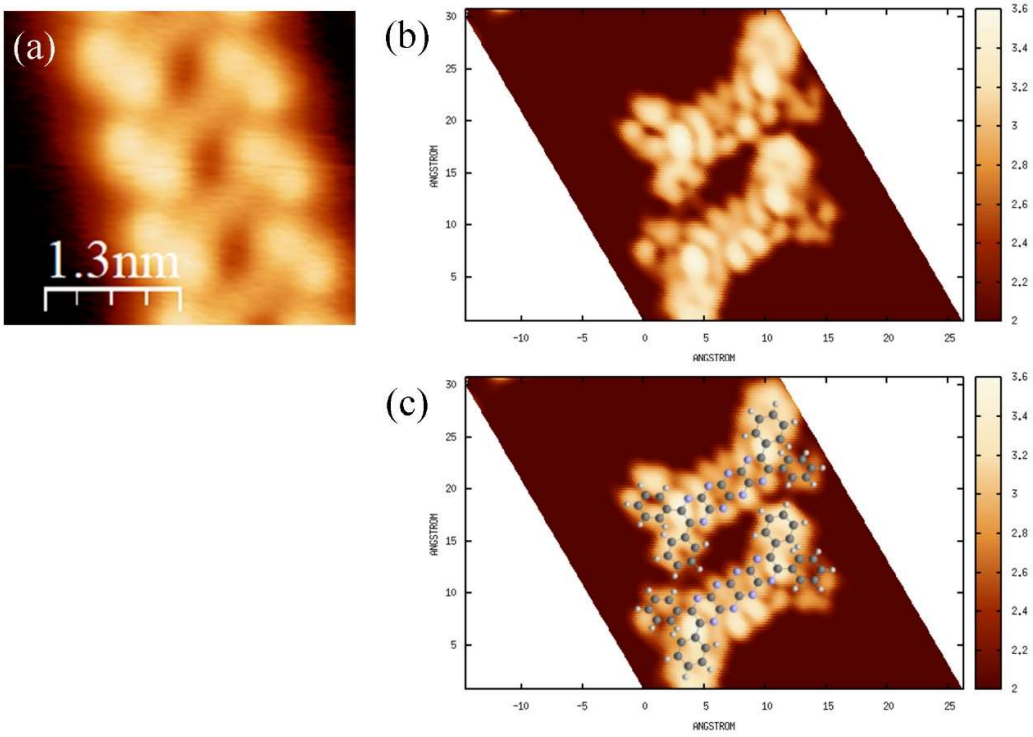

Figure S23. (a) Experimentally observed STM image of **2**-ox self-assembled line structures obtained by in situ dehydrogenation on Cu(111). (b) Simulated STM image of **2**-ox on Cu(111). (c) Simulated STM image of **2**-ox on Cu(111) with molecular structure overlaid indicating that CH…N hydrogen bonding is the most important intermolecular interaction.

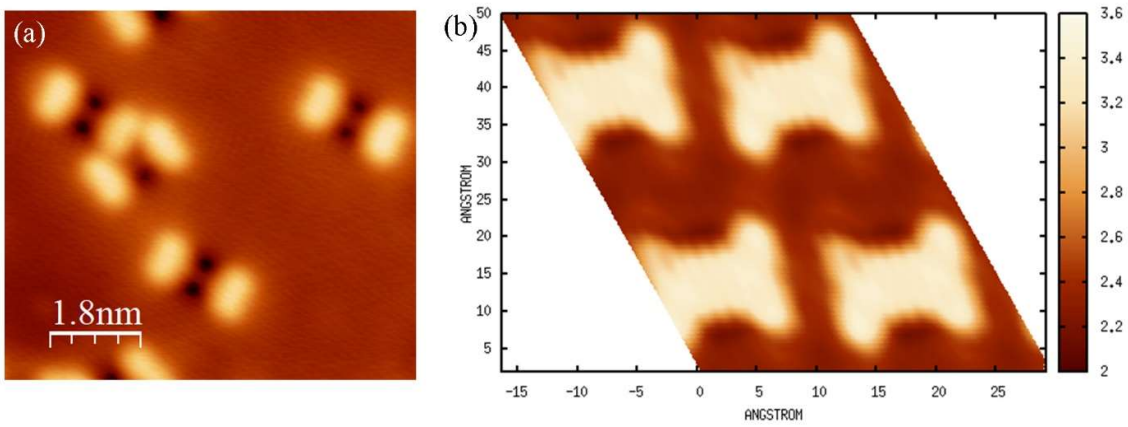

Figure S24. (a) Experimentally observed STM image of in situ cyclodehydrogenated **2**-ox. (b) Simulated STM image of in situ cyclodehydrogenated **2**-ox on Cu(111).

17.0 Photoredox Activity

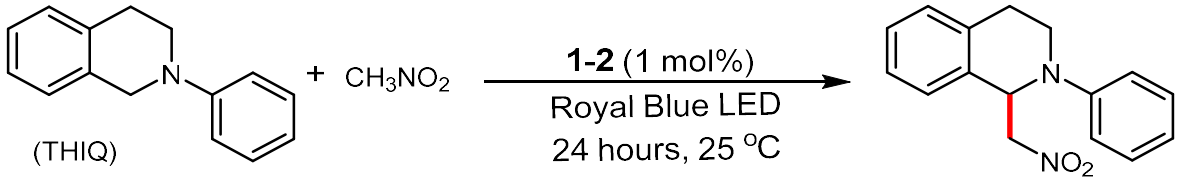

Scheme S1. Benchmark CDC reaction.

Table S1. Yields of reaction shown in Scheme S1 catalyzed by **1** or **2**.

Comp.	Conversion [%][a]	Isolated yield [%]
none	0	0
1	67	63
2	72	70

[a)] Calculated from the NMR spectrum of the crude reaction mixture

18.0 NMR and mass spectra

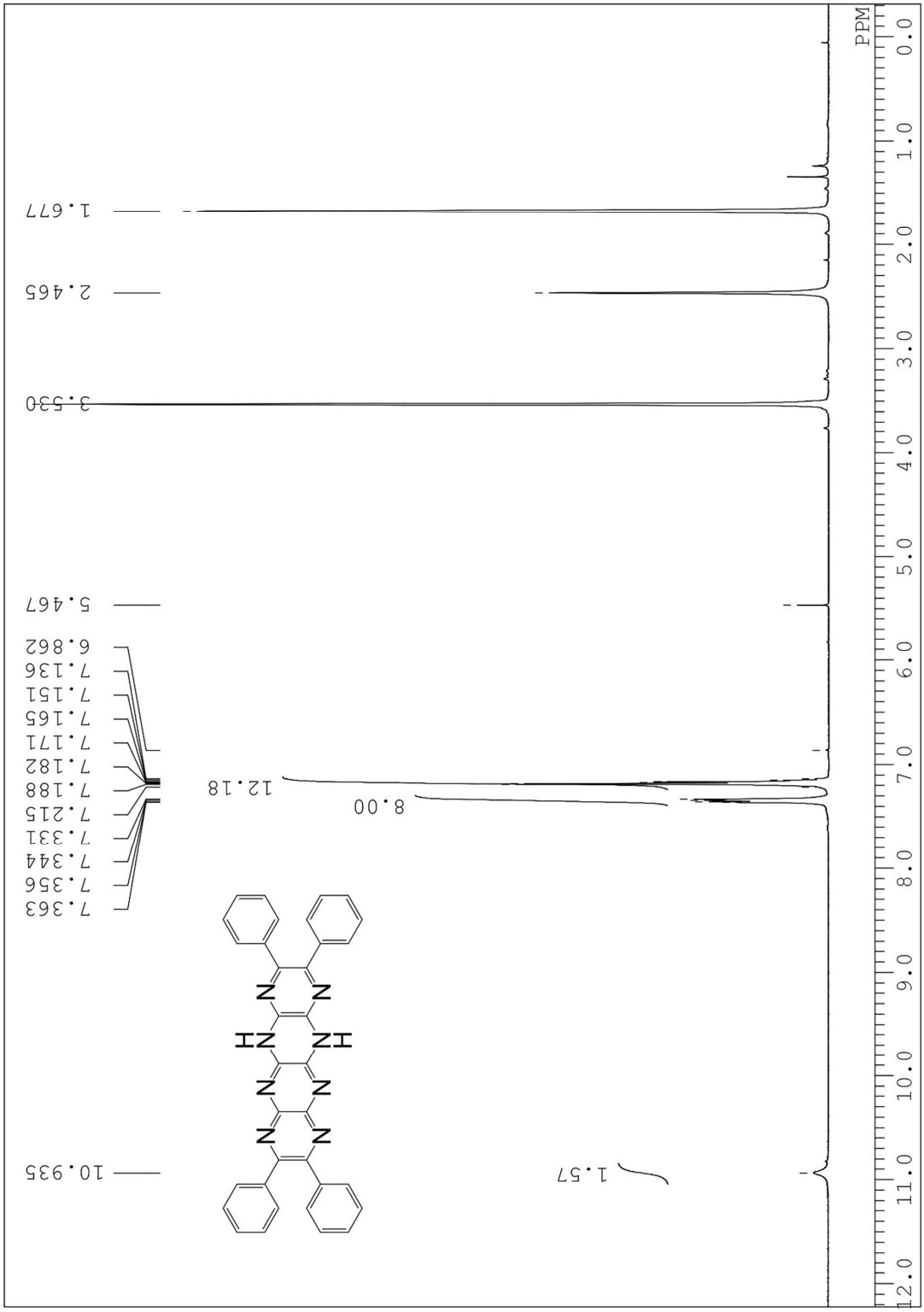

Figure S25. ^{1}H-NMR spectrum of **2** in tetrahydrofuran-d_8.

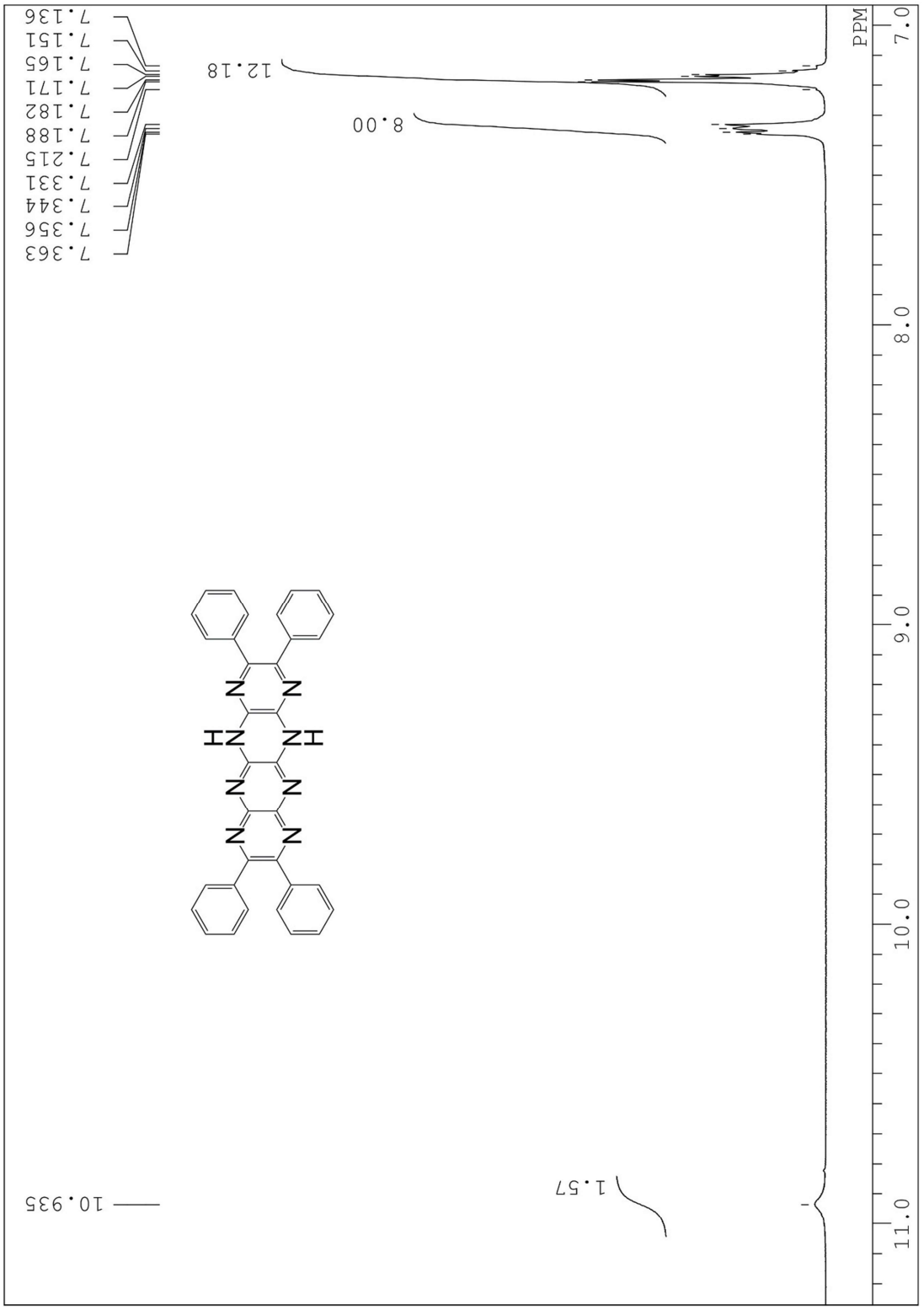

Figure S26. Low field region of ^{1}H-NMR spectrum of **2** in tetrahydrofuran-d_8.

19.0 References

[S1] M. Valiev, E. J. Bylaska, N. Govind, K. Kowalski, T. P. Straatsma, H. J. J. van Dam, E. Wang, J. Nieplocha, E. Apra, E. L. Windus, W. A. de Jong *Comput. Phys. Commun*. **2010**, *181*, 1477 – 1489.

[S2] *Gaussian 09, Rev. B.01, M. J. Frisch, G. W. Trucks, H. B. Schlegel, G. E. Scuseria, M. A. Robb, J. R. Cheeseman, V. G. Zakrzewski, J. A. Montgomery, R. E. Stratmann, J. C. Burant, S. Dapprich, J. M. Millam, A. D. Daniels, K. N. Kudin, M. C. Strain, O. Farkas, J. Tomasi, V. Barone, M. Cossi, R. Cammi, B. Mennucci, C. Pomelli, C. Adamo, S. Clifford, J. Ochterski, G. A. Petersson, P. Y. Ayala, Q. Cui, K. Morokuma, D. K. Malick, A. D. Rabuck, K. Raghavachari, J. B. Foresman, J. Cioslowski, J. V. Ortiz, B. B. Stefanov, G. Liu, A. Liashenko, P. Piskorz, I. Komaromi, R. Gomperts, R. L. Martin, D. J. Fox, T. Keith, M. A. Al-Laham, C. Y.Peng, A. Nanayakkara, C. Gonzalez, M. Challacombe, P. M. W. Gill, B. G. Johnson, W. Chen, M. W. Wong, J. L. Andres, M. Head-Gordon, E. S. Replogle, J. A. Pople, Gaussian Inc., Pittsburgh PA, **2009**.*

[S3] N. Sato, H. *J.* Mizuno, *Chem. Res., Synop.* **1997**, 250 – 251.

[S4] *CrystalClear,* Rigaku Corporation, Tokyo, Japan (2005).

[S5] G. M. Sheldrick, *Acta Cryst.* **2015**, *A71*, 3 – 8.

[S6] G. M. Sheldrick, *Acta Cryst.* **2008**, A64, 112 – 122.

[S7] L. J. Farrugia, *J. Appl. Cryst.* **1999***, 32*, 837 – 838.

[S8] P. Ordejón, E. Artacho, J. M. Soler, *Phys. Rev. B* **1996**, *53*, R10441 – R10444.

[S9] J. M. Soler, E. Artacho, J. D. Gale, A. García, J. Junquera, P. Ordejón, D. Sánchez-Portal, *J. Phys.:Condens. Matter*. **2002**, *14*, 2745 – 2779.

[S10] See also the Siesta distribution site, https://launchpad.net/siesta

[S11] N. Troullier, J. L. Martins, *Phys. Rev. B* **1992**, *46*, 1754 – 1765.

[S12] K. Berland, P. Hyldgaard, *Phys. Rev. B* **2014**, *89*, 035412.

[S13] J. Tersoff, D. R. Hamann, *Phys. Rev. B* **1985**, *31*, 805 – 813.

[S14] G. J. Richards, J. P. Hill, N. K. Subbaiyan, F. D'Souza, M. R. J. Elsegood, S. J. Teat, T. Mori, K. Ariga, *J. Org. Chem.*, **2009**, *74*, 8914 – 8923.

Chapter [[2]] and Supplementary Information

[[2]] - Frustrated H-bonding of planar molecules on a weakly interacting semi-metallic Bi surface

S. Fatemeh Mousavi, Aisha Ahsan, Thomas Nijs, Milos Baljozovic, Aneliia Wäckerlin, Olha Popova, Sylwia Nowakowska, Christian Wäckerlin, Jonas Björk, Lutz Gade and Thomas A. Jung

Contribution of S. F. Mousavi: carried out experimental investigations (STM & XPS), analyzed and interpreted the data, wrote the manuscript

COMMUNICATION

Received 00th January 20xx,
Accepted 00th January 20xx

DOI: 10.1039/x0xx00000x

www.rsc.org/

Frustrated H-bonding of planar molecules on a weakly interacting semi-metallic Bi surface

S. Fatemeh Mousavi,[*a] Aisha Ahsan,[a] Thomas Nijs,[a] Benjamin Günther,[b] Milos Baljozovic,[c] Aneliia Wäckerlin,[a,d], Olha Popova,[a] Sylwia Nowakowska,[a] Christian Wäckerlin,[*d] Jonas Björk,[*e] Thomas A. Jung[*c] and Lutz H. Gade[*b]

DPDI molecules exclusively act as hydrogen bond donors in planar 2D arrangements, making them potential building blocks for "frustrated" H-bonded aggregates on weakly interacting substrates such as Bi-Cu(100). A combination of STM experiments and DFT modeling has shown that slight out of plane rotation of the molecules enables aggregation via hydrogen bond "over-coordination", forming inter alia a porous network with chiral three-connected nodes.

Among the interactions governing molecular and macromolecular structure in three dimensional as well as in two-dimensional (2D) assembly at interfaces, H-bonding is of central importance.[1–5] The resulting supramolecular assemblies are directed via the location and orientation of the functional groups interacting in the form of hydrogen bond donor-acceptor couples. The absence or underrepresentation of complementary H-bonding acceptor units may result in bifurcated or "over-coordinated" hydrogen bonds that direct the aggregation.[6–13] In this work, we demonstrate that upon restricting the dimensionality of the aggregates on surfaces,[14–28] a remarkable situation may arise for molecules which can exclusively act as 2D H-bond donors, while possessing atoms with orthogonal H-bond accepting electron density (in molecular orbitals with π-symmetry). We show that the resulting frustration of hydrogen bonding in 2D may be overcome by slight tilting of the individual molecules, which leads to the collective stabilization of ordered aggregates.

The functionalized polycyclic aromatic compound 4,9-diaminoperylene quinone-3,10-diimine (DPDI) (Figure 1)[29] has been found to undergo a variety of transformations on coinage metal surfaces, in particular on Cu, and has given rise to a variety of highly ordered surface structures based on the partial thermal dehydrogenation and coordination of the resulting endo- or exoligands to surface adatoms.[30,31] On the other hand, the parent compound DPDI has not generated ordered structures upon deposition onto different crystal faces of Cu substrates. This is due to the absence of complementary interacting functional groups which could direct an ordered assembly of the molecules in a planar arrangement.

DPDI can exclusively act as a hydrogen bond donor in a 2D array whereas *appropriately orientated* lone pairs, which could act as hydrogen bond acceptors, are absent. This applies to both tautomers of DPDI, represented in Figure 1, l-DPDI with the arrangement of imino and amino groups colinear to the principal molecular axis and x-DPDI with an over-cross arrangement of the functional groups. While not distinguishable in solution due to rapid tautomerization, a DFT study for both molecules in the gas phase has shown that the latter is destabilized by ca 1.5 kcal·mol^{-1} (65 meV, see ESI 6.8). These properties render them ideal objects of study for possible 2D aggregation patterns in such a "frustrated" situation as would occur on smooth surfaces, such as the faces of single crystal substrates.

Given the expected weak intermolecular interactions, the considerable interaction strength of planar polyaromatic molecules with metallic substrates provides an obstacle which may be dampened by decoupling layers from semi-metallic[32] and non-metallic,[33–36] materials. For the current study we have chosen Bi reconstructed Cu(100) at higher than 0.5 ML Bi surface coverage as it has been reported to form a p(10x10) surface reconstruction.[37–39] This reconstruction is characterized by a regular pattern of pockets and dislocation arrays along the <100> directions (Figure 2a).

[a] *Department of Physics, University of Basel, Klingelbergstrasse 82, 4056 Basel, Switzerland.*
[b] *Anorganisch-Chemisches Institut, Universität Heidelberg, Im Neuenheimer Feld 270, 69120 Heidelberg, Germany.*
[c] *Laboratory for Micro- and Nanotechnology, Paul Scherrer Institute, 5232 Villigen PSI, Switzerland.*
[d] *Nanoscale Materials Science and Laboratory for Thin Films and Photovoltaics, Empa, Swiss Federal Laboratories for Materials Science and Technology, 8600 Dübendorf, Switzerland.*
[e] *Department of Physics, Chemistry and Biology, IFM, Linköping University, 581 83 Linköping, Sweden.*
† Electronic Supporting Information: Addn STM data for the DPDI surface arrays, XPS data, results of the DFT modeling of DPDI adsorption on Bi/Cu(100), comparison of alternative network structures.See DOI: 10.1039/x0xx00000x

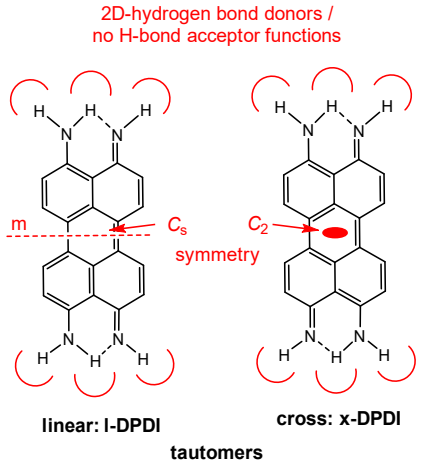

Figure 1. The two tautomeric forms l-DPDI and x-DPDI, possessing C_s and C_2 symmetry, respectively, in 2D. Both forms lack H-bond acceptor capability in 2D.

Two ordered aggregation patterns were identified by Scanning Tunneling Microscopy (STM), a new, weakly aggregated porous network containing windmill shaped nodes (generating distorted hexagons) and a compact assembly with a zigzag structure (Figure 2b,c) which is predominant at high coverages (Figure 3a). Interestingly, the two monolayer patterns co-exist even at low coverages on the same terraces of the substrate. This indicates that their formation energy (per molecule) is by coincidence about similar in spite of their distinctly different packing density and structure.[40]

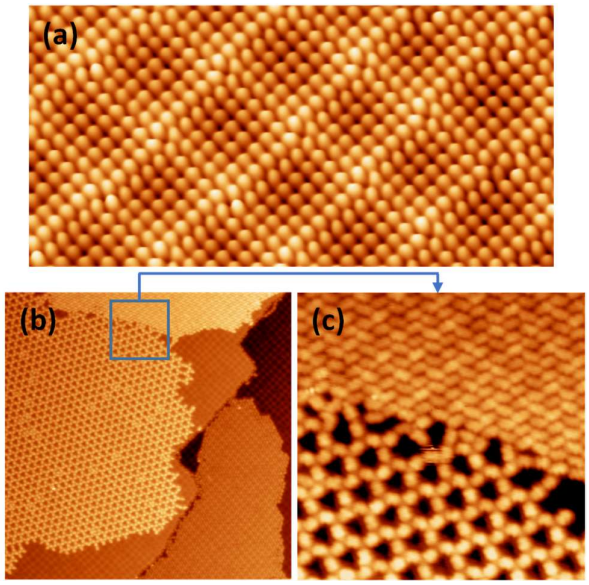

Figure 2: Atomic and molecular resolution micrographs of Bi re-constructed Cu(100) and on-surface supramolecular assemblies of DPDI, an amino-functionalized perylene derivative. a) atomic resolution Scanning Tunneling Microscopy (STM) image of p(10x10) Bi reconstructed Cu(100). b) STM micrograph of DPDI on Bi reconstructed Cu(100). Trigonal porous network of distorted hexagons and zigzag assembly created by deposition of DPDI on Bi/Cu(100) c) Zoom image taken in the area of b) showing the border between zigzag assembly and hexagonal networks a) 10 nm x 5 nm, -5 mV, 400pA, b) 90 nm x 90 nm, 1 V, 10 pA, c) 20 nm x 20 nm, 1 V, 10 pA

X-ray Photoelectron Spectroscopy (XPS) was employed to identify the chemical state of the molecular building block involved in assemblies of DPDI on Bi/Cu(100). Only the intact DPDI, characterized by the two peaks identified as amine (399.4 eV) and imine (398 eV) nitrogen, was observed The relative intensity of the amine and imine peaks was found to be independent of the relative surface coverage of the distorted hexagonal network and the higher density zigzag arrangement observed at increased DPDI coverage (Figure 3b).

Towards understanding the binding motif, the aggregation patterns were analyzed by high resolution STM at 5K. For the porous network the principle molecular axes of the three DPDI connected at the nodes are not pointing to its centre but form a C_3 symmetric "2D-chiral" motif (Figure 4a), representing alternatively right- (R) and left-handed (L) helicity. We note that such 2D chiral three-connected nodes have been observed previously in surface arrays of organic molecules.[41,42]

The x-DPDI tautomer with its C_2-symmetry in 2D would have generated a network structure with homochiral nodes (Figure S10). Since the DPDI molecules of these ordered aggregates cannot aggregate via H-bonding in a planar arrangement the question arose how these "frustrated" systems arrange to form both ordered arrays, the porous network (Figure 4a) and the more densely packed ‘zigzag’ pattern (Figure 4b).

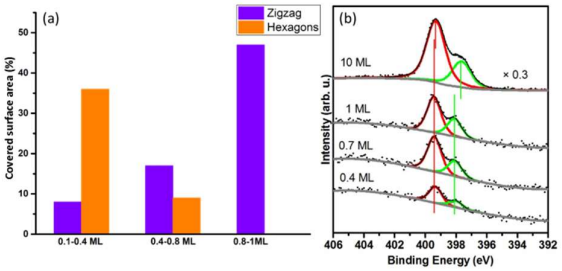

Figure 3. Identification of the chemical form of DPDI involved in the two co-existing assemblies. a) Statistical bar chart showing the increased fraction of the zigzag assembly with increased DPDI coverage. b) The surface chemical analysis by N1s XPS reveals two peaks identified as amine (399.4 eV) and imine (398 eV) nitrogen consistent with earlier reports. A constant amine/imine ratio is observed with increasing coverage from 0.4 ML to the multilayer.

Each pore of the network is thus surrounded by three L and three R nodes, generating a network with a 1:1 ratio of both enantiomeric types of nodes to give an overall achiral "meso"-structure. We note that this heterochiral array of adjacent nodes is to be seen as a direct consequence of the individual molecule adopting the l-DPDI form and thus possessing molecular C_s-symmetry (Figure 1). The x-DPDI tautomer with its C_2-symmetry in 2D would have generated a network structure with homochiral nodes (Figure S10). Since the DPDI molecules of these ordered aggregates cannot aggregate via H-bonding in a planar arrangement the question arose how these "frustrated" systems arrange to form both ordered arrays, the porous network (Figure 4a) and the more densely packed ‘zigzag’ pattern (Figure 4b).

To investigate the observed structures further in depth, we carried out DFT calculations of how the DPDI molecule adsorbs on the Bi/Cu(100) surface and how molecules may form stable intermolecular bonding motifs (see ESI). DPDI was found to adsorb in registry with the Bi top (ESI)layer with a comparably low adsorption energy of 1.58 eV and an adsorption height of 3.46 Å, characteristic of physisorption (Figure S4). Optimization of different freestanding network structures of DPDI revealed that the linear l-DPDI isomer forms the most stable network (Figure S6), with network dimensions and alternating chirality of network nodes consistent with the experimental data (Figure 4c). Importantly, the steric repulsion between one of the H atoms of the DPDI molecule and one of the H atoms of the amine group leads to the out of plane rotation of the DPDI molecules for each node generating 3D-chiral propeller like nodes (see Figure 4c, inset at the bottom).

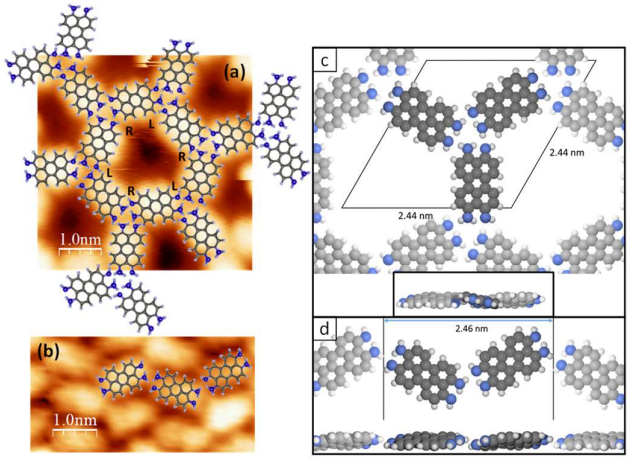

Figure 4. STM images and structural models of coexisting hydrogen bonded structures of DPDI on Bi/Cu(100). a) The quasi-hexagonal porous network with a superimposed ball-and-stick model. b) Zigzag assembly with a 2D superimposed ball-and-stick model. STM images: a) 5 nm x 5 nm, 500 mV, 30 pA b) 5 nm x 5 nm, 1 V, 10 pA. DFT studies. c) DFT model of the hexagonal network (formation energy -345 meV/molecule). DPDI remains close to planar in spite of its distinct out-of-plane orientation as it is visible from the side view below. Neighboring nodes exhibit opposite chirality. d) DFT model of the zigzag assembly (formation energy -150 meV/molecule).

For comparison this freestanding network with the heterochiral nodes, has been modelled in the gas phase and in a corresponding hypothetical network composed of the x-DPDI tautomer, in which the nodes are homochiral: The formation energy of the observed network is found to be 85 meV/molecule more stable than of the homochiral alternative (see ESI 6.6). Approximately two thirds of this energy difference correspond to the greater stability of l-DPDI compared to x-DPDI (vide supra). The remaining energy difference is due to the fact that in the homochiral network the molecule is slightly twisted, while in the heterochiral network the molecule is tilted but remains planar.

As the out of plane tilt of the DPDI molecules is required for linking the l-DPDI molecules in this H-bonding model, it is most pronounced in model calculations of the molecules as free standing layers, but clearly survives if the model calculation is performed in presence of the Bi/Cu(100) substrate. The weak interaction with the substrate is a prerequisite to the out-of-plane rotation of the DPDI molecules in this binding motif and thus to the formation of the H-bonded network.

It is quite remarkable that a planar adsorbate is driven in an out of plane orientation by intermolecular H-bonding as this is not a strong binding motif. The rather weak interaction of DPDI assemblies with the alloyed Bi/Cu(100) layers, and the resulting large adsorption heights of approx. 3.5 Å and the frustrated H-bonding is also evidenced by the facile disruption of this layer in STM repositioning experiments (Figure S3) and also by its desorption from the substrate at relatively low (<~100 °C) temperatures.

For the second observed self-assembled structure with its characteristic zigzag appearance (Figure 4d) a characteristic out-of-plane tilt of the l-DPDI molecules in the zigzag structure has also resulted from the DFT calculations (Figure 4d, bottom). From this model it becomes clear that the number of intermolecular H-bonds per molecule for the zigzag structure is only half (i.e. 2 compared to 4 bonds per molecule) that of the porous network. The predominant appearance of the hexagonal structure at lower than unity coverage (Figure 3a) of DPDI on Bi/Cu(100) can therefore be attributed to higher degree of intermolecular H-bonding. The porous network structure disappears at higher coverage to the benefit of the more compact chain structure in which the lower per molecule stabilization (by 195 meV/molecule) is compensated by stabilization through inter-chain interactions. Note that the molecular layer is driven into increasingly dense packing by the favoured Bi-DPDI interaction compared to the DPDI-DPDI interaction as typically observed, also on metal substrates.

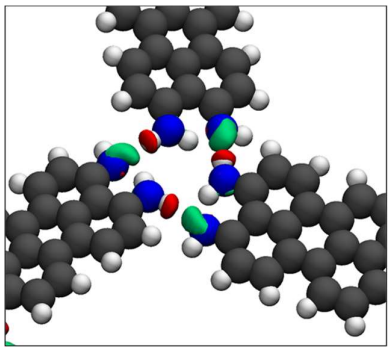

Figure 5. Electron density map denoting the redistribution of electronic charge which is a prerequisite for H-bonding. Green: Electron accumulation at the imine (donor), Red: Electron depletion at the amine (acceptor), Absolute value of contours: 0.01 e/Å^3.

A closer inspection of the hydrogen bonding which ties the molecules together at the chiral nodes has revealed that this represents a case for hydrogen bond "over-coordination" (Figure 5). An electron density map of three molecules in contact with each other in the relevant region illustrates the redistribution of electronic charge which is a prerequisite for the H-bonding. Notably, we find the accumulation of negative charge on the imine nitrogen atoms along with the polarization of one of the amine N-H bonds. A similar situation applies to the aggregation in the more densely packed "zigzag" structure(see ESI).In conclusion, a combination of STM

experiments and DFT modeling has shown that DPDI molecules, which form highly regular aggregates, can exclusively act as hydrogen bond donors in planar 2D arrays. Such "frustrated" H-bonding can be overcome through a slight out of plane rotation of the molecules which enables aggregation via hydrogen bond "over-coordination". The prerequisite for this structural flexibility to evade the slightly two-dimensional regime, is the weak adsorption energy with the substrate, in this case the Bi/Cu(100) system. The result has been either a porous network with chiral three-connected nodes or a more closely packed zigzag form of aggregation. This type of assembly mechanism may turn out to be fairly common for weakly adsorbed molecular layers.

Acknowledgements

Mac Iwasaki, Mariah O'Doherty, Robert Skonieczny, Mina Moradi, Jan Nowakowski, R. Schelldorfer, M. Martina and M. Senn are gratefully acknowledged for helpful discussions and support. We acknowledge funding by the Paul Scherrer Institute, the Physics Department of the University of Basel and the Swiss Nanoscience Institute, the Swiss National Science Foundation (Grants # 200020_162512, 206021_144991, 206021_121461), the Swiss Commission for Technology and Innovation (CTI, 16465.1 PFNM-NM), the Swiss Government Excellence Scholarship Program for Foreign Scholars as well as the Deutsche Forschungsgemeinschaft (SFB 1249 TP A2). J.B. acknowledges computational resources at the National Supercomputer Centre, Sweden, allocated by SNIC.

Conflicts of interest

There are no conflicts to declare.

Notes and references

1 J. M. Berg, J. L. Tymoczko, L. Stryer and L. Stryer, *Biochemistry*, W.H. Freeman, New York, 5th ed., 2002.
2 S. De Feyter and F. C. De Schryver, *Chem. Soc. Rev.*, 2003, **32**, 139–150.
3 T. Kudernac, S. Lei, J. A. A. W. Elemans and S. De Feyter, *Chem Soc Rev*, 2009, **38**, 402–421.
4 A. G. Slater, L. M. A. Perdigão, P. H. Beton and N. R. Champness, *Acc. Chem. Res.*, 2014, **47**, 3417–3427.
5 O. Ivasenko and D. F. Perepichka, *Chem Soc Rev*, 2011, **40**, 191–206.
6 M. Baron, S. Giorgi-Renault, J. Renault, P. Mailliet, D. Carré and J. Etienne, *Can. J. Chem.*, 1984, **62**, 526–530.
7 D. Laage, *Science*, 2006, **311**, 832–835.
8 O. Markovitch and N. Agmon, *Mol. Phys.*, 2008, **106**, 485–495.
9 C. B. Aakeröy and K. R. Seddon, *Chem Soc Rev*, 1993, **22**, 397–407.
10 I. Rozas, I. Alkorta and J. Elguero, *J. Phys. Chem. A*, 1998, **102**, 9925–9932.
11 T. Steiner, *Angew. Chem. Int. Ed.*, 2002, **41**, 48–76.
12 M. Head-Gordon and T. Head-Gordon, *Chem Phys Lett*, 1994, **220**, 122–128.
13 P. A. Giguère, *J. Chem. Phys.*, 1987, **87**, 4835–4839.
14 L. Dong, Z. Gao and N. Lin, *Prog. Surf. Sci.*, 2016, **91**, 101–135.
15 S. Mohnani and D. Bonifazi, *Coord. Chem. Rev.*, 2010, **254**, 2342–2362.
16 M. Koepf, F. Chérioux, J. A. Wytko and J. Weiss, *Coord. Chem. Rev.*, 2012, **256**, 2872–2892.
17 C. Xie, Q.-M. Wu, R.-N. Li, G.-C. Gu, X. Zhang, N. Li, R. Berndt, J. Kröger, Z.-Y. Shen, S.-M. Hou and Y.-F. Wang, *Chin. Chem. Lett.*, 2016, **27**, 807–812.
18 Y.-W. Yang, Y.-L. Sun and N. Song, *Acc. Chem. Res.*, 2014, **47**, 1950–1960.
19 G. de Ruiter, M. Lahav and M. E. van der Boom, *Acc. Chem. Res.*, 2014, **47**, 3407–3416.
20 V. Balzani, A. Credi and M. Venturi, *ChemPhysChem*, 2008, **9**, 202–220.
21 Z. Huang, Y. Zhang, Y. He, H. Song, C. Yin and K. Wu, *Chem. Soc. Rev.*, 2017, **46**, 1955–1976.
22 J. A. A. W. Elemans, S. Lei and S. De Feyter, *Angew. Chem. Int. Ed.*, 2009, **48**, 7298–7332.
23 J. M. Gottfried, *Surf. Sci. Rep.*, 2015, **70**, 259–379.
24 J. V. Barth, *Annu. Rev. Phys. Chem.*, 2007, **58**, 375–407.
25 L. Bartels, *Nat. Chem.*, 2010, **2**, 87–95.
26 S. De Feyter and F. C. De Schryver, *J. Phys. Chem. B*, 2005, **109**, 4290–4302.
27 M. Matena, A. Llanes-Pallas, M. Enache, T. Jung, J. Wouters, B. Champagne, M. Stöhr and D. Bonifazi, *Chem. Commun.*, 2009, 3525.
28 A. Llanes-Pallas, M. Matena, T. Jung, M. Prato, M. Stöhr and D. Bonifazi, *Angew. Chem. Int. Ed.*, 2008, **47**, 7726–7730.
29 L. H. Gade, C. H. Galka, K. W. Hellmann, R. M. Williams, L. De Cola, I. J. Scowen and M. McPartlin, *Chem. - Eur. J.*, 2002, **8**, 3732.
30 A. Shchyrba, C. Wäckerlin, J. Nowakowski, S. Nowakowska, J. Björk, S. Fatayer, J. Girovsky, T. Nijs, S. C. Martens, A. Kleibert, M. Stöhr, N. Ballav, T. A. Jung and L. H. Gade, *J. Am. Chem. Soc.*, 2014, **136**, 9355–9363.
31 M. Matena, J. Björk, M. Wahl, T.-L. Lee, J. Zegenhagen, L. H. Gade, T. A. Jung, M. Persson and M. Stöhr, *Phys. Rev. B*, , DOI:10.1103/PhysRevB.90.125408.
32 A. Wäckerlin, S. Fatayer, T. Nijs, S. Nowakowska, S. F. Mousavi, O. Popova, A. Ahsan, T. A. Jung and C. Wäckerlin, *Nano Lett.*, 2017, **17**, 1956–1962.
33 S. Joshi, F. Bischoff, R. Koitz, D. Ecija, K. Seufert, A. P. Seitsonen, J. Hutter, K. Diller, J. I. Urgel, H. Sachdev, J. V. Barth and W. Auwärter, *ACS Nano*, 2014, **8**, 430–442.
34 C. Morchutt, J. Björk, S. Krotzky, R. Gutzler and K. Kern, *Chem. Commun.*, 2015, **51**, 2440–2443.
35 T. Dienel, J. Gómez-Díaz, A. P. Seitsonen, R. Widmer, M. Iannuzzi, K. Radican, H. Sachdev, K. Müllen, J. Hutter and O. Gröning, *ACS Nano*, 2014, **8**, 6571–6579.
36 L. Ramoino, M. von Arx, S. Schintke, A. Baratoff, H.-J. Güntherodt and T. A. Jung, *Chem. Phys. Lett.*, 2006, **417**, 22–27.
37 H. . Meyerheim, M. De Santis, W. Moritz and I. . Robinson, *Surf. Sci.*, 1998, **418**, 295–302.
38 P. Wynblatt, D. Chatain and A. Ranguis, *Surf. Sci.*, 2007, **601**, 1623–1629.
39 P. Gargiani, M. G. Izzo, F. Bussolotti, M. G. Betti, S. Achilli and M. I. Trioni, *J. Chem. Phys.*, 2010, **132**, 174706.
40 T. Nijs, F. J. Malzner, S. Fatayer, A. Wäckerlin, S. Nowakowska, E. C. Constable, C. E. Housecroft and T. A. Jung, *Chem. Commun.*, 2015, **51**, 12297–12300.
41 M. Pivetta, G. E. Pacchioni, E. Fernandes and H. Brune, *J. Chem. Phys.*, 2015, **142**, 101928.
42 S. Dutta and A. J. Gellman, *Chem. Soc. Rev.*, 2017, **46**, 7787–7839.

Supporting Information:

Frustrated H-bonding of planar molecules on a weakly interacting semi-metallic Bi surface

Table of contents:

1. Methods section

All sample preparations and investigation were performed under ultrahigh vacuum (UHV) conditions with a base pressure of $\sim 10^{-10}$ mbar. The crystals (MaTecK GmbH) were cleaned by cycles of sputtering with Ar^+ ions at 1 keV and subsequent annealing at ~ 450°C. Deposition of molecules on the substrates was done by thermal evaporation from a commercial evaporator (Kentax GbmH) at ~240°C. Metal adatoms were supplied by e-beam evaporator (Oxford Applied Research). The sublimed amount of the compound was controlled by a quartz crystal microbalance. All STM images were recorded at 5K in constant current mode (Omicron Nanotechnology GmbH) and processed with WSxM software[1]. The STM tip was made of 90% Pt and 10% Ir wire, mechanically cut and sputtered in situ with Ar^+ ions. The XPS measurements were performed at the Laboratory for Micro- and Nano-technology at the Paul Scherrer Institute (PSI). The spectra were recorded in normal emission using a monochromatic Al kα X-ray source which results in a full width at half maximum (FWHM) of 1 eV. Spectra analysis was done with Unifit software.

Computational details

Periodic DFT calculations were done with the VASP code[2], using the projector-augmented wave

method to describe ion-core interactions[3] and with planewaves expanded to a kinetic energy cutoff of 400 eV. The van der Waals density functional[4] described exchange-correlation effects, with the version by Hamada denoted as rev-vdWDF2[5] which has shown to describe adsorption of molecules on coinage metals accurately[6]. For the calculations of adsorbed molecules, the Bi/Cu(100) system was modeled by a four layered Cu(100) slab and a single layer of Bi atoms. The Bi/Cu(100)-$p(10 \times 10)$ system was modeled by the smallest supercell possible for constructing the system by translational periodic boundary conditions, resulting in 200 Cu atoms per layer and unit cell.[7] All calculations were done with a Γ-point only k-point sampling. For the optimization of freestanding networks we found the length of the unit cell vectors by optimizing the structure of a range of lattice parameters. All structures were geometrically optimized until the residual forces on all atoms (except the two bottom layers of the Cu slab) were smaller than 0.01 eV/Å.

2. Deposition of DPDI on bare Cu(100)

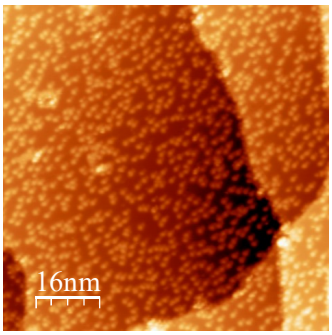

Figure S1: STM micrograph of DPDI on Cu(100). Single native molecules are spread all over the metal substrate. STM image: 80 nm x 80 nm, 1 V, 10 pA.

As can be seen above deposition of DPDI on bare Cu(100) does not lead to the formation of any assembly/network and single molecules are found in their native form spread around on the substrate.

3. XPS studies

Detailed information on coverage dependency XPS:

Coverage	Amino peak (I)	Imino peak (II)
0.4 ML	399.36	398
0.7 ML	399.42	398.08
1 ML	399.44	398.1
10 ML	399.4	397.7

Table 1: Amino & Imino groups peak positions and corresponding information upon coverage increase on the substrate.

1. Orientation of the hexagonal networks with respect to the substrate

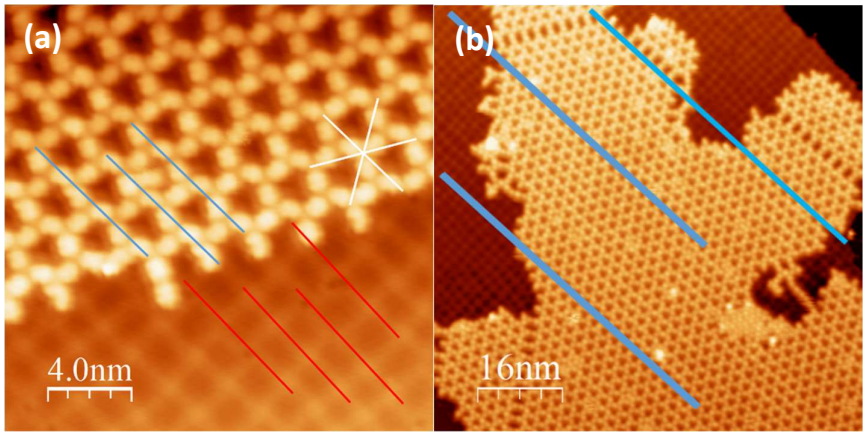

Figure S2: Overall alignment of the DPDI network with the principal axis of the reconstruction of the underlying substrate. a.) The three principal directions of the observed DPDI network are indicated by *white* lines along the directions of the densest linear packing of DPDI. a &b) One of these directions is found to align with the principal axis of the p10x10 reconstruction of the Bi thin film indicating preference of DPDI for the 'node' positions (for the discussion of another supramolecular layer on p(10x10) Bi see Ref [8]. The relative alignment of the network and the near network reconstruction has been determined as indicated: Directions in the network and for the reconstruction close to (within 4-6 unit cells) to the network have been indicated *blue* and *red*, respectively. The analysis of '60' such lines on '6' different DPDI islands on p10x10 Bi revealed a directional alignment of 3 +/- 1 degrees. Similarly, agreement is found between the line spacing of ~ 2.35nm for the DPDI network and ~1.85nm for the p (10x10) Bi. The observed agreement of the lattice parameters of the not strictly regular p (10x10) Bi reconstruction in the vicinity of the DPDI network indicates that this alignment is caused by an adsorbate induced reconstruction.[9]

2. Strength test using STM tip

To test the strength of the networks we tried to break those using STM tip. The tip was crossed very close to the surface. As a result, we could break the H-bonded pores.

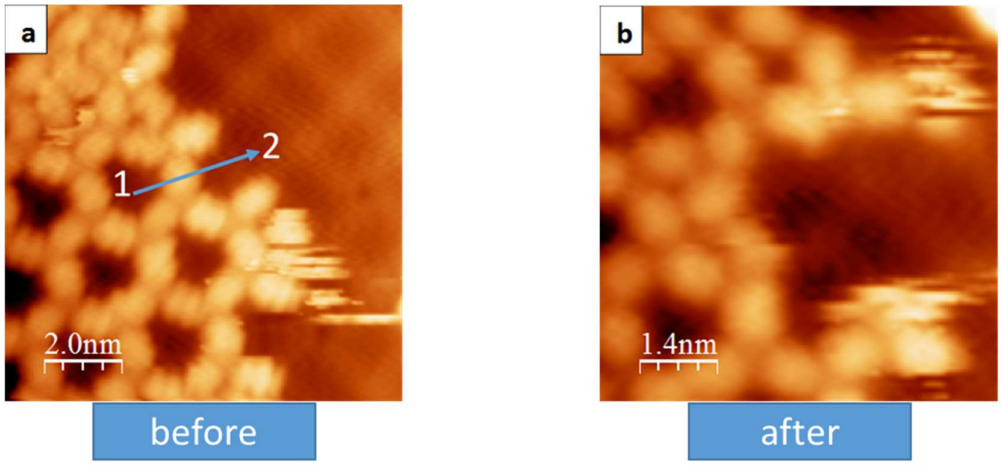

Figure S3: Strength test performed on DPDI pores. a) before breaking. b) after breaking. STM images: a) 10 nm x 10 nm, 1 V, 10 pA. b) 7 nm x 7 nm, 1 V, 10 pA.

Procedure:
1- STM tip was put in position 1
2- Voltage and current values were changed in order to make the tip closer to the surface
3- feedback was switched off
4- tip was moved from position 1 to position 2.
5- Feedback switched on
6- The place was scanned again.

As it can be seen the pore is broken.
This test shows the weakness of the bonds.

3. DFT-Calculations

6.1 Isolated DPDI on Bi-Cu(100)

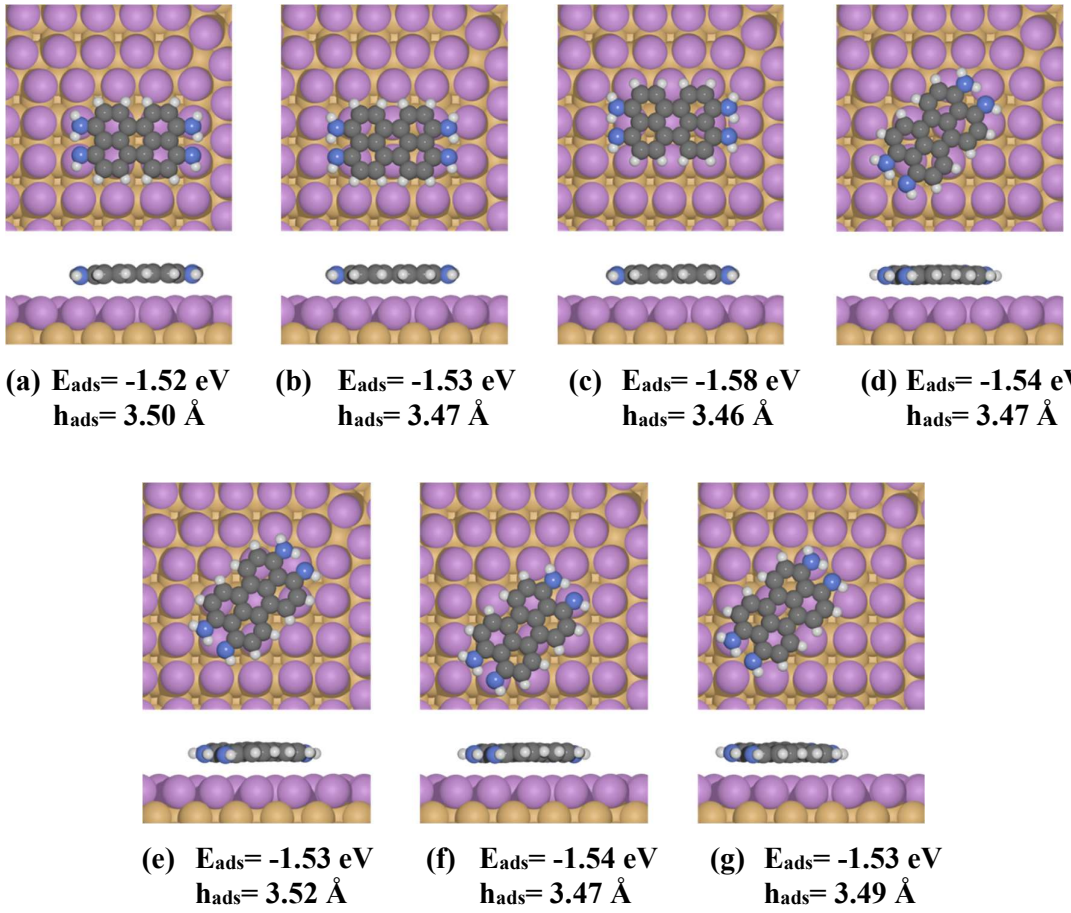

Figure S4: Different possible positions of isolated DPDI molecule (**Tautomer 1**) on Bi/Cu(100) substrate. Adsorption energy and height are mentioned at the bottom of each image.

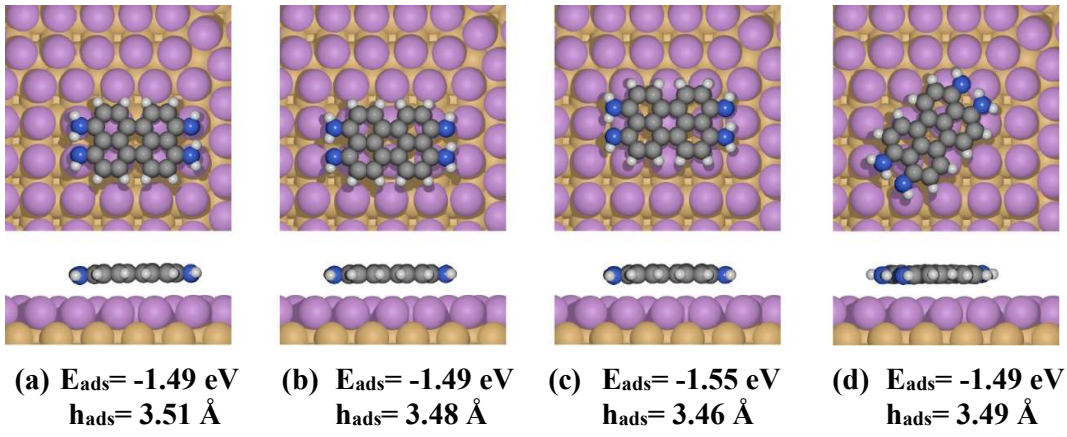

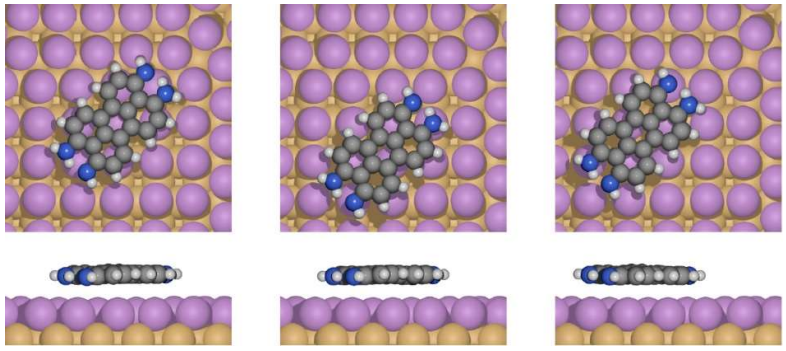

(e) E_{ads}= **-1.49 eV** h_{ads}= **3.53 Å** **(f)** E_{ads}= **-1.50 eV** h_{ads}= **3.48 Å** **(g)** E_{ads}= **-1.50 eV** h_{ads}= **3.49 Å**

Figure S5: Different possible positions of isolated DPDI molecule (**Tautomer 2**) on Bi/Cu(100) substrate. Adsorption energy and height are mentioned at the bottom of each image.

All adsorption energies are given with respect of having tautomer 1 desorbed from the surface.

6.2 Comparison between two tautomers

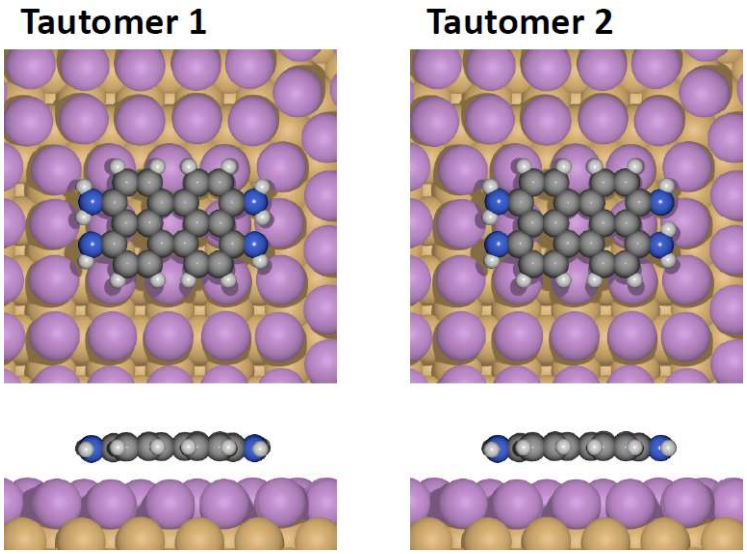

E_{ads}= **-1.58 eV** h_{ads}= **3.46 Å** E_{ads}= **-1.55 eV** h_{ads}= **3.46 Å**

Figure S6: Comparison of adsorption energy and adsorption height between two most stable adsorption configurations of tautomer1 and tautomer 2. There is 0.03 eV difference in energy for the two tautomers when adsorbed on the surface. This should be compared to 0.04 eV which is the energy difference between the two tautomers in the gas phase, so essentially the energy difference between the two tautomers is the same on the surface and in the gas phase. Thus, the Bi-Cu(100) surface does not affect the relative stability between the tautomers.

6.3 DPDI trimer on Bi reconstructed Cu(100)

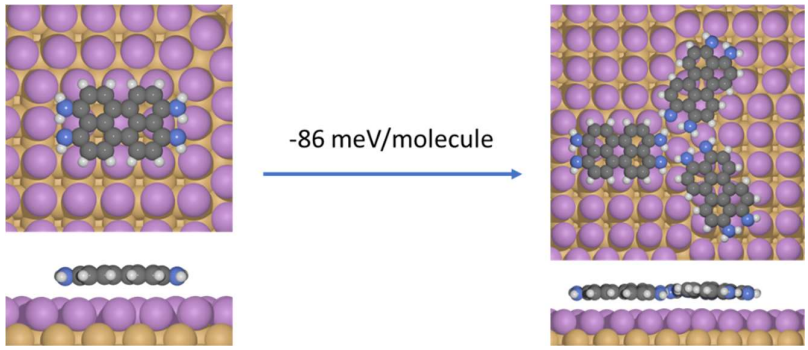

E_{ads}= -1.58 eV
h_{ads}= 3.46 Å

E_{ads}= -1.67 eV/molecule
h_{ads}= 3.62 Å

Figure S7: DFT calculations for the adsorption energy and adsorption height of DPDI trimers (nodes of the hexagonal networks).

Compare this to the formation energy of -345 meV/molecule for the freestanding network 3. But note that the trimer on the surface has half the number of intermolecular interactions per molecule. In other words, the suggested bonding motif is about half as strong on the surface as in the freestanding network. This comes from the fact that the DPDI molecule prefers to adsorb flat on the surface, while in the freestanding network it is quite tilted and the molecules cannot rotate/tilt as freely on the surface (see next figure).

6.4 Comparison between freestanding network and trimer on surface: Tilt of the molecule.

(Compare largest difference in *z*-coordinates of C-atoms for the two scenarios).

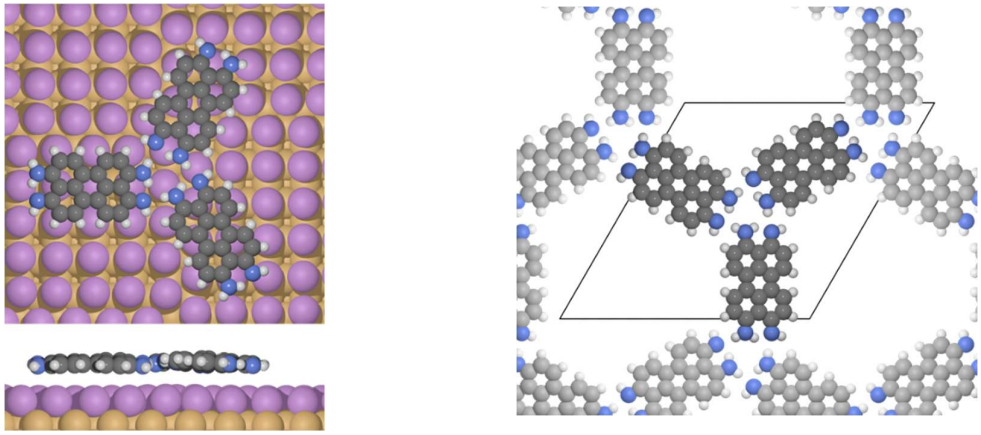

$\Delta z_{\max}(\text{C atoms}) - \Delta z_{\min}(\text{C atoms}) = 1.21$ Å

$\Delta z_{\max}(\text{C atoms}) - \Delta z_{\min}(\text{C atoms}) = 0.55$ Å

Figure S8: Comparison of the largest difference in *z*-coordinates of C-atoms between freestanding model and trimers on Bi/Cu(100) substrate.

6.5 Electron density map with different absolute value of contours (0.005 e/Å^3)

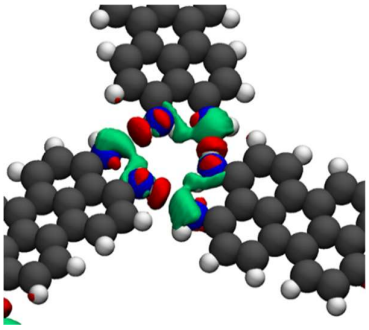

Figure S9: Electron density redistribution due to intermolecular interactions. Green: electron accumulation, Red: electron depletion. This map shows how this network is stabilized by an intermolecular H-bond with the amine as H-bond donor and imine as H-bond acceptor, at some cost of weakening the corresponding intramolecular H-bond.

6.6 Freestanding intact DPDI networks

In the following sections, different possible hexagonal networks composed of DPDI in its different tautomeric forms is presented. The most stable network which is the most similar to STM results is represented in the main text and section 7.6.4 (network 3)

6.6.1 Network 1: Nodes have the same chirality

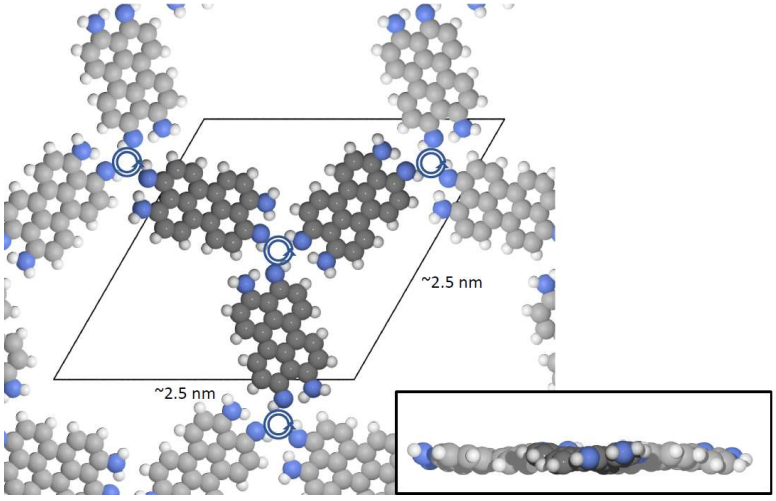

Figure S10: Freestanding DPDI network composed of tautomer 2. As can be seen the nodes of the network have the same chirality. The imine nitrogens act as both H-bond acceptors and donors for intermolecular H-bonds. Formation energy is around -120 meV/molecule.

6.6.2 Network 2: Nodes have the same chirality

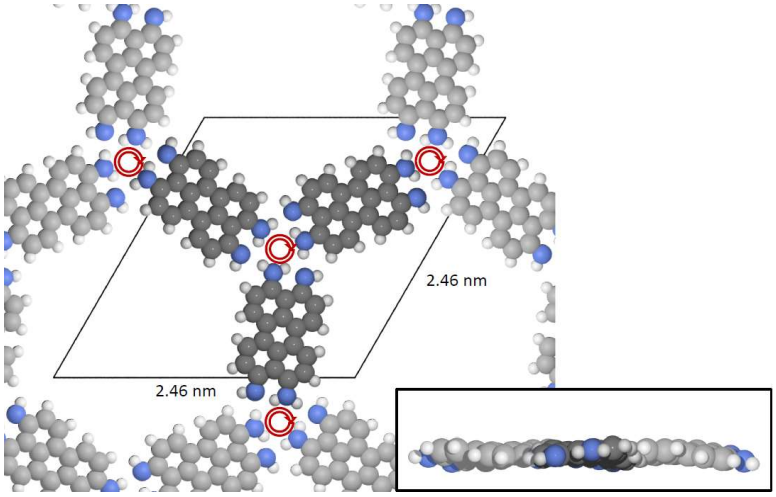

Figure S11: Freestanding DPDI network composed of tautomer 2. As can be seen the nodes of the network have the same chirality. The imine nitrogens act as H-bond acceptors, and amine nitrogens as H-bond donors, for intermolecular H-bonds. Formation energy is around -260 meV/molecule.

6.6.3 Network 2 flat: Nodes have the same chirality

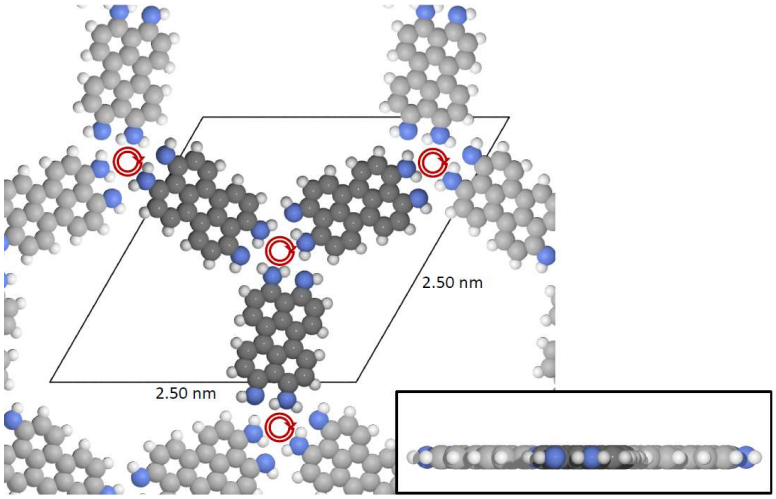

Figure S12: Freestanding DPDI network composed of tautomer 2. As can be seen the nodes of the network have the same chirality. Formation energy is around -262 meV/molecule.

6.6.4 Network 3: Nodes have alternating chirality

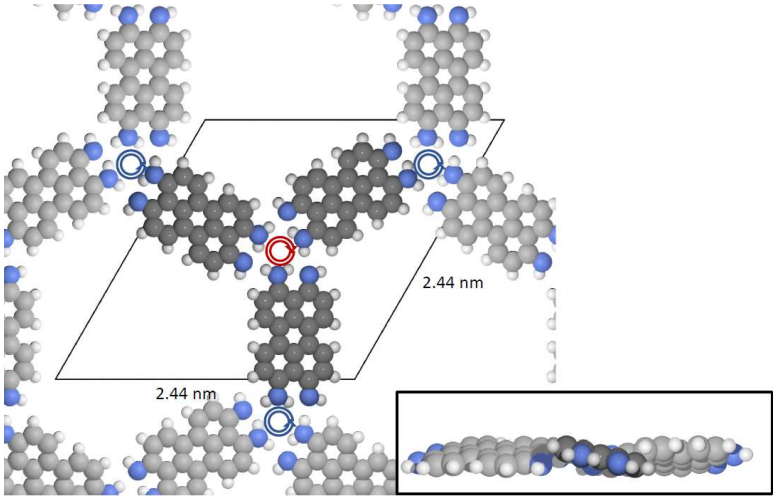

Figure S13: Freestanding DPDI network composed of tautomer 1. As can be seen the nodes of the network have alternating chirality, this model is presented in the main text too and fits well with experimentally obtained STM data. The bonding motifs are the same as in network 2, but alternating chirality between the nodes. Formation energy is around -345 meV/molecule so it is more stable comparing to network 2. It is also clear why network 3 is more stable than network 2, although the binding motifs look similar. In network 3, the molecule can easily tilt with the amines in one direction and the imines in the other direction, this way optimizing the bonding.

Comparing the two most stable networks in gas phase, network 2 (homochiral) and network 3 (heterochiral) shows that heterochiral network is 85 meV/molecule more stable than the homochiral network. So, regarding the results above, half of this energy difference comes from tautomer 1 being more stable. The remaining energy difference could be assigned to the fact that in the homochiral network the molecule is slightly twisted, while in the heterochiral network the molecule is tilted (or rotated around its long axis) and can better keep its structural integrity. So these results seem to indicate that the heterochiral network would be preferred even if the two tautomers were equally stable. However, if we consider the interaction between three molecules on the surface (sections 7.3 & 7.4), the formation energy from isolated molecules is smaller than for the freestanding network. The estimated formation energy of a network is 172 meV/molecule (2 times 86 meV), compared to 345 meV/molecule for the freestanding network. The tilt of the molecule is much smaller on the surface, since the molecule-surface interaction strive for flat adsorption. This indicates that on the surface homo vs heterochirality is of less importance, from a network point of view and the tautomerization maybe more important.

6.6.5 Network 3 flat: Nodes have alternating chirality

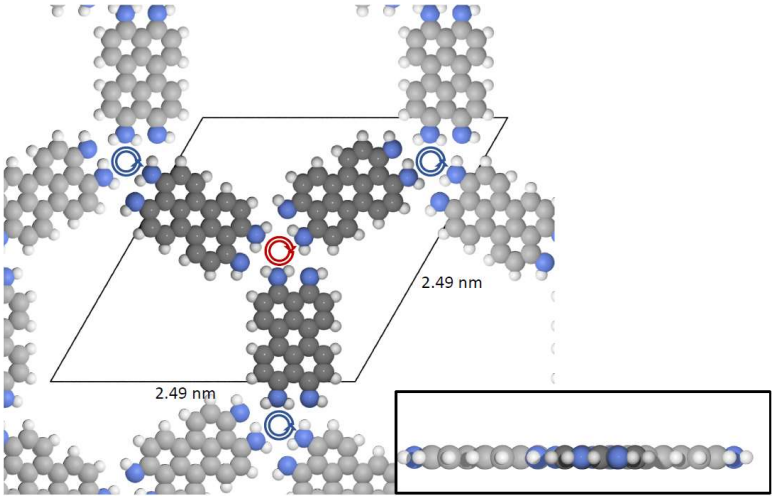

Figure S14: Freestanding DPDI network composed of tautomer 1 in its flat form. As can be seen the nodes of the network have alternating chirality. Formation energy is around −279 meV/molecule.

6.7 Different starting geometries

6.7.1 Network 4: different starting geometry optimizes to heterochiral version of network1

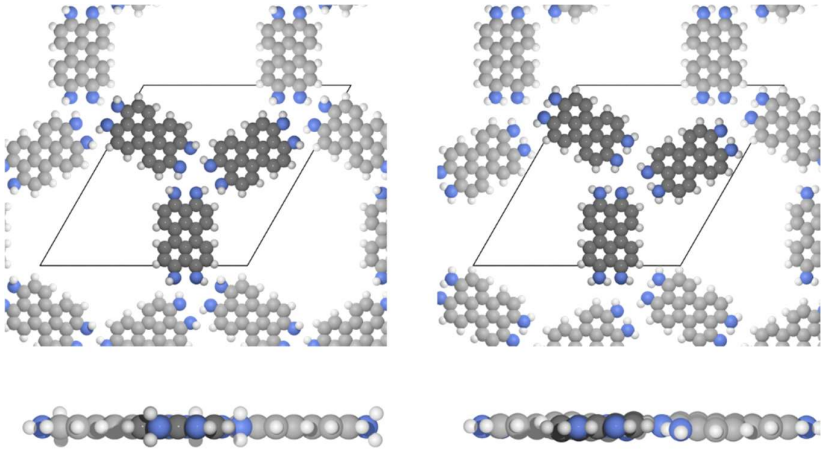

Starting geometry

Optimizes into heterochiral version of network 1

Figure S15: Freestanding DPDI network with different starting geometry. The network eventually optimizes to heterochiral version of network1.

6.7.2 Network 5: different starting geometry optimizes to network 3

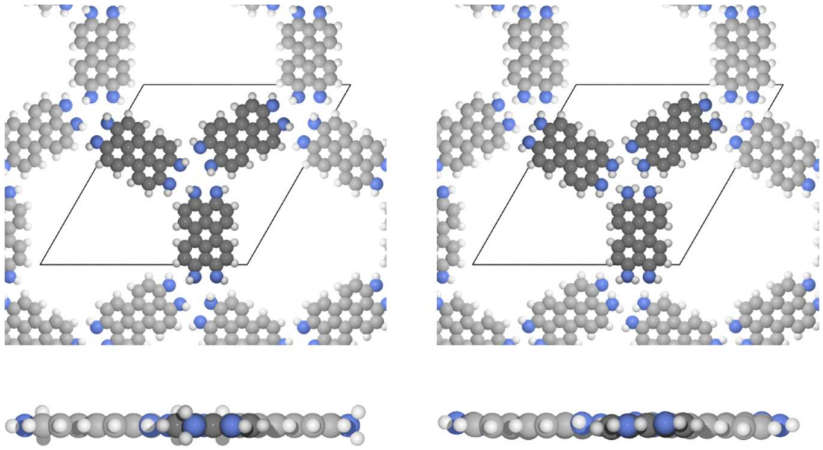

Figure S16: Freestanding DPDI network with different starting geometry. The network eventually optimizes to network3.

6.8 Geometry of gas phase calculation of l-DPDI and x-DPDI

The DFT calculations were carried out using ORCA 4.0.1 program package.[10] B3LYP was employed as functional[11] and a def2-SVP basis set was used for all atoms during geometry optimizations.[12] Single point calculations were performed using a def2-QZVPP basis set.[13]

6.8.1 xyz-Coordinates of l-DPDI

* xyz 0 1

N	20.070157000	-5.569409000	0.058058000
N	22.394089000	-6.661749000	0.432228000
C	20.151168000	-5.969767000	-1.228483000
C	19.078532000	-5.686105000	-2.126768000
C	19.129297000	-6.060208000	-3.443590000
H	18.280921000	-5.805911000	-4.078564000
C	20.247634000	-6.752316000	-3.991974000
C	21.330099000	-7.058863000	-3.112678000
C	21.288755000	-6.672240000	-1.727681000
C	22.401486000	-7.007847000	-0.828667000
C	23.507270000	-7.751047000	-1.422504000

C	23.536632000	-8.097401000	-2.731523000
H	24.398870000	-8.656880000	-3.093211000
C	20.295551000	-7.139354000	-5.381924000
N	22.751440000	-9.243106000	-9.086623000
N	20.381442000	-8.262139000	-9.451586000
C	22.672549000	-8.890736000	-7.829871000
C	23.747917000	-9.155026000	-6.881094000
C	23.673969000	-8.803088000	-5.575168000
H	24.520321000	-9.043629000	-4.932502000
C	22.524497000	-8.124403000	-5.015737000
C	21.433829000	-7.821803000	-5.908976000
C	21.488726000	-8.204068000	-7.294289000
C	20.384659000	-7.910023000	-8.149084000
C	19.260411000	-7.225404000	-7.596385000
C	19.224298000	-6.856865000	-6.277611000
H	18.340986000	-6.328697000	-5.919761000
C	22.467451000	-7.765598000	-3.648386000
H	18.418890000	-6.988114000	-8.253754000
H	18.204857000	-5.152240000	-1.741238000
H	24.333607000	-8.031663000	-0.762060000
H	24.637053000	-9.665046000	-7.265557000
H	20.870666000	-5.824043000	0.662989000
H	19.231351000	-5.114149000	0.390908000
H	23.240937000	-6.988598000	0.903998000
H	23.644491000	-9.702296000	-9.282138000
H	19.587678000	-8.031446000	-10.032971000
H	21.234818000	-8.737994000	-9.794301000

*

6.8.2 xyz-Coordinates of x-DPDI

* xyz 0 1

N	20.054073000	-5.580261000	0.035775000

N	22.391019000	-6.603125000	0.433051000
C	20.145105000	-5.989348000	-1.244211000
C	19.063571000	-5.733696000	-2.148795000
C	19.122901000	-6.111411000	-3.459798000
H	18.269480000	-5.879949000	-4.096148000
C	20.259597000	-6.789755000	-4.006385000
C	21.349011000	-7.076976000	-3.112876000
C	21.296141000	-6.672935000	-1.731058000
C	22.412083000	-6.971058000	-0.824232000
C	23.531565000	-7.696593000	-1.407508000
C	23.561454000	-8.066676000	-2.712785000
H	24.434318000	-8.612905000	-3.070163000
C	20.317307000	-7.176160000	-5.380776000
N	22.745392000	-9.373720000	-9.044292000
N	20.419196000	-8.327356000	-9.446989000
C	22.653765000	-8.966973000	-7.763423000
C	23.729937000	-9.234188000	-6.855906000
C	23.671947000	-8.854471000	-5.545298000
H	24.521425000	-9.094732000	-4.906921000
C	22.540482000	-8.165358000	-5.001353000
C	21.453236000	-7.873472000	-5.896038000
C	21.506920000	-8.274942000	-7.278563000
C	20.395774000	-7.965925000	-8.187915000
C	19.278474000	-7.236371000	-7.605314000
C	19.245801000	-6.872851000	-6.298337000
H	18.375185000	-6.322541000	-5.941675000
C	22.485751000	-7.772739000	-3.628444000
H	18.446652000	-6.977568000	-8.267681000
H	18.179177000	-5.216340000	-1.765055000
H	24.367822000	-7.946452000	-0.747274000
H	24.609940000	-9.760770000	-7.237198000
H	20.867675000	-5.814990000	0.639606000
H	19.207117000	-5.136825000	0.365024000

H	23.241832000	-6.902877000	0.914938000
H	23.588713000	-9.826043000	-9.371022000
H	19.571823000	-8.020120000	-9.929988000
H	21.936258000	-9.129754000	-9.650290000

*

References:

1. Horcas I, Fernández R, Gómez-Rodríguez JM, Colchero J, Gómez-Herrero J, Baro AM. *Rev Sci Instrum*. 2007;**78,** 013705.

2. Kresse G, Furthmüller J. *Phys Rev B*. 1996; **54,** 11169-11186.

3. Blöchl PE. *Phys Rev B*. 1994; **50,** 17953-17979.

4. Dion M, Rydberg H, Schröder E, Langreth DC, Lundqvist BI. *Phys Rev Lett*. 2004; **92,** 246401.

5. Hamada I. *Phys Rev B*. 2014; **89,** 121103.

6. Björk J, Stafström S. *ChemPhysChem*. 2014; **15,** 2851-2858.

7. Meyerheim HL, De Santis M, Moritz W, Robinson IK. *Surf Sci*. 1998; **418,** 295-302.

8. Wäckerlin A, Fatayer S, Nijs T, Nowakowska S, Mousavi S.F, Popova O, Ahsan A, Jung T.A, Wäckerlin C. *Nano Lett*. 2017; **17,** 1956-1962.

9. Oura K. *Surface Science: An Introduction ; with 16 Tables*. Berlin: Springer; 2003.

10. Neese, F. *Wiley Interdiscip. Rev. Comput. Mol. Sci.* 2012, **2**, 73-78.

11. (a) Becke, A. D. *J. Chem. Phys.* 1993, **98**, 1372-1377; (b) Becke, A. D. *J. Chem. Phys.* 1993, **98**, 5648.

12. (a) Lee, C.; Yang, W.; Parr, R. G. *Phys. Rev. B* 1988, **37**, 785-789; (b) Weigand, F.; Häser, M.; Patzelt, H.; Ahlrichs, R. *Chem. Phys. Lett.* 1998, **294**, 143-152.

13. Weigand, F.; Ahlrichs, R. *Phys. Chem. Chem. Phys.* 2005, **7,** 3297-3305.

Chapter 2

Chapter [[3]] and Supplementary Information

[[3]] – Substitution of Mutually Interacting Substituents for Monolayer Engineering of Tetraphenylporphyrin Surface Self-assembled Structures

S. Fatemeh Mousavi, Aisha Ahsan, Luiza Buimaga-Iarinca, Cristian Morari, Mehdi Heydari, Ondrej Sedlacek, Waka Nakanishi, Yutaka Wakayama, Katsuhiko Ariga, Jonathan P. Hill and Thomas A. Jung

Contribution of S. F. Mousavi: carried out experimental investigations (STM & XPS), analyzed and interpreted the data, wrote the manuscript

Substitution of Mutually Interacting Substituents for Monolayer Engineering of Tetraphenylporphyrin Surface Self-assembled Structures

S. Fatemeh Mousavi[a], Aisha Ahsan[a], Luiza Buimaga-Iarinca[b], Cristian Morari[b], Mehdi Heydari[c], Ondrej Sedlacek[d], Waka Nakanishi[d], Yutaka Wakayama[d], Katsuhiko Ariga[d], Jonathan P. Hill[d] and Thomas A. Jung[c].

[a] Department of Physics, University of Basel, Klingelbergstrasse 82, 4056 Basel, Switzerland.
[b] National Institute for Research and Development of Isotopic and Molecular Technologies (NIRDIMT) 65-103Donath, Ro-400293, Cluj-Napoca, Romania
[c] Laboratory for Micro- and Nanotechnology, Paul Scherrer Institute, 5232 Villigen PSI, Switzerland.
[d] International Center for Materials Nanoarchitectonics, National Institute for Materials Science, Namiki 1-1, Tsukuba, Ibaraki 305-0044, Japan

The self-assembly of small organic molecules at metal surfaces is a valid method for generating pristine nanostructured films over large areas of substrate and could lead to the development of information storage devices if stable molecules with appropriate properties are utilized[1,2]. For this reason, the surface self-assembly of porphyrins, phthalocyanines and their derivatives have been intensively studied because of their chemical properties (multiple stable oxidation states, intense electronic absorption, excellent stabilities) and nanometric dimensions[3,4]. Different methods have been applied for their assembly including hydrogen bonding, transition metal atom coordination and covalent linkage often yielding extended monolayers with highly homogeneous structures[5–7]. On the other hand, while self-assembly involving fluorophilic interactions (F…F interactions and C-F…H-C hydrogen bonds) has been studied in crystalline and gel states[8–10] there is less known about their utility as structure-directing forces in organic assemblies at surfaces, in particular, for tetraphenylporphyrins. F…F interactions and C-F…H-C hydrogen bonds are well-known in planar perfluorinated phthalocyanine monolayers and binary assemblies with planar hydrocarbons since coplanarity of the interacting moieties optimizes the possible intermolecular interactions[11]. However, in the more flexible tetraphenylporphyrins less is known about how the presence of units that can interact through fluorophilic forces and related hydrogen bonds or their combinations can affect surface self-assembly structures.

In this work, we consider the cases of two functional groups known to interact either through hydrogen bonding, fluorophilic interactions or combinations. In order to study such possible interactions 4 new compounds were successfully synthesized

- TRANS: 5,15-Bis(3,5-trifluoromethylphenyl)-10,20-bis(3,4,5-trimethoxyphenyl)porphyrin

- MONO: 5-(3,4,5-trimethoxyphenyl)-10,15,20-tris(3,5-trifluoromethylphenyl)porphyrin
- MeOTPP: tetrakis(3,4,5-trimethoxyphenyl)porphyrin
- CF3TPP: tetrakis(3,5-trifluoromethylphenyl)porphyrin

The chemical structures of these compounds can be found in scheme 1.

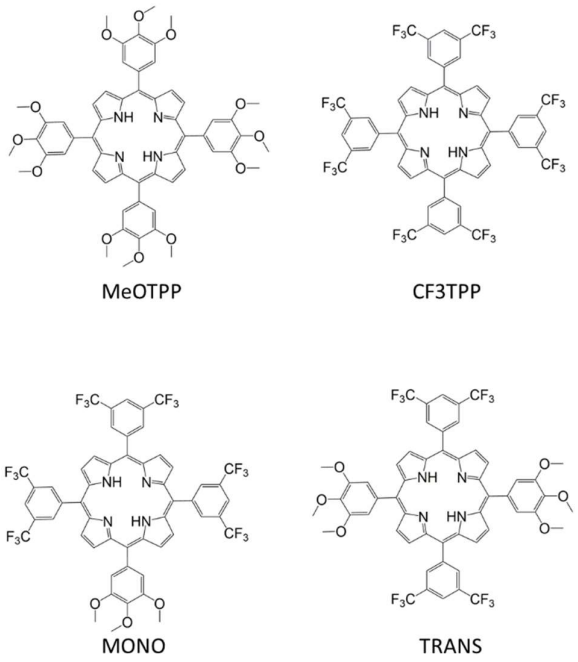

Scheme 1: Structures of the functionalized tetraphenylporphyrins.
On surface in-situ behavior of these compounds was studied using Scanning Tunneling Microscopy (STM) and X-ray photoelectron spectroscopy (XPS).

Both compounds (Trans and Mono) show a similar flower shape morphology upon deposition on Cu(111) which resembles their chemical porphyrin based structure.

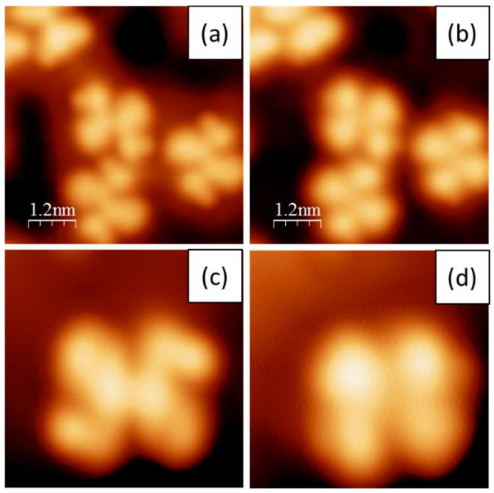

Figure1: STM micrographs of on surface behavior of Trans upon deposition on Cu(111). a & b) images recorded with opposite biases (500mV & -500mV) showing the distribution of compounds

on substrate. b & c) Zoomed-in images recorded with opposite biases (720mV & -720mV). STM information: a) 6x6nm, 30pA, 500mV. b) 6x6nm, 30pA, -500mV. c) 3x3nm, 200pA, 720mV. d) 3x3nm, 200pA, -720mV.

The methoxy side of the compounds is distinguishable considering its double lobe appearance comparing with the single lobe appearance of CF3 side. The compounds are mostly individually adsorbed on the substrate, however, looking at big overviews one can see that they intent to interact with each other despite strong interaction with the substrate. (Fig. 2)

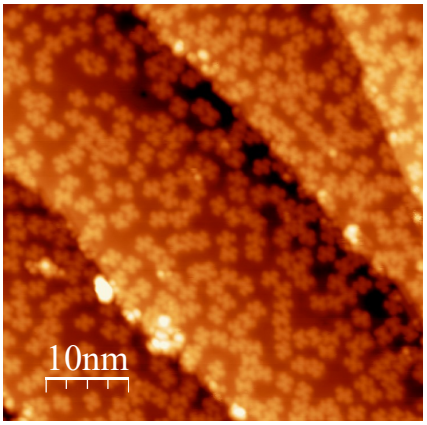

Figure 2: Overview STM image showing the overall distribution of compounds on Cu(111) substrate. As can be seen, there is strong interaction with the substrate and molecules are individually adsorbed. There is also an intermolecular interaction guiding the compounds to get closer to each other. STM information: 50x50n, 10pA, 1V

Similar to Trans, Mono also shows a flower shape STM footprint. The asymmetric form of Mono is clearly seen in STM images, the only double lobe side is representing Methoxy side and the rest are Trifluoromethyl groups. Mono compounds also distribute individually on Cu(111) substrate with an intention to interact with each other despite strong molecules-substrate interaction. (Fig. 3- overview image can be found in SI- Fig. S1)

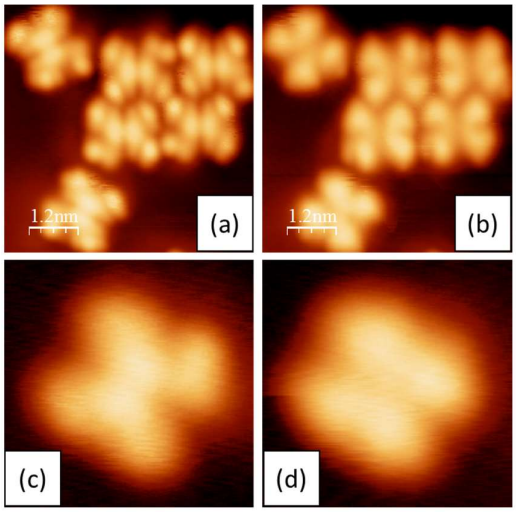

Figure 3: STM micrographs of on surface behavior of Mono upon deposition on Cu(111). a & b)

images recorded with opposite biases (1V & -1V) showing the distribution of compounds on substrate. b & c) Zoomed-in images recorded with opposite biases (1V & -1V). STM information: a) 7x7nm, 10pA, 1V b) 7x7nm, 10pA, -1V c) 3x3nm, 10pA, 1V d) 3x3nm, 10pA, -1V

As can be seen in figure 3, the molecules appear differently in images with different applied biases. The images recorded with positive and negative tip biases are representing occupied and unoccupied states respectively.

XPS was used to understand the chemical on surface properties of the compounds (Fig. 4 & S9). Figure 4 shows the XP spectra of F1s, O1s and N1s for a monolayer of Trans deposited on Cu(111) and it compares it with the multilayer sample. F1s XP spectrum contains two peaks at 688.8eV and 687.8eV (Fig. 4a) while the F1s spectrum for multilayer sample contains one peak at 688.8eV (Fig. 4d). Comparing these two cases one can realize that the extra peak in monolayer XPS comes from either intermolecular or molecules-substrate interaction.

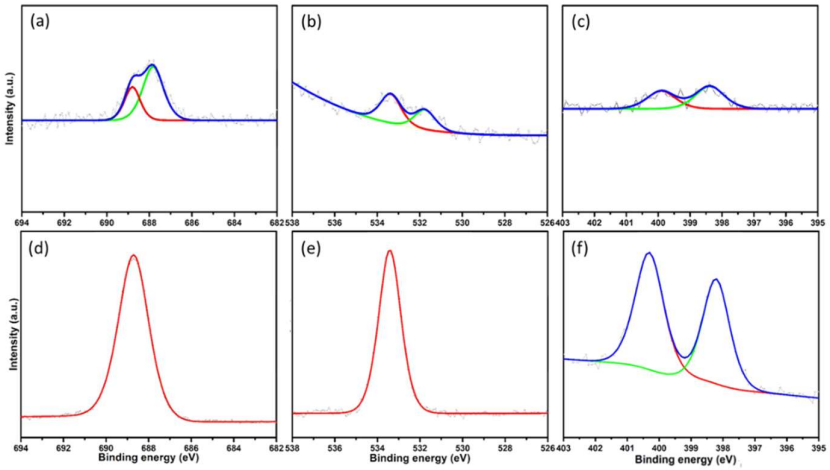

Figure 4: XP spectrum of F1s, O1s and N1s of a monolayer of Trans deposited on Cu(111) and comparison with multilayer sample. a) F1s XP spectrum for monolayer sample. b) O1s XP spectrum for monolayer sample. c) N1s XP spectrum for monolayer sample. d) F1s XP spectrum for multilayer sample. e) O1s XP spectrum for multilayer sample. f) N1s XP spectrum for multilayer sample.

The F1s spectrum contains two peaks at 688.8 and 687.8 eV with an area ratio of approximately 1:2 suggesting that 2 fluorine atoms of each trifluoromethyl group interact with the metal substrate. The XPS spectrum of the multilayer confirms this since substrate-interacting F atoms are more difficult to observe. Similarly, the O1s XP spectrum of the monolayer shows two peaks at 533.3eV and 531.7eV but a single peak in the multilayer sample for the same reason. N1s XP spectrum contains two peaks assignable to imine-type and pyrrole NH-type nitrogen atoms for monolayer and multilayer because proximity to the surface does not affect this ratio. Our current DFT models are based on this theory and nicely describe the formation of different self-assemblies.

For DFT please see section 4 of SI.

Similar conclusion can be made from XP spectra of monolayer and multilayer samples of Mono on Cu(111). (Fig. S9). These compounds have been studied on other substrates too: Ag(111) and Au(111). Interestingly, upon deposition of them on the mentioned substrates, the compounds appear in the form of different self-assemblies. Figure 5 shows the self-assemblies of Trans and Mono upon deposition on Ag(111). For more images taken with negative biases please check section 2 of SI (Fig. S2). The fact that these self-assemblies are highly ordered and are long ranged suggests the possibility of having H-bonds as bonding motif.

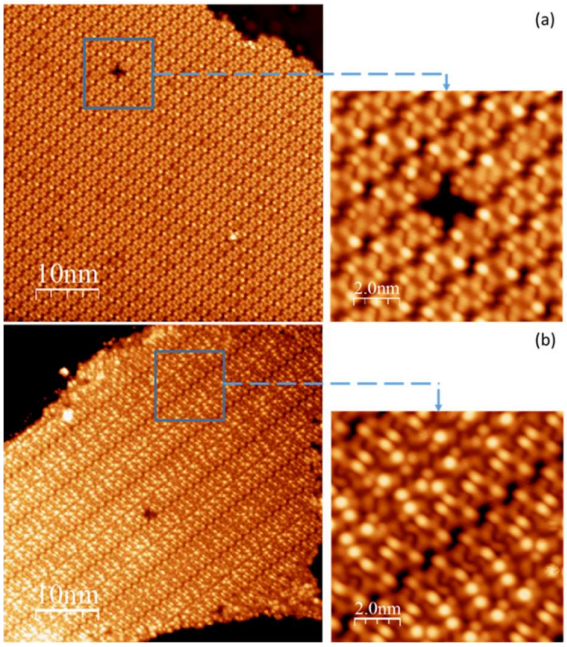

Figure 5: Compact self-assemblies of Trans and Mono after deposition on Ag(111) substrate. a) Overview STM micrograph of Trans/Ag(111) and zoomed-in image. b) Overview STM micrograph of Mono/Ag(111) and zoomed-in image. STM information: a) 50x50nm, 20pA, 250mV. 10x10nm, 20pA, 250mV. b) 50nm x 50nm, 20pA, 600mV. 10nm x 10nm, 20pA, 600mV.

XPS data taken from the samples containing above mentioned self-assemblies again suggests the possibility of having a chemical on surface reaction prior to the H-bonding self-assembly. (For more details please check section 3 of SI, Fig. S10 & S11). DFT model description for the above mentioned self-assembly can be found in section 4 of SI.

Similar to Ag(111), deposition of Trans and Mono on Au(111) leads to the formation of compact and long-range ordered self-assemblies (Fig. 6). Images recorded with different biases are presented in section 2 of SI Fig. S3.

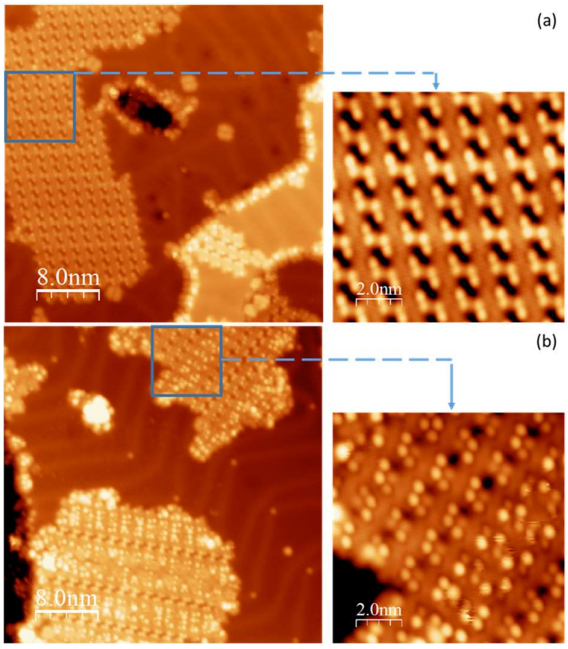

Figure 6: Compact self-assemblies of Trans and Mono after deposition on Au(111) substrate. a) Overview STM micrograph of Trans/Au(111) and zoomed-in image. b) Overview STM micrograph of Mono/Au(111) and zoomed-in image. STM information: a) 40x40nm, 30pA, 500mV. 10x10nm, 30pA, 500mV. b) 40nm x 40nm, 10pA, 1V. 10nm x 10nm, 30pA, 500mV.

Since for both Trans and Mono, F1s and O1s XP spectra show one peak more comparing to the multilayer samples, we are expecting a chemical reaction to happen prior to the self-assembly of compounds via H-bonding. (For details please check section 3 of SI, Fig. S12 and S13).

In order to better understand the physical and chemical properties of Trans and Mono compounds, the symmetric form of them was also synthesized and studied using STM and XPS. MeOTPP and CF3TPP are tetraphenylporphyrin compounds which are fully functionalized with methoxy and Trifluoromethyl groups respectively. MeOTPP, the methoxy functionalized compound have been successfully studied in-situ and its behavior is investigated on different substrates. The four lobe morphology of MeOTPP is clearly seen after its deposition on Cu(111). Upon deposition the compounds are mostly seen individually adsorbed on the substrates (Fig. 7, for overview STM image please refer to section 2 of SI, Fig. S4). There are tiny spots appearing upon deposition which are most probably decomposition compounds. For XPS please see section 3 of SI, Fig. S14)

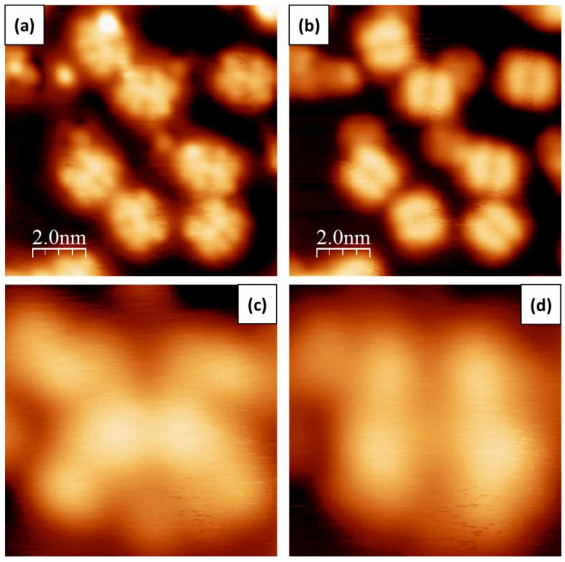

Figure7: STM micrographs of on surface behavior of MeO upon deposition on Cu(111). a & b) images recorded with opposite biases (1.5V & -1.5V) showing the distribution of compounds on substrate. b & c) Zoomed-in images recorded with opposite biases (700mV & -700mV). STM information: a & b) 10x10nm, 10pA. c & d) 2.3x2.3nm, 30pA.

On surface behavior of MeOTPP was also studied on Ag(111). Interestingly, after deposition long ranged ordered self-assemblies appeared on the substrate (Fig. 8, for overview images please check section 2 of SI, Fig. S5). These Kagome lattice nanostructures are composed of intact molecules bonded to each other via hydrogen bonding. This can be understood considering XPS studies which show that there is no special difference in XP spectra of monolayer and multilayer samples. (for XPS please see section 3 of SI, Fig. S15)

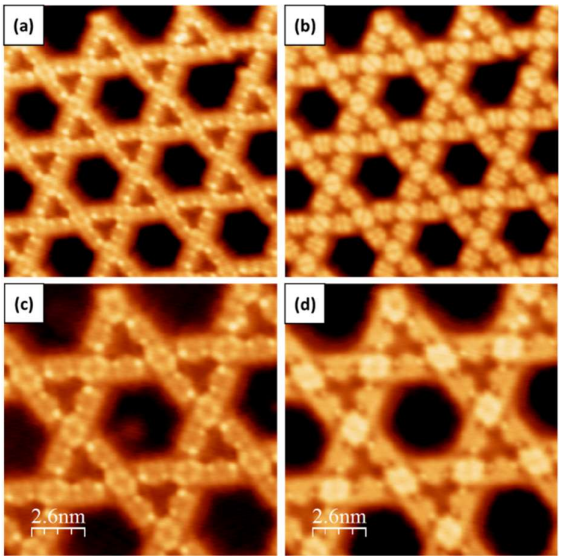

Figure 8: STM micrographs of MeO networks on Ag(111). a & b) images recorded with opposite biases (1V & -1V) showing the chiral star shaped networks. b & c) Zoomed-in images recorded with opposite biases (200mV & -200mV). STM information: a & b) 20x20nm, 10pA. c & d) 13nm x 13nm, 30pA.

Our proposed model for these nicely ordered Kagome lattice structures, shows the possible hydrogen bonds considering the orientation of the molecules and intermolecular distances.

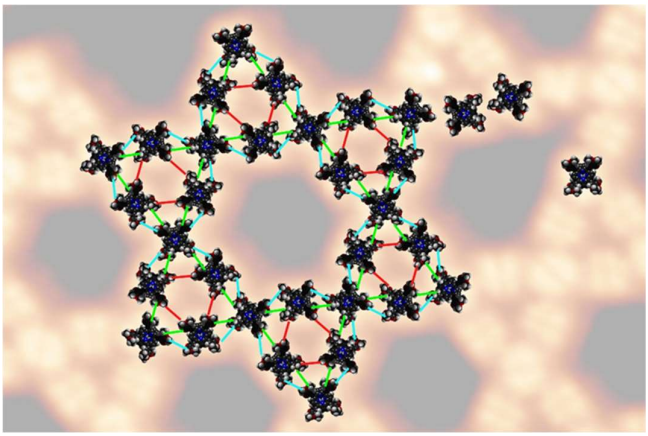

Figure 9: Proposed model for Kagome lattice structure of MeOTPP on Ag(111). Location of hydrogen bonds: Green: probable, Light blue: less likely, Red: possible.

Deposition of MeOTPP on Au(111) single crystal, leads to the formation of chains which are mostly aligned in the direction of herringbone structures of Au (Fig. 9, for overview image please check section 2 of SI, Fig. S6). These structure are also most probably hydrogen bonded. XPS studies for a monolayer of MeOTPP deposited on Au(111) shows a possible on surface chemical reaction involving oxygens (for XPS please check section 3 of SI, Fig. S16). The O1s XP spectrum contains three peaks at 530.4 eV, 531.55eVand 532.93eV, it may also be due to different binding energies of oxygens in methoxy groups.

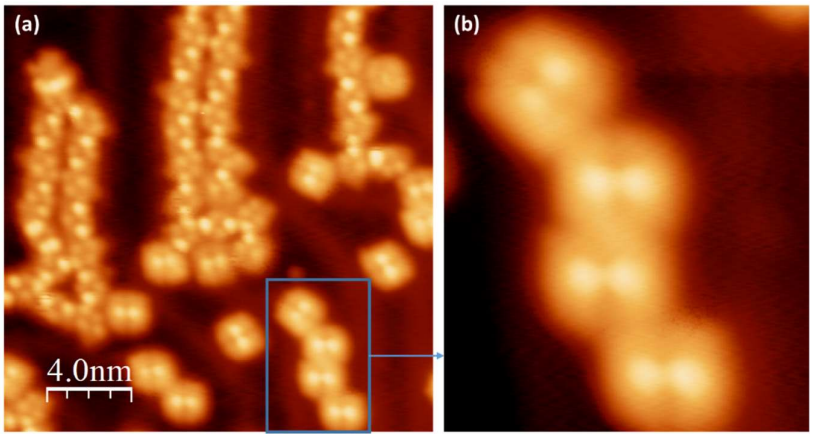

Figure 9: STM micrographs of MeO chains on Au(111). a) STM image showing the formation of MeO chains in between the herringbone structure of Au(111). b) Zoomed-in STM image. STM information: a) 10pA, 1V, 20nm x 20nm. b) 10pA, 1V, 7nm x 6nm

The next symmetric compound which we studied to compare with Trans/Mono compounds is a tetraphenylporphyrin based compound functionalized with Trifluoromethyl at each corner. Interestingly the deposition of CF3TPP was only successful in the case of the inert, non-reactive

substrate, Au(111). The compounds were mostly decomposed and destroyed upon deposition on Cu(111) and Ag(111). (for more information please check section 2 of SI, Fig. S7 & S8). Deposition of CF3TPP on Au(111) leads to the formation of two coexisting phases which are very unstable even at 4K. The unstability of the compounds is clearly seen in STM by moving objects and lines. (Fig. 10)

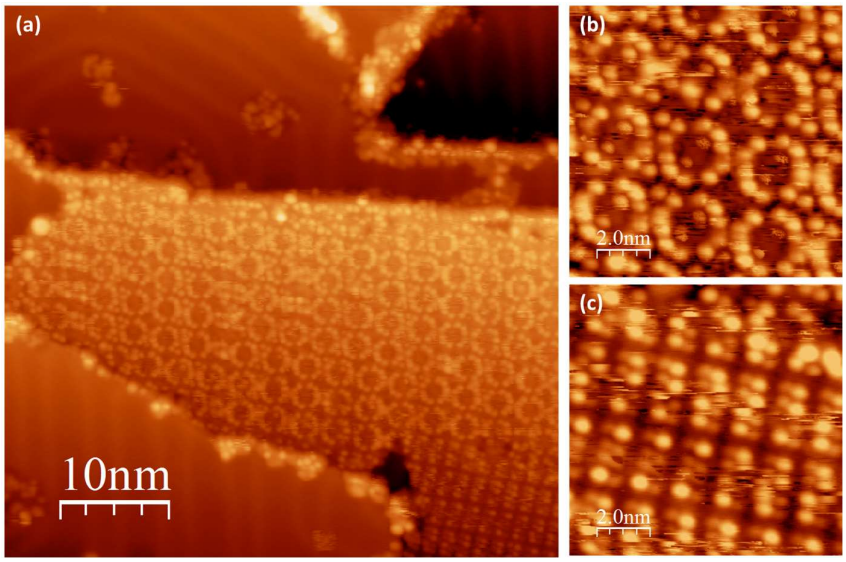

Figure10: STM micrographs of CF3 assemblies on Au(111). Two coexisting phases of porous network and compact assemblies all observed in long range a) STM image showing the formation of two coexisting phases upon deposition. b) Zoomed-in STM image taken on porous networks. c) Zoomed-in STM image taken on compact assemblies. STM information: a) 50nm x 50nm, 10pA, 1V. b) 50pA, 300mV, 10nm x 10nm. c) 10pA, 1V, 10nm, 10nm

Our proposed model for these self-assemblies describe different conformers of the compounds and intermolecular hydrogen bonding motif which drives the formation of the self-assembly.

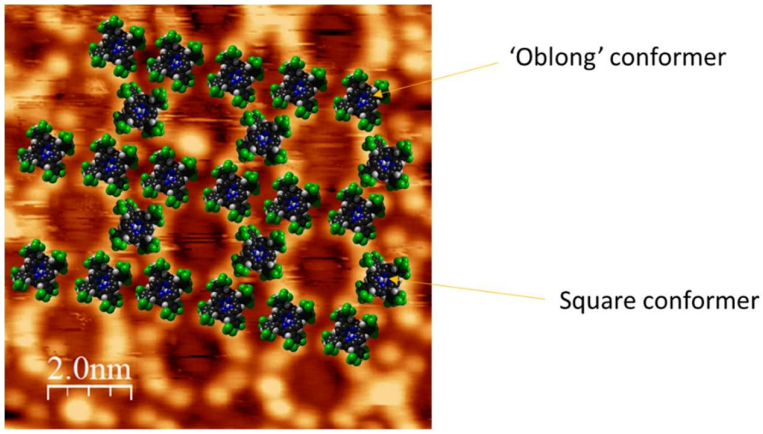

Figure11: Proposed model describing the formation of hydrogen bonded self-assemblies of CF3TPP on Au(111) involving two different conformers of the compounds.

In summary, the effect of functionalization of tetraphenylporphyrins with Trifluoromethyl and methoxy groups in their on-surface self-assemblies is studied. The resulted self-assemblies have different characteristics and features on different substrates (Cu/Ag/Au). Moreover, to have a general comparison, the on-surface behavior of tetraphenylporphyrins which are fully functionalized with the mentioned chemical groups is presented. This study is an unprecedented example for on-surface self-assemblies involving F…F interactions and C-F…H-C hydrogen bonds. As discussed above, while MeOTPP and CF3TPP both form unique structures, such as Kagome and porous structures due to intermolecular interactions including methoxy-methoxy interactions (probably hydrogen bonding) and fluorophilic interactions, Trans and Mono form extended monolayers due to the combination of these effects. This work illustrates how even relatively weak intermolecular interactions can be engineered to yield highly desirable uniform monolayer structures.

References:

1. Mali, K. S., Adisoejoso, J., Ghijsens, E., De Cat, I. & De Feyter, S. Exploring the Complexity of Supramolecular Interactions for Patterning at the Liquid–Solid Interface. *Acc. Chem. Res.* **45,** 1309–1320 (2012).
2. Nowakowska, S. *et al.* Interplay of weak interactions in the atom-by-atom condensation of xenon within quantum boxes. *Nat. Commun.* **6,** (2015).
3. Auwärter, W., Écija, D., Klappenberger, F. & Barth, J. V. Porphyrins at interfaces. *Nat. Chem.* **7,** 105–120 (2015).
4. Gottfried, J. M. Surface chemistry of porphyrins and phthalocyanines. *Surf. Sci. Rep.* **70,** 259–379 (2015).
5. Buchner, F. *et al.* Diffusion, Rotation, and Surface Chemical Bond of Individual 2 *H* -Tetraphenylporphyrin Molecules on Cu(111). *J. Phys. Chem. C* **115,** 24172–24177 (2011).
6. Diller, K. *et al.* Investigating the molecule-substrate interaction of prototypic tetrapyrrole compounds: Adsorption and self-metalation of porphine on Cu(111). *J. Chem. Phys.* **138,** 154710 (2013).
7. Auwärter, W. *et al.* Site-specific electronic and geometric interface structure of Co-tetraphenyl-porphyrin layers on Ag(111). *Phys. Rev. B* **81,** (2010).
8. Christopher Peschel, Martin Brehm & Daniel Sebastiani. Polyphilic Interactions as Structural Driving Force Investigated by Molecular Dynamics Simulation (Project 7). *Polymers* **9,** 445 (2017).

9. Heinz, D., Amado, E. & Kressler, J. Polyphilicity—An Extension of the Concept of Amphiphilicity in Polymers. *Polymers* **10,** 960 (2018).

10. Ongungal, R. M., Sivadas, A. P., Kumar, N. S. S., Menon, S. & Das, S. Self-assembly and mechanochromic luminescence switching of trifluoromethyl substituted 1,3,4-oxadiazole derivatives. *J. Mater. Chem. C* **4,** 9588–9597 (2016).

11. De Oteyza, D. G. *et al.* Copper-phthalocyanine based metal–organic interfaces: The effect of fluorination, the substrate, and its symmetry. *J. Chem. Phys.* **133,** 214703 (2010).

Supporting Information:

Substitution of Mutually Interacting Substituents for Monolayer Engineering of Tetraphenylporphyrin Surface Self-assembled Structures

Contents

1. Methods section

All sample preparations and investigation were performed under ultrahigh vacuum (UHV) conditions with a base pressure of ~10^{-10} mbar. The crystals (MaTecK GmbH) were cleaned by cycles of sputtering with Ar+ ions at 1 keV and subsequent annealing at ~450°C. Deposition of molecules on the substrates was done by thermal evaporation from a commercial evaporator (Kentax GbmH) at ~240°C. Metal adatoms were supplied by e-beam evaporator (Oxford Applied Research). The sublimed amount of the compound was controlled by a quartz crystal microbalance. All STM images were recorded at 5 K in constant current mode (Omicron Nanotechnology GmbH) and processed with WSxM software. The STM tip was made of 90% Pt and 10% Ir wire, mechanically cut and sputtered in situ with Ar+ ions. The XPS measurements were performed at the Laboratory for Micro- and Nano-technology at the Paul Scherrer Institute (PSI). The spectra were recorded in normal emission using a monochromatic Al kα X-ray source which results in a full width at half maximum (FWHM) of 1 eV. Spectra analysis was done with Unifit software.

2. Synthesis

Tetrakis(3,4,5-trimethoxyphenyl)porphyrin[1] and tetrakis(3,5-bis(trifluoro-methyl)phenyl)porphyrin[2] were prepared and purified according to literature procedures. 5,15-Bis(3,5-trifluoromethylphenyl)-10,20-bis(3,4,5-trimethoxyphenyl)porphyrin was prepared from 5-(3,4,5-trimethoxyphenyl)dipyrrylmethane[3] by condensation with 3,5-trifluoromethylbenzaldehyde under Lindsey conditions[4] and purified by column chromatography. 5-(3,4,5-Trimethoxyphenyl)-

10,15,20-tris(3,5-trifluoromethylphenyl) porphyrin was isolated as a byproduct caused by scrambling.[4]

5,15-Bis(3,5-trifluoromethylphenyl)-10,20-bis(3,4,5-trimethoxyphenyl)porphyrin. 5-(3,4,5-Trimethoxyphenyl)dipyrrylmethane (2.04 g, 6.5 mmol) and 3,5-bistrifluoromethylbenzaldehyde (1.58 g, 6.5 mmol) were dissolved in dichloromethane (1600 mL) with stirring under an atmosphere of dry nitrogen with shielding from ambient light. Trifluoroacetic acid (200 μL) was then added whereupon the mixture turned black. Stirring was continued in the dark for 2 h then 2,3-Dichloro-5,6-dicyano-1,4-benzoquinone (4g) was added and stirring continued for a further 2 h. Dichloromethane was then evaporated under reduced pressure and the residue suspended in a small volume of dichloromethane (50 mL) followed by filtration through a pad of silica. Dichloromethane was again evaporated under reduced pressure and the residue purified using column chromatography (SiO_2/CH_2Cl_2:hexane, gradient elution: 1:2 → 1:1). The main product was obtained as a purple solid. Yield: 0.64 g (18 %). ^{1}H NMR (300 MHz, $CDCl_3$, 298 K) δ = 9.05 (d, 4H, J = 4.8 Hz, porph-β), 8.71 (d, 4H, J = 4.8 Hz, porph-β), 8.69 (s, 4H, trifluoromethylphenyl *ortho*-H), 8.36 (s, 2H, trifluoromethylphenyl *para*-H), 7.47 (s, 4H, 3,4,5-trimethoxyphenyl *ortho*-H), 4.18 (s, 6H, 4-methoxy-H), 3.99 (s, 12H, 3,5-methoxy-H) ppm; ^{13}C NMR (300 MHz, $CDCl_3$, 298 K) δ = 151.59, 144.17, 138.33, 136.92, 133.69, 132.39, 130.84, 130.48 (q, J = 33.3 Hz), 128.97, 128.82, 125.36, 121.98, 121.75, 121.22, 118.13, 116.52, 113.09, 68.19, 61.31, 60.36, 56.46 ppm; MALDI-TOF-MS (dithranol): calc'd for $C_{54}H_{39}F_{12}N_4O_6$ ([M + H]$^+$) 1067.27 a.m.u., found 1067.45.

5-(3,4,5-trimethoxyphenyl)-10,15,20-tris(3,5-trifluoromethylphenyl)porphyrin was isolated as a byproduct caused by scrambling.[4] Yield: 0.126 g (1.7 %). ^{1}H NMR (300 MHz, $CDCl_3$, 298 K) δ = 9.07 (d, 2H, J = 5.1 Hz, porph-β), 8.78 (s, 4H, porph-β), 8.73 (d, 2H, J = 5.1 Hz, porph-β), 8.69 (s, 6H, trifluoromethylphenyl *ortho*-H), 8.37 (s, 3H, trifluoromethylphenyl *para*-H), 7.47 (s, 2H, 3,4,5-trimethoxyphenyl *ortho*-H), 4.19 (s, 3H, 4-methoxy-H), 3.99 (s, 6H, 3,5-methoxy-H) ppm; ^{13}C NMR (300 MHz, $CDCl_3$, 298 K) δ = 151.66, 143.90, 143.85, 138.48, 136.69, 133.70, 132.79, 130.65 (q, J = 33.0 Hz), 130.63 (q, J = 33.0 Hz), 125.33, 122.23, 122.15, 121.72, 117.11, 116.78, 113.18, 61.34, 56.50 ppm; MALDI-TOF-MS (dithranol): calc'd for $C_{53}H_{31}F_{18}N_4O_3$ ([M + H]$^+$) 1113.21 a.m.u., found 1113.05.

3. Additional STM images

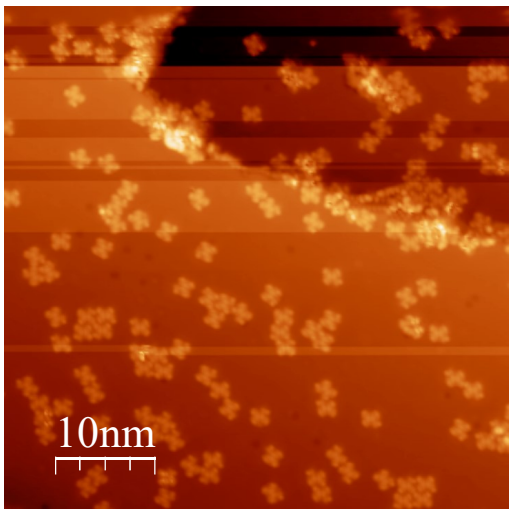

Figure S1: STM micrograph showing the distribution of Mono compounds after deposition on Cu(111). As can be seen, despite individual adsorption the molecules intend to interact with each other.

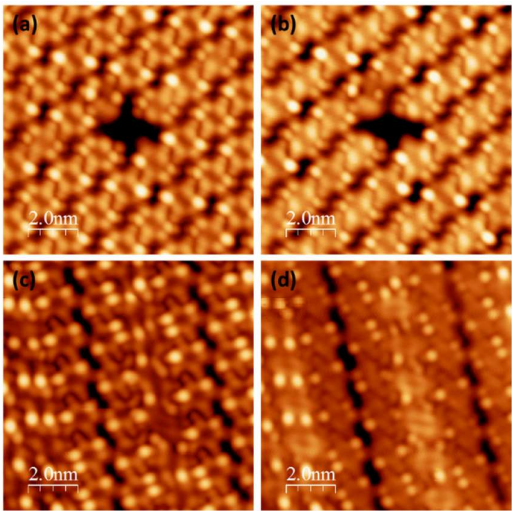

Figure S2: STM micrographs taken with opposite biases on Trans and Mono compounds after deposition on Ag(111). The images recorded with positive and negative tip biases represent occupied and unoccupied states respectively. a & b) Trans on Ag(111), bias voltages 250 mV and -250mV respectively. c & d) Mono on Ag(111), bias voltages 500mV and -500mV respectively. STM information: a, b, c, d) 10x10nm, 20pA.

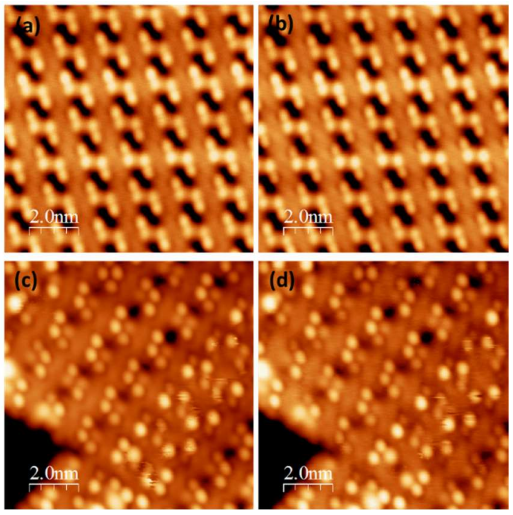

Figure S3: STM micrographs taken with opposite biases on Trans and Mono compounds after deposition on Au(111). The images recorded with positive and negative tip biases represent occupied and unoccupied states respectively. a & b) Trans on Au(111), bias voltages 500 mV and -500mV respectively. c & d) Mono on Au(111), bias voltages 500mV and -500mV respectively. STM information: a, b, c, d) 10x10nm, 30pA.

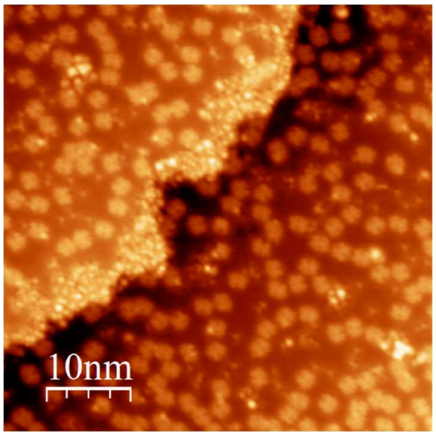

Figure S4: STM micrograph showing the distribution of MeO compounds after deposition on Cu(111). The tiny spots beside the molecules are most probably decomposition compounds that appear after deposition on the substrate.

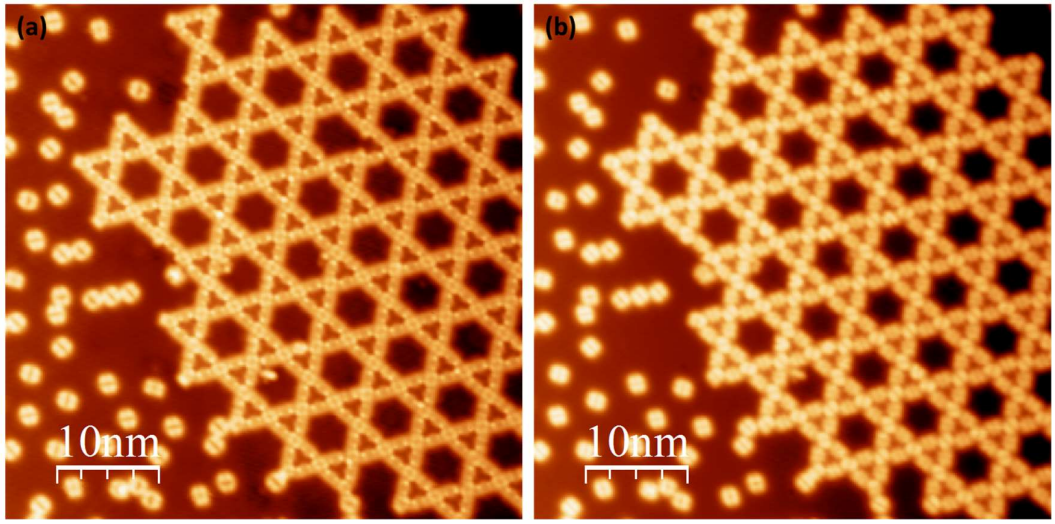

Figure S5: STM micrographs taken with opposite biases on MeO compounds after deposition on Ag(111). a) MeO/Ag(111), bias voltage 1.5V. b) MeO/Ag(111), bias voltage -1.5V. The images recorded with positive and negative tip biases represent occupied and unoccupied states respectively. STM information: a & b) 50nm x 50nm, 10pA

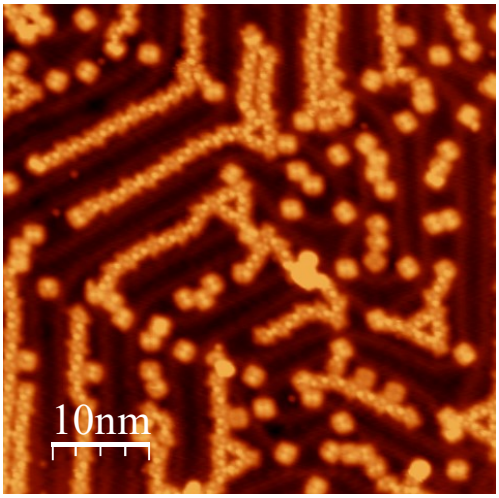

Figure S6: Overview STM image showing the formation of MeO chains on Au(111) after deposition. STM information: 10pA, 1V, 50nm

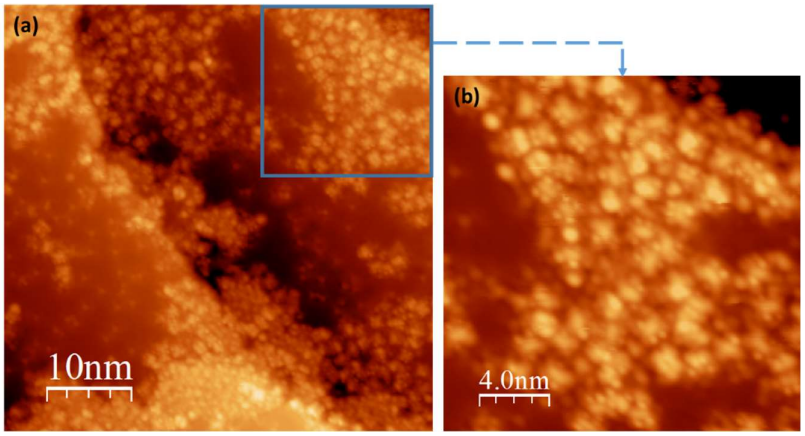

Figure S7: STM images showing the decomposition of CF3 compounds upon deposition on Cu(111). a) Overview STM image. b) Zoomed-in image. STM information: a) 50nm x 50nm, 10pA, 800mV. b) 10pA, 800mV, 20nm x 20nm.

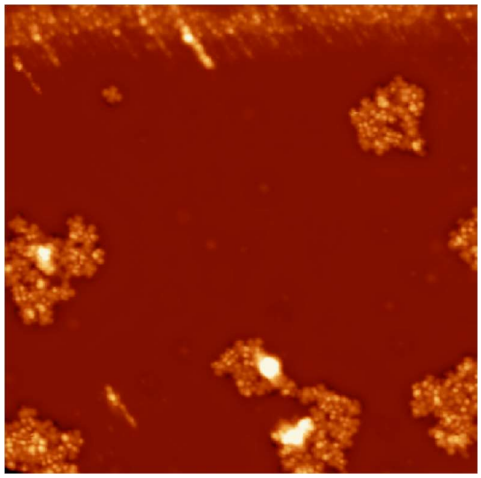

Figure S8: STM images showing the decomposition of CF3 compounds upon deposition on Ag(111). STM information: 30pA, 500mV, 50nm

4. XPS studies

4.1- Mono/Cu(111)

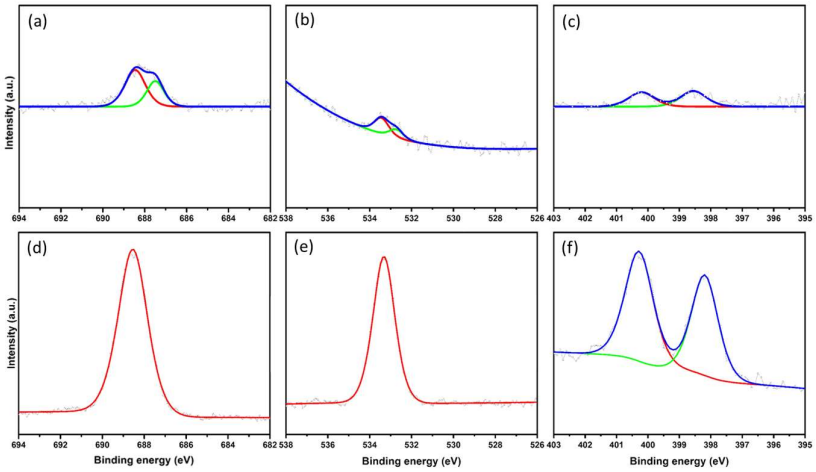

Figure S9: XP spectrum of F1s, O1s and N1s of a monolayer of Mono deposited on Cu(111) and comparison with multilayer sample. a) F1s XP spectrum for monolayer sample, the spectrum contains two peaks at 688.5eV and 687.5eV. b) O1s XP spectrum for monolayer sample, the spectrum contains two peaks at 533.3eV and 532.7eV. c) N1s XP spectrum for monolayer sample, the spectrum contains two peaks at 400.2eV and 398.5eV. d) F1s XP spectrum for multilayer sample, the spectrum contains one peak at 688.5eV. e) O1s XP spectrum for multilayer sample, the spectrum contains two peaks at 533.3eV. f) N1s XP spectrum for multilayer sample, the spectrum contains two peaks at 400.2eV and 398.2eV

As can be seen above, addition of one peak in monolayer sample comparing to multilayer case, shows the existence of an intermolecular or molecules-substrate interaction.

4.2- Trans/Ag(111)

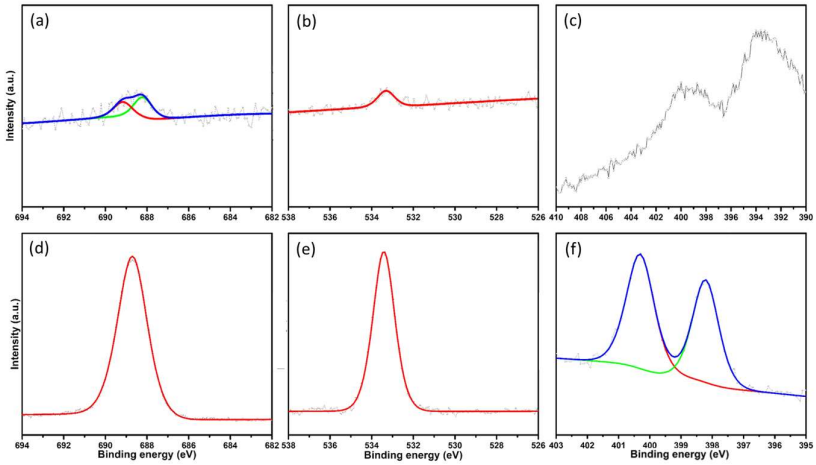

Figure S10: XP spectrum of F1s, O1s and N1s of a monolayer of Trans deposited on Ag(111) and comparison with multilayer sample. a) F1s XP spectrum for monolayer sample, the spectrum contains two peaks at 689.2eV and 688.2eV. b) O1s XP spectrum for monolayer sample, the spectrum contains one peak at 533.3eV. c) N1s XP spectrum for monolayer sample, unfortunately our XPS resolution has not been enough to detect N1s peaks. d) F1s XP spectrum for multilayer sample, the spectrum contains one peak at 688.7eV. e) O1s XP spectrum for multilayer sample, the spectrum contains two peaks at 533.3eV. f) N1s XP spectrum for multilayer sample, the spectrum contains two peaks at 400.2eV and 398.2eV

4.3- Mono/Ag(111)

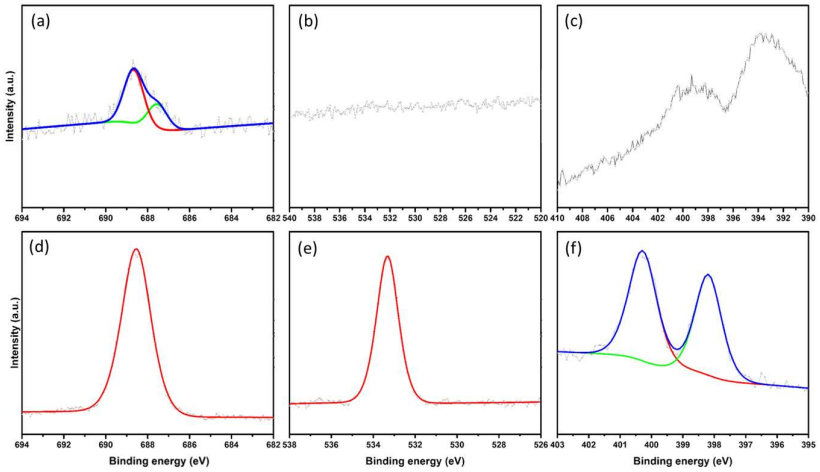

Figure S11: XP spectrum of F1s, O1s and N1s of a monolayer of Trans deposited on Ag(111) and comparison with multilayer case. a) F1s XP spectrum for monolayer sample, the spectrum contains 2 peaks at 688.5eV and 687.5eV. b) O1s XP spectrum for monolayer sample, the O1s XP spectrum could not be detected, or it might be that Oxygen groups are eliminated upon deposition. c) N1s XP spectrum for monolayer sample, unfortunately our XPS resolution has not been enough to detect N1s peaks. d) F1s XP spectrum for multilayer sample, the spectrum contains one peak at 688.5eV. e) O1s XP spectrum for multilayer sample, the spectrum contains two peaks at 533.3eV. f) N1s XP spectrum for multilayer sample, the spectrum contains two peaks at 400.2eV and 398.2eV.

4.4- Trans/Au(111)

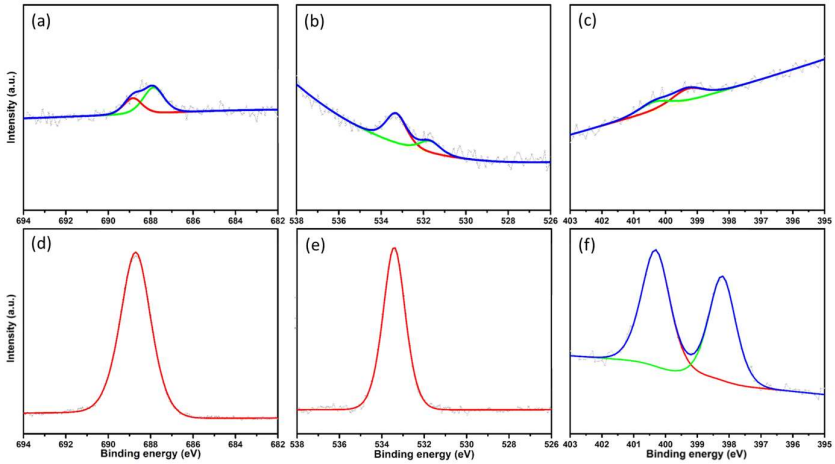

Figure S12: XP spectrum of F1s, O1s and N1s of a monolayer of Trans deposited on Au(111) and comparison with multilayer sample. a) F1s XP spectrum for monolayer sample, the spectrum contains two peaks at 688.8eV and 687.8eV. b) O1s XP spectrum for monolayer sample, the spectrum contains two peaks at 533.3eV and 531.7eV. c) N1s XP spectrum for monolayer sample, the spectrum contains two peaks at 400.3eV and 399.3eV. d) F1s XP spectrum for multilayer sample, the spectrum contains one peak at 688.7eV. e) O1s XP spectrum for multilayer sample, the spectrum contains two peaks at 533.3eV. f) N1s XP spectrum for multilayer sample, the spectrum contains two peaks at 400.2eV and 398.2eV.

4.5- Mono/Au(111)

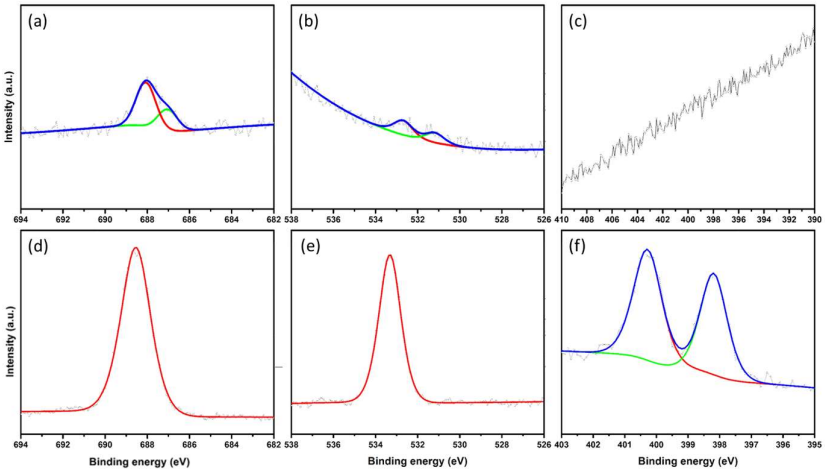

Figure S13: XP spectrum of F1s, O1s and N1s of a monolayer of Mono deposited on Au(111) and comparison with multilayer sample. a) F1s XP spectrum for monolayer sample, the spectrum contains two peaks at 688.1eV and 687.1eV. b) O1s XP spectrum for monolayer sample, the spectrum contains two peaks at 532.7eV and 531.2eV. c) N1s XP spectrum for monolayer sample, unfortunately our XPS resolution has not been enough to detect N1s peaks. d) F1s XP spectrum for multilayer sample, the spectrum contains one peak at 688.5eV. e) O1s XP spectrum for multilayer sample, the spectrum contains two peaks at 533.3eV. f) N1s XP spectrum for multilayer sample, the

spectrum contains two peaks at 400.2eV and 398.2eV.

4.6- MeO/Cu(111)

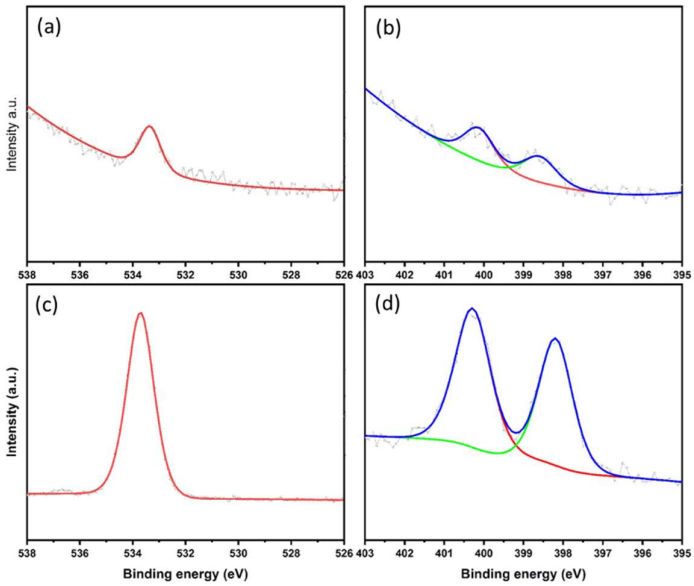

Figure S14: XP spectra of O1s and N1s of a monolayer of MeO deposited on Cu(111) and comparison with multilayer sample. a) O1s XP spectrum for monolayer sample, the spectrum contains one peaks at 533.3eV. b) N1s XP spectrum for monolayer sample, the spectrum contains two peaks at 400.1eV and 398.6eV. c) O1s XP spectrum for multilayer sample, the spectrum contains one peak at 533.3eV. d) N1s XP spectrum for multilayer sample, the spectrum contains two peaks at 400.2eV and 398.2eV.

4.7- MeO/Ag(111)

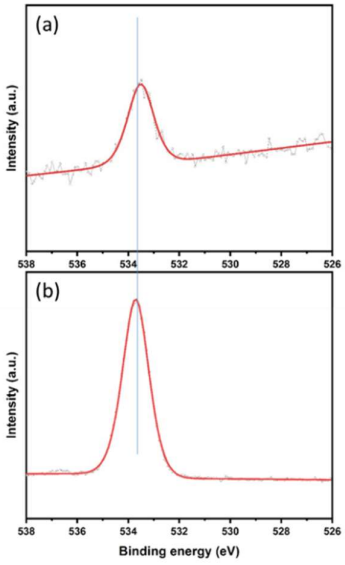

Figure S15: O1s XP spectrum of a monolayer of MeO deposited on Ag(111) and comparison with multilayer sample. a) Monolayer, peak position: 533.5eV. b) Multilayer, peak position: 533.7eV. As can be seen, there is no big difference between the peak positions which indicates that the

chemical environment of oxygens are not changed. This is an evidence that star shape nanostructures are hydrogen bonded.

4.8- MeO/Au(111)

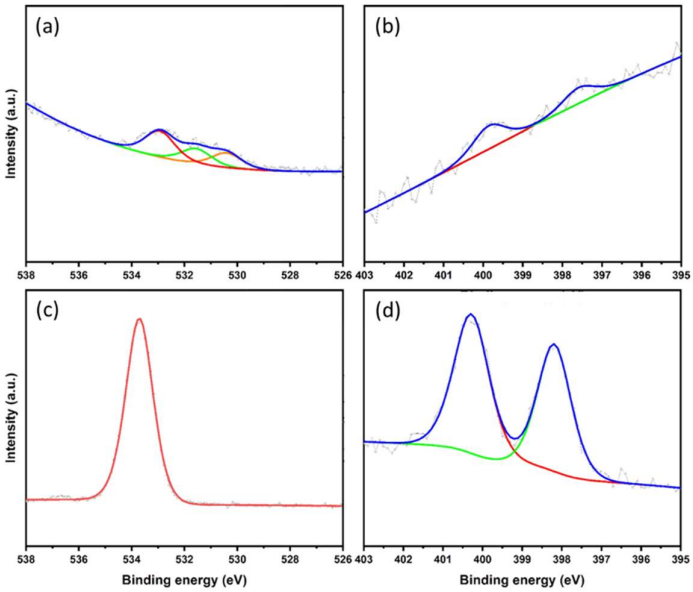

Figure S16: O1s and N1s XP spectra of a monolayer of MeO deposited on Au(111) and comparison with multilayer sample. a) Monolayer O1s spectrum, peak positions: 530.4 eV, 531.55eV, 532.93eV. b) Monolayer N1s spectrum, peak positions: 399.9eV and 397.6eV. c) Multilayer O1s spectrum, peak position: 533.7eV. The XP spectrum for monolayer sample suggests different oxygen groups. This might be due to a chemical interaction or the fact that each of the oxygens in methoxy group are having different binding energy. d) Multilayer N1s XP spectrum contains two peaks at 400.2eV and 398.2eV.

5. DFT studies

The preliminary DFT results for the mentioned self-assemblies is presented here. Please note that these models are not fully correct since small corrections noticing the possible on-surface chemical reactions must be considered.

5.1 TRANS/Cu(111)

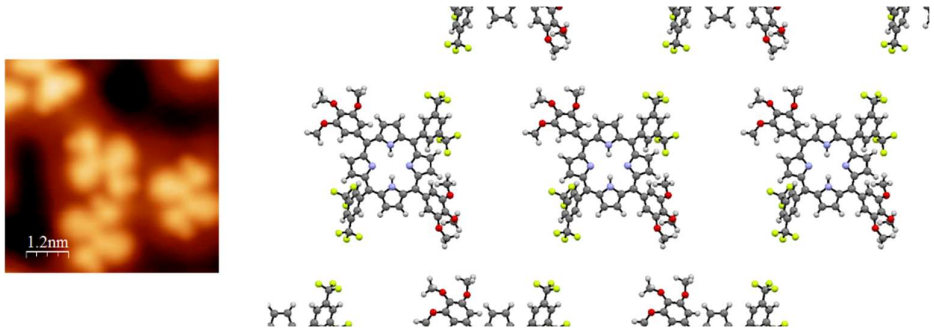

Figure S17: DFT model showing the distribution of Trans compounds on Cu(111).

5.2 TRANS/Ag(111)

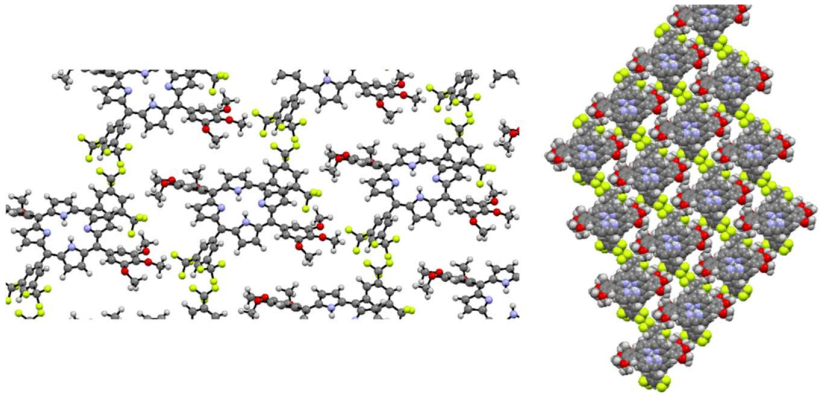

Figure S18: DFT model describing the formation of self-assembly of TRANS/Ag(111).

5.3 TRANS/Au(111)

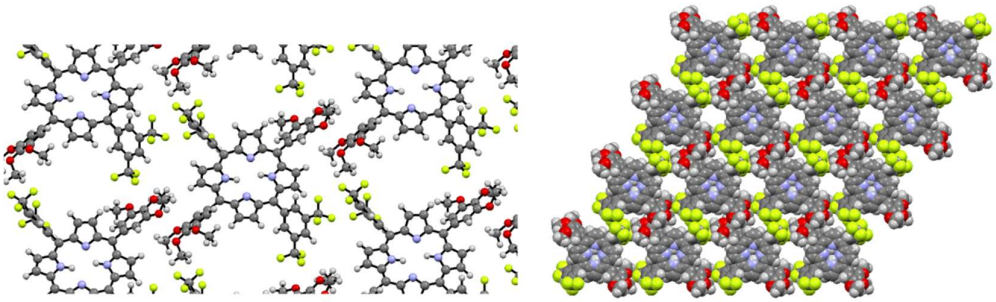

Figure S19: DFT model describing the formation of self-assembly of TRANS/Au(111).

5.4 MONO/Cu(111)

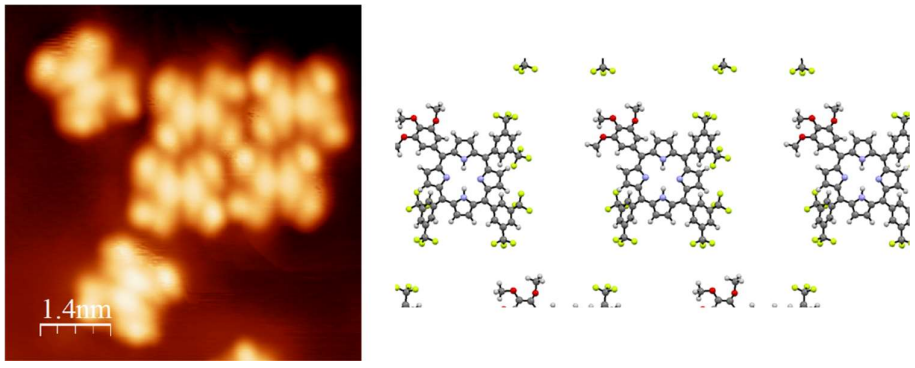

Figure S20: DFT model showing the distribution of Mono compounds on Cu(111).

5.5 MONO/Ag(111)

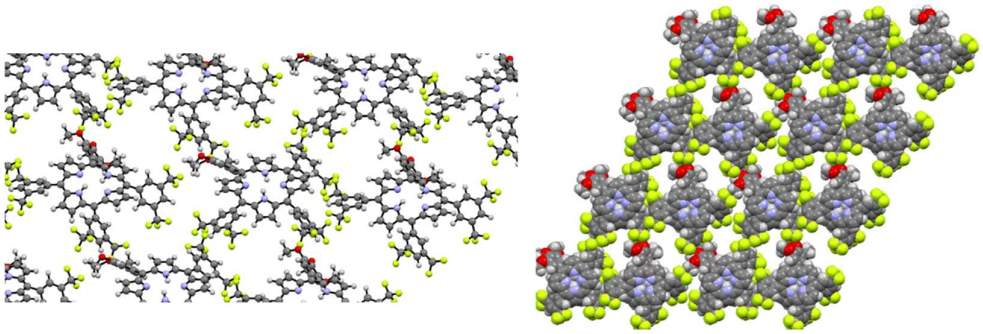

Figure S21: DFT model describing the formation of self-assembly of Mono/Ag(111).

5.6 MONO/Au(111)

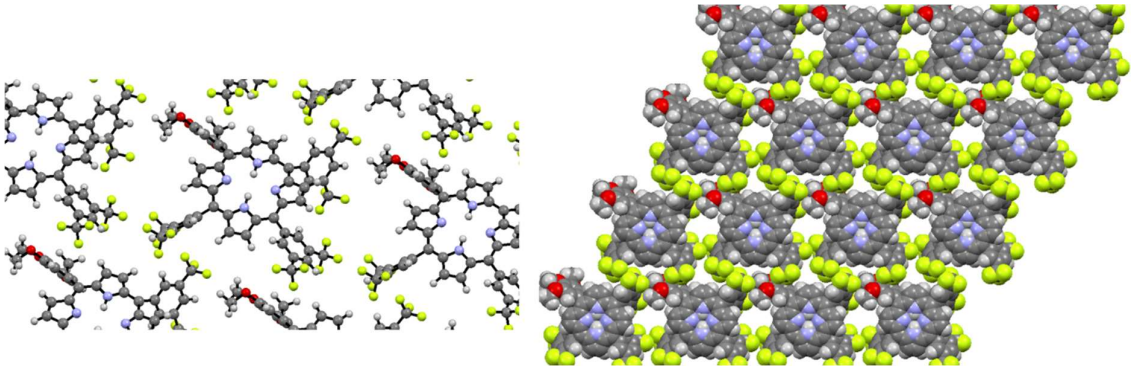

Figure S22: DFT model describing the formation of self-assembly of Mono/Au(111).

Summary and outlook

This thesis addresses the following questions: i) How can direct comparison between in-solution and on-surface studies help us understand the properties of the material and facilitate the discovery of new applications? ii) How can on-surface molecular architectures be controlled with atomic precision by utilizing different chemical compounds and substrates? iii) How does the surface affect the supramolecular chemistry and the formation of novel, molecular architectures? iv) How can functionalization be used to expand the variety of on-surface reactions and consequently manufacture different on-surface self-assemblies?

To tackle these questions, in chapter [[1]], the step-by-step oxidation and subsequent modification of pyrazinacene self-assemblies was studied. Dihydrooctaazatetracene (2) and dihydrodecaazapentacene (1) which are core, chromophoric structures, lacking N-substituents, were studied both in-solution and on-surface of Cu(111) single crystal. They show a chiral behavior upon their in-situ deposition. (1) and (2) can be oxidized to octaazatetracene (2-ox) and decaazapentacene (1-ox) after annealing to 150°C and form linear arrays. These linear arrays break upon further annealing to 300°C and a new morphology in which the compounds are planar, flat and cyclodehydrogenated appear. These oxidation compounds are potentially n-type molecules whose structures ought to be compatible with the much studied p-type pentacene material, therefore they can be used to facilitate preparation of organic thin film transistors.

In chapter [[2]], we have shown how a non-planar, hydrogen-bonding motif occurs in planar, polyaromatic DPDI self-assemblies on the weakly interacting Bi/Cu(100) substrate. Two coexisting self-assembled structures of hexagonal networks and compact zigzags appear upon thermal-deposition of DPDI on the mentioned bi-layer substrate. Remarkably, Hydrogen bonding is only possible by out-of-plane rotation of the molecules. Considering the fact that direct deposition of DPDI on Cu(100) substrate does not lead to any sort of assembly, this study shows the importance of the substrate in guiding the formation of self-assembled, nano-structures.

In chapter [[3]], the effect of Trifluoromethyl and Methoxy groups on the self-assembly structures of symmetrically and unsymmetrically-substituted tetraphenylporphyrins is studied. We aimed to control the resulting self-assembled structures according to the substrate identity (Cu/Ag/Au) and intermolecular interactions. In addition, comparison of the on-surface behavior of these compounds with functionalized tetraphenylporphyrins, tetrakis(3,4,5-trimethoxyphenyl)porphyrin and tetrakis(3,5-trifluoromethylphenyl)porphyrin is presented. This study is a unique example of on-surface self-assemblies involving fluorophilic interactions.

Bibliography

1. Gao, H.-Y. *et al.* In-plane Van der Waals interactions of molecular self-assembly monolayer. *Appl. Phys. Lett.* **106,** 081606 (2015).
2. Kunkel, D. A. *et al.* Self-assembly of strongly dipolar molecules on metal surfaces. *J. Chem. Phys.* **142,** 101921 (2015).
3. Barth, J. V. *et al.* Building Supramolecular Nanostructures at Surfaces by Hydrogen Bonding. *Angew. Chem. Int. Ed.* **39,** 1230–1234 (2000).
4. Kossev, I. *et al.* Highly Ordered 2D Hydrogen-Bonded Structures of a Tetralactam Macrocycle on the Au(111) Surface. *Adv. Funct. Mater.* **17,** 513–519 (2007).
5. Berg, J. M., Tymoczko, J. L., Stryer, L. & Stryer, L. *Biochemistry*. (W.H. Freeman, 2002).
6. Lee, D., Redfern, O. & Orengo, C. Predicting protein function from sequence and structure. *Nat. Rev. Mol. Cell Biol.* **8,** 995–1005 (2007).
7. Matena, M. *et al.* Aggregation and Contingent Metal/Surface Reactivity of 1,3,8,10-Tetraazaperopyrene (TAPP) on Cu(111). *Chem. - Eur. J.* **16,** 2079–2091 (2010).
8. Zhang, J. *et al.* Probing the spatial and momentum distribution of confined surface states in a metal coordination network. *Chem Commun* **50,** 12289–12292 (2014).
9. Peyrot, D. & Silly, F. On-Surface Synthesis of Two-Dimensional Covalent Organic Structures versus Halogen-Bonded Self-Assembly: Competing Formation of Organic Nanoarchitectures. *ACS Nano* **10,** 5490–5498 (2016).
10. Björk, J., Hanke, F. & Stafström, S. Mechanisms of Halogen-Based Covalent Self-Assembly on Metal Surfaces. *J. Am. Chem. Soc.* **135,** 5768–5775 (2013).
11. Anfinsen, C. B. Principles that Govern the Folding of Protein Chains. *Science* **181,** 223–230 (1973).
12. Selkoe, D. J. Folding proteins in fatal ways. *Nature* **426,** 900–904 (2003).
13. Deechongkit, S. *et al.* Context-dependent contributions of backbone hydrogen bonding to β-sheet folding energetics. *Nature* **430,** 101–105 (2004).
14. Dobson, C. M. Protein folding and misfolding. *Nature* **426,** 884–890 (2003).
15. Nijs, T. *et al.* The Different Faces of 4′-Pyrimidinyl-Functionalized 4,2′:6′,4″-Terpyridines: Metal–Organic Assemblies from Solution and on Au(111) and Cu(111) Surface Platforms. *J. Am. Chem. Soc.* **140,** 2933–2939 (2018).

16. Yan, H.-J., Liu, J., Wang, D. & Wan, L.-J. Two-dimensional self-assemblies of telechelic organic compounds: structure and surface host-guest chemistry. *Philos. Trans. R. Soc. Math. Phys. Eng. Sci.* **371,** 20120302–20120302 (2013).
17. Yasuda, T., Goto, T., Fujita, K. & Tsutsui, T. Ambipolar pentacene field-effect transistors with calcium source-drain electrodes. *Appl. Phys. Lett.* **85,** 2098–2100 (2004).
18. Allen, C. F. H. & Gates, J. W. A New Synthesis of the Pentacene Ring System. *J. Am. Chem. Soc.* **65,** 1502–1503 (1943).
19. *Surface Analysis with STM and AFM*. (Wiley-VCH Verlag GmbH, 1995).
20. Shchyrba, A. *et al.* Controlling the Dimensionality of On-Surface Coordination Polymers via Endo- or Exoligation. *J. Am. Chem. Soc.* **136,** 9355–9363 (2014).
21. Ogunrinde, A., Hipps, K. W. & Scudiero, L. A Scanning Tunneling Microscopy Study of Self-Assembled Nickel(II) Octaethylporphyrin Deposited from Solutions on HOPG. *Langmuir* **22,** 5697–5701 (2006).
22. Joshi, S. *et al.* Control of Molecular Organization and Energy Level Alignment by an Electronically Nanopatterned Boron Nitride Template. *ACS Nano* **8,** 430–442 (2014).
23. Morchutt, C., Björk, J., Krotzky, S., Gutzler, R. & Kern, K. Covalent coupling via dehalogenation on Ni(111) supported boron nitride and graphene. *Chem. Commun.* **51,** 2440–2443 (2015).
24. Wäckerlin, C. *et al.* Assembly of 2D ionic layers by reaction of alkali halides with the organic electrophile 7,7,8,8-tetracyano-p-quinodimethane (TCNQ). *Chem. Commun.* **47,** 9146 (2011).
25. Carrera, A. *et al.* Controlling Carboxyl Deprotonation on Cu(001) by Surface Sn Alloying. *J. Phys. Chem. C* **117,** 17058–17065 (2013).
26. Wäckerlin, A. *et al.* Molecular Chessboard Assemblies Sorted by Site-Specific Interactions of Out-of-Plane d-Orbitals with a Semimetal Template. *Nano Lett.* **17,** 1956–1962 (2017).
27. Matena, M. *et al.* On-surface synthesis of a two-dimensional porous coordination network: Unraveling adsorbate interactions. *Phys. Rev. B* **90,** (2014).
28. Packwood, D. M. & Hitosugi, T. Materials informatics for self-assembly of functionalized organic precursors on metal surfaces. *Nat. Commun.* **9,** (2018).
29. Diaconescu, B. *et al.* Molecular Self-Assembly of Functionalized Fullerenes on a Metal Surface. *Phys. Rev. Lett.* **102,** (2009).
30. Snegir, S. V. *et al.* STM Observation of Open- and Closed-Ring Forms of Functionalized

Diarylethene Molecules Self-Assembled on a Au(111) Surface. *J. Phys. Chem. Lett.* **2,** 2433–2436 (2011).

31. Grill, L. Functionalized molecules studied by STM: motion, switching and reactivity. *J. Phys. Condens. Matter* **20,** 053001 (2008).
32. Wormald, R., Evans, J. R., Smeeth, L. L. & Henshaw, K. S. Photodynamic therapy for neovascular age-related macular degeneration. *Cochrane Database Syst. Rev.* (2007). doi:10.1002/14651858.CD002030.pub3
33. Walker, C. ., Sibly, R. ., Hopkin, S. . & Peakall, D. . *Principles of Ecotoxicology, Fourth Edition*. (CRC Press, 2012).
34. Lewtak, J. P. & Gryko, D. T. Synthesis of π-extended porphyrins via intramolecular oxidative coupling. *Chem. Commun.* **48,** 10069 (2012).
35. Girovsky, J. *et al.* Antiferromagnetic coupling of Cr-porphyrin to a bare Co substrate. *Phys. Rev. B* **90,** (2014).
36. Nowakowski, J. *et al.* Porphyrin metalation providing an example of a redox reaction facilitated by a surface reconstruction. *Chem. Commun.* **49,** 2347 (2013).
37. Nowakowski, J. *et al.* Probing the Reactivity of Functionalized Surfaces by Porphyrin Metalation. *ChemistrySelect* **1,** 891–895 (2016).
38. Iacovita, C. *et al.* Controlling the Dimensionality and Structure of Supramolecular Porphyrin Assemblies by their Functional Substituents: Dimers, Chains, and Close-Packed 2D Assemblies. *Chem. - Eur. J.* **18,** 14610–14613 (2012).

Acknowledgements

Here I would like to sincerely thank all the people who kindly helped me during my PhD. I am very lucky to meet and work with wonderful people who were always supportive no matter what.

Especially I would like to acknowledge my PhD supervisor Thomas Jung for the opportunity of working in his group and his support and kindness during these 4 years. I am very thankful for his supervision, all the freedom I had to act creative, our fruitful scientific discussions and his great support in writing the manuscripts. In addition, I will never forget our wonderful group excursions in planning which Thomas is indeed an expert.

I like to specially thank all my former and current colleagues in Nanolab and PSI, Aneliia and Christian Wäckerlin, Sylwia Nowakowska, Milos Baljozovic, Jan Nowakowski, Jan Girovsky, Harald Rossmann, Olha Popova, Dipanwitta Dutta, Mina Moradi and Mehdi Heydari. My special thanks goes to my special colleagues Aisha Ahsan and Thomas Nijs. I am very grateful to them not only because of all the technical and scientific support but also because of the great friendship we have which helped us surviving difficult days.

I am very grateful for all the technical support that I received from very nice technicians with whom I worked. Specifically Marco Martina for his always on time support and magic presence! I never understood how stainless steel listens him and as soon as he appears in the lab everything magically start working! I am also sincerely thankful to Rolf Schelldorfer not only because of his similar magical properties but also because of his kindness, patience and indescribable love he has for his job which spreads positive energy all over the lab. I am very thankful to Yves Pellmont who has never been officially our technician but as a friend despite his own tough job and time schedule has always been ready to help me and my colleagues. Many thanks to Matthes Senn for his technical support during the short time that he was our technician and to all other technicians in mechanical and electronic workshop who are always ready to help and do a perfect job.

I would like to express my special gratefulness to all the great chemistry groups I worked with for the synthesis of the compounds presented in this thesis: Lutz Gade from University of Heidelberg, David Miklík and Jonathan Hill from National Institute for Material Science / Japan (NIMS). Specifically, I am very grateful to Jonathan, we have never met in person but I have learned a lot from him. This great collaboration with NIMS was incredibly joyful and productive for me, I did realize how science does not limit to geographical borders and scientists despite long distances can fruitfully work with each other.

Acknowledgements

I am very thankful to the great intelligent computational scientists who helped me with all the DFT calculations presented in this thesis: Luiza Buimaga-Iarinca from National Institute for Research and Development of Isotopic and Molecular Technologies, Cluj-Napoca in Romania and Jonas Björk from Ulm University.

I would like to sincerely thank many people here in department of physics of university of Basel, Germaine C. Weaver, Claudia Wirth, Astrid Kalt and Barbara Kammermann from secretarial section. Special thanks to Dominik Sifrig not only because of always having liquid helium on time but also because of our everyday early mornings 'hello, good mornings' in helium recovery center corridor! It is great to start the day seeing kind people. Many thanks to Bernd Heimann, our kind Hauswart, who is always ready to help.

Last but not least, I am very thankful to all the block course, summer students and scientist visitors we had in our lab: Tino Matter, Mac Iwasaki, Mariah O'Doherty, Robert Skonieczny, Martin Dudoit, Simon Bompard and Laurent Clarissou, naming few, for sharing their experiences and scientific supports.

I would like to specifically thank my lovely family who has always been the greatest support for me. My beloved parents, whose love and guidance are with me in whatever I pursue and my lovely brother and sister. I have no words to acknowledge them, no words to express my gratefulness and no words to express my unlimited love.

And finally, I would like to thank my beloved husband, Meghdad, who is the most supportive, kindest and best husband in the world who wrote his own PhD thesis in SBB trains, traveled at least 4 hours a day such that I could walk 10 minutes to university. I am the luckiest on the planet to have him beside myself passing the journey of life together and have no words to express my infinite love.

I am sincerely thankful to all the people who helped me finishing this challenging chapter of my life and hope that I have not forgotten a name here.